

Dissertation
submitted to the
Combined Faculties for the Natural Sciences and for Mathematics
of the Ruperto-Carola University of Heidelberg, Germany
for the degree of
Doctor of Natural Sciences

presented by
Dipl. Phys. RENÉ WINTER
born in Steinfurt

Day of oral examination: 25th of May 2011

Fluorescent Tracers for air-sided Concentration Profile Measurements at the Air-Water Interface

Referees:

Prof. Dr. BERND JÄHNE

Prof. Dr. WERNER AESCHBACH-HERTIG

Abstract: This study focuses on the first visualization of the air-sided mass boundary layer at the wind-driven air-water interface using a planar laser induced fluorescence technique (PLIF). The PLIF technique gives vertical concentration profiles with high temporal resolution. This allows to investigate the transport for tracers that are partially or fully controlled by the air-sided boundary layer, i.e. to study the influence of substance solubility on gas exchange. The PLIF setup was constructed utilizing a 266 nm pulsed laser operating at 20 Hz with a pulse duration of 6 ns for the fluorescence excitation and UV-optics for acquisition of profile images. A wind-wave tank was built that is optimized for visualization measurements. Based on literature review, a set of tracers with differing solubilities ($3 < \alpha < 22000$) were selected. The PLIF signal of this set was measured and compared in terms of signal strength. For a fixed wind-wave condition the transfer velocity and its solubility dependence is evaluated. Acetone, fluorobenzene, anisole, 4-fluoroanisole, 2,4-difluoroanisole, 2-fluorophenol and 2-methoxyphenol provide sufficient signal strength to acquire vertical air-sided concentration profiles averaged over 2.5 s with a resolution of 227 μm . 1,4-Difluorobenzene provides a signal strong enough for single pulse measurements. The signal provided by ethanal and 4-methylanisole was too low for the current setup. The air-sided transfer velocities and the effect of the solubility on gas exchange could not be assessed from the concentration profiles due to multiple reflections (within the first 10 mm) and too high fluorescence dynamics in the water at the interface.

Zusammenfassung: Diese Arbeit behandelt die Visualisierung der luftseitigen Stofftransportgrenzschicht zur Untersuchung des Gasaustauschs an einer windbewegten Wasseroberfläche. Hierzu wurde erstmalig eine planare, laserinduzierte Fluoreszenztechnik (PLIF) eingesetzt, womit zeitlich hochaufgelöste vertikale Konzentrationsprofile gewonnen werden können. Dies erlaubt die Untersuchung des Stofftransports von Substanzen die teilweise oder vollständig luftseitig kontrolliert sind, z.B. hinsichtlich des Einflusses der Löslichkeit. Der PLIF Aufbau basiert auf einem gepulsten UV-Laser mit 266 nm Wellenlänge und 20 Pulsen pro Sekunde mit einer Pulsdauer von 6 ns zur Fluoreszenzanregung. Die Aufnahme der Konzentrationsprofile erfolgt mittels einer bildgebenden UV-Optik. Für die Visualisierungsmesstechnik wurde zudem ein optimierter Wind-Wellen-Kanal aufgebaut. Basierend auf einer Literaturrecherche wurde ein Satz von Tracern mit verschiedenen Löslichkeiten ($3 < \alpha < 22000$) ausgewählt. Das PLIF-Signal wurde gemessen und die Tracer hinsichtlich ihrer Signalstärke verglichen. Für eine bestimmte Wind-Wellen-Bedingung wurden die Transfergeschwindigkeit berechnet und der Einfluss der Löslichkeit auf den Gasaustausch ausgewertet. Die Signalstärke von Aceton, Fluorobenzol, Anisol, 4-Fluoranisol, 2,4-Difluoranisol, 2-Fluorphenol und 2-Methoxyphenol erlaubt Aufnahmen von Profilen mit einer Auflösung von 227 μm , gemittelt über 2,5 Sekunden. 1,4-Difluorobenzol verfügt über ein Signal stark genug für Einzelpulsmessungen. Das Fluoreszenzsignal von Ethanal und 4-Methylanisol war nicht ausreichend. Die luftseitigen Transfergeschwindigkeiten und der Einfluß der Löslichkeit auf den Transfer konnten jedoch aufgrund von Unsicherheiten durch zu hohe Fluoreszenzdynamik an der Grenzfläche und Mehrfachreflexionen innerhalb der ersten 10 mm nicht abschließend bewertet werden.

Contents

1	Introduction	1
1.1	Motivation	1
1.2	Goal	3
1.3	Overview	4
I	Background	7
2	Gas Transfer at the Air-Water Interface	9
2.1	Turbulent-Diffusive Flows	9
2.1.1	Shear Stress and Friction Velocity	12
2.2	Velocity and Concentration Profiles	13
2.2.1	Turbulent Layer	13
2.2.2	Viscous Boundary Layer	14
2.2.3	Interpolated Profile	18
2.3	Transfer Resistance and Velocity	19
2.3.1	Boundary Layer Thickness	20
2.3.2	Air-Water Transfer Partition	21
2.3.3	Concentration Profiles	23
2.3.4	Controlling Phase	25
3	Fluorescence Theory	31
3.1	Stokes Shift	31
3.2	Phosphorescence	32
3.3	Fluorescence Quantum Yield and Life-Time	33
3.4	Quenching	33
4	Absorption Spectroscopy	35
4.1	Lambert-Beer Law	35
4.1.1	Absorption Cross Section	37
4.2	UV/Vis Spectra and the Molecular Structure	37

II	Experimental Methods	41
5	Applied Planar Laser Induced Fluorescence	43
5.1	Effective Fluorescence Quantum Yield	43
5.2	Concentration Measurements	44
5.3	Saturation Excitation	45
5.3.1	Calculating the Laser Irradiance	46
5.3.2	Optical Thickness	47
5.4	Signal Rating	48
5.4.1	Calculating the Signal Rating	48
5.4.2	Measuring the Signal Rating	49
5.5	Resolution	50
6	Setup	53
6.1	Preliminary Measurement Setup	53
6.1.1	Tracer Injection	54
6.1.2	Fluorescence Measurement	55
6.1.3	Spectrometer	56
6.2	Wind-Wave Tank Setup	57
6.2.1	Cover Plate	58
6.2.2	Tracer Injection	59
6.2.3	UV-Laser System	60
6.2.4	Camera Setup	66
6.2.5	Spectrometer	67
7	Experimental Procedure	71
7.1	Important Tracer Attributes	71
7.2	Test Conditions for the Tracer Study	73
7.3	Data Acquisition and Processing	75
7.3.1	Spectrometer Data	75
7.3.2	Signal Strength Evaluation	76
7.3.3	Concentration Profiles	78
7.3.4	Pitot-Tube Data	81
7.3.5	Box Model	82
III	Measurements and Results	85
8	Tracer Characterization	87
8.1	Acetone	87
8.1.5	Signal Strength	90
8.1.6	Boundary Layer Visualization	90
8.2	Ethanal	93

8.2.5	Signal Strength	95
8.2.6	Boundary Layer Visualization	96
8.3	Fluorobenzene	98
8.3.5	Signal Strength	100
8.3.6	Boundary Layer Visualization	100
8.4	1,4-Difluorobenzene	102
8.4.5	Signal Strength	104
8.4.6	Boundary Layer Visualization	105
8.5	Anisole	107
8.5.5	Signal Strength	109
8.5.6	Boundary Layer Visualization	109
8.6	4-Fluoroanisole	111
8.6.5	Signal Strength	113
8.6.6	Boundary Layer Visualization	113
8.7	4-Methylanisole	115
8.7.5	Signal Strength	117
8.7.6	Boundary Layer Visualization	117
8.8	2,4-Difluoroanisole	119
8.8.5	Signal Strength	120
8.8.6	Boundary Layer Visualization	121
8.9	2-Fluorophenol	123
8.9.5	Signal Strength	124
8.9.6	Boundary Layer Visualization	125
8.10	2-Methoxyphenol	127
8.10.5	Signal Strength	128
8.10.6	Boundary Layer Visualization	129
8.11	Other Tracers	131
8.11.1	Diacetyl	131
8.11.2	2,3-Pentanedione	131
8.11.3	Benzaldehyde	132
8.11.4	Indolizine	132
8.11.5	Sulfur dioxide	132
9	Summary of Results	133
9.1	Air-sided LIF	133
9.1.1	Resolution	134
9.1.2	Water-Sided Fluorescence	137
9.2	Transfer Measurements	138
9.3	Controlling Phase	140
10	Conclusion and Outlook	143
10.1	Conclusion	143
10.2	Outlook	144

Appendix	146
A The Linear Visualization-Test Wind-Wave Tank	147
A.1 Motivation	147
A.2 Setup	148
A.2.1 Water System	148
A.2.2 Air System	154
A.2.3 Stirred Tank	158
A.3 Characterization	159
A.3.1 Wind Profile	159
A.3.2 Experimental Method and Measurements	160
A.3.3 Wind Profile and Characteristics	160
A.4 Leakage Rate	165
A.4.1 Experimental Method	165
A.4.2 Results	166
B Datasheets	167
B.1 UV Broadband Anti-Reflective Coating ARB 2 UV	167
B.2 Sensicam EM UV Calibration Data	168
B.3 Absorption and Fluorescence Spectra	169
B.3.1 Acetone	169
B.3.2 Ethanal	169
B.3.3 Diacetyl	170
C Bibliography	171

1 Introduction

1.1 Motivation

Since the beginning of the industrial revolution, mankind has deliberately as well as undeliberately released an increasing variety of organic and inorganic chemicals into the environment. The reasons are numerous. The increasing use of fossil fuels has caused a dramatic rise in global carbon dioxide (CO_2) concentration. Incomplete combustion produces sulfur dioxide (SO_2) and carbon monoxide (CO), causing acid rain and the acidification of lakes and soil water. Accidental release of petroleum, a mixture of more than 11000 compositionally different organic compounds [33], spills it directly and uncontrolled into the environment. Organic chemicals are widely used as insecticides and biocides, often without understanding of their full impact on the local ecosystem and human health.

A famous example of a synthetic organic substance being widely used without knowledge of its detrimental effects is dichloro-diphenyl-trichloroethane or simply DDT. A highly effective insecticide, DDT was introduced during the second world war to protect troops against malaria and typhus. After the war, it was widely used: it was deployed not only as agricultural insecticide but also to remove insects from popular beaches [64]. In 1972, DDT use was banned in the US and later in Europe after negative effects upon wildlife and human health became known [51]. To this day there have been discussions whether controlled use of DDT was acceptable or even necessary to stop the propagation of aforementioned diseases carried by insects like mosquitoes [76].

In the light of this knowledge, it is reasonable that there is more than academic interest in the processes involved in the distribution and decomposition of these substances into our environment. To fully understand the transport of even a single substance one would need to understand all processes involved. It is necessary to know how transport and transformation of the substances in and across all of earth's compartments (atmosphere, biosphere, cryosphere, hydrosphere and lithosphere) function. That is no small task. This work focuses on one aspect of these processes: the transport of chemicals across the wind-driven air-water interface.

Atmosphere and hydrosphere complement each other in the distribution of chemicals, heat and small particles across the globe. While transport within the atmosphere is faster, some substances prefer an aquatic milieu. Furthermore the residence time in

water is longer than in air. This augments the importance of transport through the sea despite the lower velocities.

The global interface between air and water is huge. The ice-free ocean covers 3.28×10^8 km² of our planet [see 60, App. E]. This number accounts for neither lakes nor rivers. These would inflate the size of the global water surface slightly but are not the focus of this work.

In the environment, air and water phase are usually not in equilibrium. The size of atmosphere and ocean prevent them from quickly transporting chemicals from their bulk to an interface. Natural biogeochemical processes and human influence constantly drive them into a state of disequilibrium. Another important factor on smaller, local scales are catastrophic events that rapidly change the composition of one of the phases.

One example is the explosion of the offshore oil rig Deepwater Horizon in April 2010, which delivered approximately 780×10^5 m³[48] of unrefined petroleum into the Gulf of Mexico near the US south coast. Compared to the 2.5×10^{15} m³ of water in the Gulf of Mexico this number might seem insignificant, but on a local scale the effect was dramatic.

The ocean is the world's biggest CO₂ sink. About one third of CO₂ produced by fossil fuel burning is taken up by the ocean [17]. Precise knowledge of this greenhouse gas' transfer from the atmosphere into the ocean is important to improve climate models. Numerous problems occur at any attempt to adequately parameterize the transfer velocity across a wind-driven air-water interface like the ocean.

It is an accepted fact that wind enhances the transport velocities across the air-water interface by inducing turbulent transport and by generating waves. Depending on the parametrization used, predicted transfer rates at high wind speeds differ by a factor of two [37]. Looking into estimates of global CO₂ uptake into the ocean shows the magnitude of the problem. Takahashi et al. [65] compute a 70% difference in ocean CO₂ uptake between the parametrization of Wanninkhof [72] and Wanninkhof and McGillis [73].

The process of wave generation is extremely complex. The wind interacts with water, inducing waves by the means of momentum transfer. A process that depends both on wind speed and fetch¹. The waves interact with the wind field and with each other. The strength of interaction also depends on the surface tension, which might be locally modified by the presence of surfactants.

The effect of turbulence on the other hand is better understood. In the Prandtl layer, the lowest 50 m of the atmosphere, where the effects of pressure gradients and the Coriolis effect can be neglected, the wind velocity profile has a logarithmic shape. This can be explained by the fact that the turbulence induced transport is proportional to

¹In oceanography the word 'fetch' refers to the length of an area where waves are being generated by the wind.

the distance from the surface [58]. That result is connected to the notion of turbulent eddies whose size is limited by the distance to the surface they cannot pass through. Usually, turbulent transport velocities exceed those of molecular diffusion by several orders of magnitude. Very close to the surface though the turbulence is dampened and molecular diffusion dominates the transport, resulting in the so called boundary layer.

As the transport across the boundary layer is very slow, it is this layer that predominately determines the transport velocity of a substance to the surface. In air it typically has a thickness of 1-10 mm. In water it is frequently below 250 μm thick. Depending on a variety of conditions and properties like wind-speed and diffusivity, 50%-70% of the air-sided transfer resistance is located in this boundary layer. In water the effect is even more dramatic. For many substances, nearly the entire transport resistance is located in the boundary layer.

Measuring the concentration profile of a tracer near the air-water interface, and thus the boundary layer, allows a direct, local and real-time examination of the transport across the air-water interface in a laboratory experiment. Due to the local nature of such a measurement approach, uncertainties introduced by the overall flow field in a wind-wave tank are removed from the measurement. These measurements can also be combined with current wave-field acquisition methods like a CISG [57] and/or with heat transfer measurements [59]. The former might yield insights into the interaction of the wave-field and the boundary layer while the latter could serve to monitor the analogy of heat and concentration transport across the air-water interface.

The visualization of concentrations in a variety of fluids using laser induced fluorescence (LIF) has been a common technique used in the study of reacting liquid flows [71] and in combustion engine diagnostics [27] for more than 20 years. Based on those studies, the visualization of the water-sided boundary layer was pursued successfully: Wolff and Hanratty [75] successfully visualized the transfer of oxygen by measuring oxygen quenching while Münsterer and Jähne [46] report measurements of the transport of HCL using an pH-indicator based technique.

While there is ongoing research in water-sided LIF visualization of the boundary layer [20, 22, 28], trying to accomplish 3-dimensional time resolved measurements, there is no established technique for air-sided measurements at the air-water interface. In fact, to the author's knowledge, no air-sided profile measurements have been reported.

1.2 Goal

By applying knowledge gained in two separate fields of research, this study intends to realize the first air-sided LIF concentration profile measurements near a wind-driven

air-water interface and to provide a set of suitable tracer substances for the study of solubility effects on the transport process.

Based on insights provided by combustion engine studies [26, 30, 66], a new LIF setup was constructed which is suitable for air-sided measurements. A UV-laser system was chosen as excitation source as the fluorescence of many volatile organic substances of interest to gas exchange studies can be excited by UV light. However, in combustion engine diagnostics a single tracer of high sensitivity is usually enough. This limits the field as a data source.

Fortunately, the fluorescence characteristics of a multitude of organic substances were studied in great detail in the middle of the last century to optimize liquid scintillators for the detection of β -particles [1, 7, 56]. The solubility of a substance plays an important role in the transport and distribution of a tracer substance across the air-water interface. Slightly soluble substances should have no noteworthy air-sided concentration decrease. In consequence, only substances of moderate to high solubility are of interest for air-sided measurements. Especially the substances whose transport is controlled by both sides of the interface are barely understood at this point. To get solubility dependent results, that allow for a deeper insight into the transport processes, a large number of tracers featuring different solubilities and a high fluorescence sensitivity was needed.

1.3 Overview

This work is divided into three parts. Part I provides the necessary theoretical background, part II describes the used methods, experimental setups and procedures, and part III presents the measurements, results and conclusions.

Part I - Background Chapter 2 describes the concepts and parameters involved in the air-water gas exchange. The theoretically expected shape of air-sided profiles and the effect of solubility are explained herein. In chapter 3, the physical processes involved in fluorescence light generation are described, and chapter 4 provides a brief introduction into the field of absorption spectroscopy as far as needed in the course of this study.

Part II - Experimental Methods In chapter 5, LIF is described as an applied measurement technique. In addition, the definition of the signal rating SR , a figure of merit used throughout this study for tracer comparison, is given along with means for its measurement. The setups built during the course of this work are described in chapter 6, while the experimental procedure, data acquisition and processing are detailed in chapter 7.

Part III - Measurements and Results Chapter 8 presents an extensive overview of the characteristics of ten different tracers used for profile measurements obtained by literature review and measurements. Subsequently, chapter 9 provides an analysis of the measurements in terms of tracer sensitivity and transport across the air-water interface. Finally, the conclusion and outlook that can be gained from this study are presented in chapter 10.

Part I

Background

2 Gas Transfer at the Air-Water Interface

Volatile substances cross the air-water interface from the air into the water and vice versa. An inert substance has two channels of transport available: transport by molecular diffusion and transport via turbulent motion. Of these two processes, turbulent transport is the faster and thus more efficient within the air and water body on each side of the interface. However, turbulent motion is unable to cross the phase boundary between air and water. Consequently, the turbulent transport is effectively suppressed near the interface and molecular diffusion begins to dominate the process as the turbulent transport is more and more inhibited. Molecular transport on the other hand is negligibly slow compared to turbulent transport within the bulk of the air and water phase.

2.1 Turbulent-Diffusive Flows

The transport of tracer concentrations and the propagation of momentum in a flow field is governed by molecular diffusion and by turbulent transport. Both transport processes work to compensate for concentration differences. Reynolds deduced from his experiments that the parameters of a turbulent flow like the velocity u_i and the concentration c can be written as the sum of the temporal mean (\bar{u}_i, \bar{c}) of the respective property and its temporal variation (u'_i, c'). This so called Reynolds approach allows for a separate treatment of the diffusive and turbulent fraction of the transport.

$$u_i = \bar{u}_i + u'_i \quad \text{with} \quad (2.1)$$

$$\bar{u}_i = \frac{1}{T} \int_0^T u_i dt \quad \text{and} \quad u'_i = u_i - \bar{u}_i$$

$$c = \bar{c} + c' \quad \text{with} \quad (2.2)$$

$$\bar{c} = \frac{1}{T} \int_0^T c dt \quad \text{and} \quad c' = c - \bar{c}$$

The fluid velocity u_i consists of three components in the directions $[x, y, z]$. The integration time T has to be chosen sufficiently long, so that the temporal mean of the fluctuations u'_i and c' is zero.

The property of interest when speaking of transport is the flux density j_c , i.e. the flux of a certain property per unit area. In the case of a concentration flux, j_{c_i} equals $c u_i$. If the observed property is the flux of momentum, $j_{m_i,j}$ equals $\rho u_i u_j$

Purely diffusive molecular exchange is described by Fick's 1st law:

$$\vec{j}_c = -D\nabla c \quad (2.3)$$

It states that the diffusion driven flux density j is proportional to the negative local concentration gradient ∇c . The constant of proportionality D is called diffusivity and describes the mobility of a tracer within the fluid. A higher diffusivity and concentration gradient result in a higher flux density.

The mean flux density j_{c_i} for concentration transport, using equations (2.2) and (2.1), is:

$$\begin{aligned} j_{c_i} &= \overline{(\bar{c} + c')(\bar{u}_i + u'_i)} \\ &= \overline{\bar{c}\bar{u}_i} + \overline{\bar{c}u'_i} + \overline{c'\bar{u}_i} + \overline{c'u'_i} \\ &= \bar{c}\bar{u}_i + \overline{\bar{c}u'_i} + \overline{c'\bar{u}_i} + \overline{c'u'_i} \\ &= \bar{c}\bar{u}_i + \overline{c'u'_i} \end{aligned} \quad (2.4)$$

The first term of (2.4) describes the advective transport driven by the mean velocity. The second term represents the turbulent transport and is proportional to the correlation of the fluctuations of two properties whose individual temporal mean is zero. In other words: If the fluctuation of the concentration and velocity are totally uncorrelated, the resulting turbulent flux disappears.

Adding the term for molecular diffusion from Fick's 1st law (2.3) to equation (2.4), the resulting total flux is:

$$j_{c_i} = \bar{c}\bar{u}_i + \overline{c'u'_i} - D\nabla\bar{c} \quad (2.5)$$

Using the continuity equation $\partial c/\partial t = -\nabla\vec{j}$, the transport equation for the mean concentration becomes:

$$\frac{\partial\bar{c}}{\partial t} = -\sum_i \left[\frac{\partial}{\partial x_i}(\bar{c}\bar{u}_i) + \frac{\partial}{\partial x_i}(\overline{c'u'_i}) \right] + D\Delta\bar{c} \quad (2.6)$$

Applying the same method as described above to the momentum flux, but considering that now there are two vectorial properties, the following formulation can be derived:

$$j_{m_{i,j}} = \rho(\bar{u}_i \bar{u}_j) + \rho(\overline{u'_i u'_j}) - \rho \nu \nabla \bar{u}_i \quad \text{with} \quad \nu = \frac{\eta}{\rho} \quad (2.7)$$

The last term describes the diffusion of momentum by molecular interaction. ν is the kinematic viscosity, defined as the dynamic viscosity η divided by the fluid density ρ . Using the continuity equation, the transport equation of momentum becomes:

$$\frac{\partial \bar{u}_i}{\partial t} = -\rho \sum_{j=x,y,z} \left[\frac{\partial}{\partial x_j} (\bar{u}_i \bar{u}_j) + \frac{\partial}{\partial x_j} (\overline{u'_i u'_j}) \right] + \rho \nu \Delta \bar{u}_i \quad (2.8)$$

The flux equations (2.5) and (2.7) can be significantly simplified for a stationary flow in x -direction directly at the interface ($z = 0$, $\bar{u}_{y,z} = 0$). The only possible gradients are in z -direction; consequently all fluctuations in other planes than the x, z -plane disappear, resulting in the following equations:

$$-j_c = D \frac{\partial \bar{c}}{\partial z} - \overline{c' u'_z} \quad (2.9)$$

$$-j_m = \rho \nu \frac{\partial \bar{u}_x}{\partial z} - \overline{\rho u'_x u'_z} \quad (2.10)$$

Here j_c is the concentration flux density and j_m is the momentum flux density. The first term of equation (2.9) and (2.10) can be interpreted as the transport via molecular diffusion with the kinematic viscosity ν times the density ρ in the case of momentum transport as a constant of proportionality, as governed by Fick's 1st Law.

The second term describes the influence of the turbulence on the transport process. If there is no correlation between the observed property's fluctuations (i.e. concentration or velocity in x -direction) and the fluctuations of the velocity field in z -direction this term vanishes per definition of the fluctuations above. A higher correlation results in a greater influence of turbulence on the flux density and thus the transport process.

A well established model that will be used in the following sections is the definition of a turbulent diffusion coefficient K that is used to describe the correlation term in the equations (2.5) and (2.7) in a way equivalent to the molecular diffusion.

$$-K_c(z) \frac{\partial \bar{c}}{\partial z} = \overline{c' u'_z} \quad (2.11)$$

$$-K_m(z) \frac{\partial \bar{u}_x}{\partial z} = \overline{u'_x u'_z} \quad (2.12)$$

$K_c(z)$ is the turbulent diffusion coefficient. $K_m(z)$ is the turbulent viscosity. Both are dependent on the height z in a so far undefined fashion. Applying this model to the flux density (2.9) and (2.10), the following equations describe the transport process:

$$j_c = (D + K_c(z)) \frac{\partial c}{\partial z} \quad (2.13)$$

$$j_m = \rho(\nu + K_m(z)) \frac{\partial u_x}{\partial z} \quad (2.14)$$

2.1.1 Shear Stress and Friction Velocity

An important parameter that can be derived from equation (2.7) is the turbulent shear stress, also called 'Reynolds stress' τ . It is the turbulent component of the vertical flux density of the horizontal momentum, $j_{m,\text{turbulent},x,z}$. Equation (2.7) gives:

$$j_{m_{x,z}} = \rho(\bar{u}_x \bar{u}_z) + \rho(\overline{u'_x u'_z}) - \rho \nu \nabla^2 \bar{u}_x \quad (2.15)$$

The first term gives the mean contribution of the flow. It usually vanishes near the interface as the mean velocity in z direction is zero. The third term represents the contribution of the diffusive momentum transport while the second term is the wanted formulation of the turbulent shear stress.

$$\tau = j_{m,\text{turbulent},x,z} = \rho(\overline{u'_x u'_z}) \quad (2.16)$$

For many applications, it proved practical to define another parameter - the friction velocity u_* :

$$u_* = \sqrt{\frac{|\tau|}{\rho}} = \sqrt{\overline{u'_x u'_z}} \quad (2.17)$$

The friction velocity u_* is constant in a flow field without a velocity variation in y -direction in heights in which the dynamic viscosity does not matter i.e. far away from the surface, since the downward transported momentum flux has to be conserved.

2.2 Velocity and Concentration Profiles

A significant problem when working with equations (2.13) and (2.14) is the depth dependence of the turbulent diffusion coefficient K , which is in general not known. The wind-profile, i.e. the depth resolved wind-speed however, has been studied in detail. The models can be transferred with relative ease to concentration profiles.

A widely used and comprehensible approach is the separation of the transport process into two layers: one far away from the turbulence inhibiting surface where the process is entirely controlled by turbulence; and another layer close to the surface, where the transport is dominated by molecular diffusion. The second layer is called the viscous boundary layer. The profiles corresponding to these two separate layers can later be merged into a single profile, describing the depth dependent velocity or concentration.

2.2.1 Turbulent Layer

Assuming there is no influence of the diffusive transport, the velocity profile du_x/dz can only depend on the constant friction velocity u_* and the height z above the surface. The only way to combine these parameters that results in the depth dependence of the velocity (du_x/dz) is:

$$\frac{du_x}{dz} = \frac{1}{\kappa} \frac{u_*}{z} \quad (2.18)$$

The constant of integration κ is known as the 'von Karman constant'. Its value is 0.41 [14]. Using equation (2.14), the shear stress τ can be formulated as:

$$\tau = j_{m,\text{turbulent},x,z} = \rho K_m(z) \frac{\partial u_x}{\partial z} \quad (2.19)$$

Combining the above equations with the friction velocity (2.17), the turbulent diffusion coefficient K_m (2.14) can be determined directly:

$$\begin{aligned} (2.17) \quad \tau &= \rho u_*^2 \\ (2.18) + (2.19) \quad \tau &= \rho K_m(z) \frac{1}{\kappa} \frac{u_*}{z} \\ \Rightarrow K_m(z) &= \kappa u_* z \end{aligned} \quad (2.20)$$

By integration of (2.18), the velocity profile becomes:

$$u_x(z) = \frac{u_*}{\kappa} \ln \frac{z}{z_0} \quad (2.21)$$

The constant of integration z_0 , also called the roughness parameter, depends on the nature of the surface the velocity field moves along. z_0 must be determined experimentally. This has been done for the wind-wave tank utilized in this study (see appendix A). An upper limit for the friction velocity u_* and the roughness parameter z_0 for the wind velocities used are $u_* < 20 \text{ cm/s}$ and $z_0 < 0.002 \text{ cm}$.

The Reynolds number Re can be used to determine whether the observed surface has to be considered rough or slick.

$$Re = \frac{u_* z_0}{\nu} \quad (2.22)$$

With the kinematic viscosity of air $\nu = 0.145 \text{ cm}^2/\text{s}$, the resulting Reynolds number is $Re < 0.27$. According to Nikuradse [50], a surface must be considered rough for $Re > 2.5$. This is clearly not the case. On the other hand, a surface can only be considered perfectly smooth with absolute certainty for $Re < 0.13$. The profiles presented here assume a smooth surface. This is in agreement with Deacon [14], who gets very good results for his calculation of gas exchange rates for friction velocities u_* of up to 30 cm/s by making the same assumption. For a smooth surface, z_0 can be approximated with $z_0 \approx \nu/9 u_*$ [58]. This gives the logarithmic velocity profile:

$$u_x(z) = \frac{u_*}{\kappa} \ln \frac{u_* z}{\nu} + 5.36 u_* \quad (2.23)$$

2.2.2 Viscous Boundary Layer

The viscous boundary layer is the region just above the water surface, where the molecular diffusion dominates the transport process. As a first simple approximation, the turbulent diffusion K_m can be considered zero for the height of the boundary layer. Equation (2.14) solved for $\partial u_x / \partial z$ becomes:

$$\frac{\partial u_x}{\partial z} = \frac{j_m}{\rho \nu} \quad (2.24)$$

The momentum flux above is the positive flux of momentum into the surface, resulting in a reversal of the sign. By defining a diffusive shear stress and friction velocity in the same way as in equation (2.16) and (2.17) for the turbulent shear stress, integration yields the following velocity profile in the viscous boundary layer:

$$u_x(z) = \frac{j_m}{\rho\nu} z \quad \text{with} \quad j_m = \tau = \frac{u_*}{\rho} \quad (2.25)$$

$$\Rightarrow u_x(z) = \frac{u_*^2}{\nu} z \quad (2.26)$$

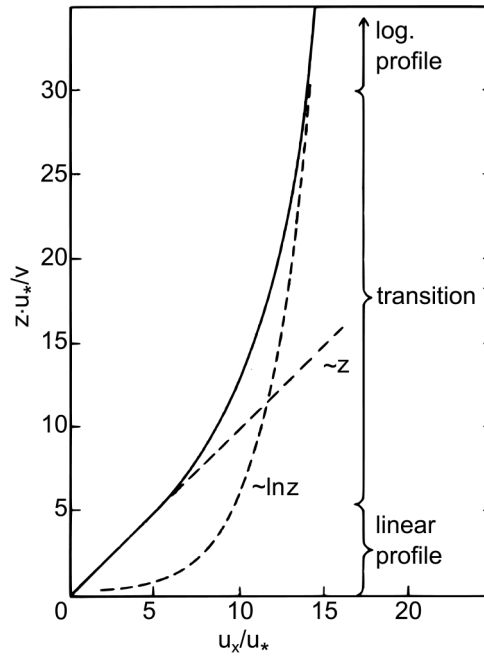


Figure 2.1: The dimensionless velocity u_x/u_* plotted against the dimensionless height $z u_*/\nu$. Near the surface, the profile is proportional to the height z . Far away from the surface, the profile becomes logarithmic. (Adopted from Roedel [58])

While the molecular diffusion dominates the transport process in the viscous boundary layer, the turbulent diffusion can still play a role. Especially when describing the transport of molecular tracers as their diffusion constant might differ greatly from the kinematic viscosity of air.

Equation (2.13), when solved for the turbulent diffusion coefficient, reads:

$$K_m(z) = \frac{j_m}{\rho \frac{\partial u_x}{\partial z}} - \nu \quad (2.27)$$

This suggests that the turbulent diffusion coefficient can be directly derived from the velocity profile. While the profile is not known, the viscous boundary layer is only a very small subsection of the profile. By approximating the velocity field by a Taylor series

at the surface, $K_m(z)$ within the boundary layer can be determined. This approach was first published by Coantic [10]. This model, also known as the 'small eddy model', assumes that the fluctuations u'_x can be considered small in comparison to the mean velocities \bar{u}_x . The Taylor series of the mean velocity at the surface reads:

$$\bar{u}_x(z) = \bar{u}_x(0) + \sum_{n=1}^{\infty} \frac{1}{n!} \left. \frac{\partial^n \bar{u}_x(z)}{\partial z^n} \right|_{z=0} \cdot z^n \quad (2.28)$$

Observation shows that the velocity of fluid particles directly at a non moving surface is zero, and all but the diffusive transport vanishes. Equation (2.10), for zero velocities, gives for the first order derivative:

$$\frac{\partial \bar{u}_x}{\partial z} = \frac{j_m}{\rho \nu} \quad (2.29)$$

In order to get the second order derivative of \bar{u}_x equation (2.8) applied to a stationary, one dimensional flow is needed:

$$\begin{aligned} \frac{\partial}{\partial t} \bar{u}_x &= \rho \frac{\partial}{\partial z} \left(\nu \frac{\partial}{\partial z} \bar{u}_x - \overline{u'_x u'_z} \right) = 0 \\ \Rightarrow \frac{\partial^2}{\partial z^2} \bar{u}_x &= \frac{1}{\nu} \frac{\partial}{\partial z} \overline{u'_x u'_z} \end{aligned} \quad (2.30)$$

Higher order derivatives can be calculated by gradual derivation of equation (2.30).

$$\frac{\partial^n}{\partial z^n} \bar{u}_x = \frac{1}{\nu} \frac{\partial^{n-1}}{\partial z^{n-1}} \overline{u'_x u'_z} \quad (2.31)$$

The derivatives of the velocity up to 4th order are:

$$\left. \frac{\partial^2}{\partial z^2} \bar{u}_x \right|_{z=0} = \frac{1}{\nu} \left[\overline{u'_z \frac{\partial u'_x}{\partial z}} + \overline{u'_x \frac{\partial u'_z}{\partial z}} \right]_{z=0} \quad (2.32)$$

$$\left. \frac{\partial^3}{\partial z^3} \bar{u}_x \right|_{z=0} = \frac{1}{\nu} \left[\overline{u'_z \frac{\partial^2 u'_x}{\partial z^2}} + 2 \overline{\frac{\partial u'_z}{\partial z} \frac{\partial u'_x}{\partial z}} + \overline{u'_x \frac{\partial^2 u'_z}{\partial z^2}} \right]_{z=0} \quad (2.33)$$

$$\left. \frac{\partial^4}{\partial z^4} \bar{u}_x \right|_{z=0} = \frac{1}{\nu} \left[\overline{u'_z \frac{\partial^3 u'_x}{\partial z^3}} + 3 \overline{\frac{\partial u'_z}{\partial z} \frac{\partial^2 u'_x}{\partial z^2}} + 3 \overline{\frac{\partial^2 u'_z}{\partial z^2} \frac{\partial u'_x}{\partial z}} + \overline{u'_x \frac{\partial^3 u'_z}{\partial z^3}} \right]_{z=0} \quad (2.34)$$

This set of equations can be simplified considerably by adding the boundary conditions for the specific problem of the turbulent flow directly at the surface of a rigid wall. The

water surface is considered to be an unmoving obstacle for the flow of air since the air density is about three orders of magnitude smaller. At $z = 0$ all velocity fluctuations have to be zero as the particles at the surface are considered to be stationary.

$$u'_x = u'_y = u'_z = 0 \Big|_{z=0} \quad (2.35)$$

With no movement along the surface (x, y -direction), the continuity equation for incompressible fluids $\nabla u' = 0$ gives:

$$\nabla u' = \frac{\partial u'_x}{\partial x} + \frac{\partial u'_y}{\partial y} + \frac{\partial u'_z}{\partial z} = 0 \quad (2.36)$$

$$\Rightarrow \frac{\partial u'_z}{\partial z} \Big|_{z=0} = 0 \quad (2.37)$$

With these boundary conditions, most of the individual derivatives above become zero. Putting everything together, the Taylor series for the mean velocity in x -direction \bar{u}_x becomes:

$$\begin{aligned} \bar{u}_x &= \bar{u}_x(0) + \frac{j_m}{\rho\nu} z + \frac{1}{24\nu} \overline{3 \frac{\partial^2 u'_z}{\partial z^2} \frac{\partial u'_x}{\partial z}} z^4 \\ &= \bar{u}_x(0) + \frac{j_m}{\rho\nu} z + \frac{1}{24\nu} \alpha z^4 \end{aligned} \quad (2.38)$$

α is assumed to be constant in this approximation. Two more steps are necessary to get a final approximation of the turbulent diffusion near the water surface. The first is to calculate the derivative in z of equation (2.38)

$$\frac{\partial \bar{u}_x}{\partial z} = \frac{j_m}{\rho\nu} + \frac{1}{6\nu} \alpha z^3 \quad (2.39)$$

And putting this into equation (2.27).

$$\begin{aligned} K_m(z) &= -\nu \left(1 - \frac{1}{\underbrace{1 - \frac{\rho}{6j_m} \alpha z^3}_{\frac{1}{1-x} \approx 1 + \frac{1}{2}x + x^2 \dots \text{ for } -1 < x < 1}} \right) \\ \Rightarrow K_m(z) &\approx \frac{\rho\nu}{12j_m} \alpha z^3 = \text{const} \cdot z^3 \end{aligned} \quad (2.40)$$

As shown above, the second addend can be approximated by a power series for small z , giving the final correlation between the height z and the turbulent diffusion coefficient K_m in the viscous boundary layer.

2.2.3 Interpolated Profile

The results acquired above give a formulation for the turbulent diffusion coefficient near the water surface, where the velocity or concentration is proportional to the distance z from the interface and within the bulk, where the profile has a logarithmic shape. For many applications, when the interest is in total transfer velocities, this knowledge is adequate. The logarithmic shape of the profile in the bulk can be used to estimate the friction velocity u_* by fitting equation (2.23) to a measured wind velocity profile. The linear slope of the concentration profile combined with a measurement of the bulk concentration can be used to determine the mass boundary layer thickness, as described in section 2.3, thus providing information about the transfer velocity k .

One aim of this study is to achieve the measurement of concentration profiles in air. To get an idea of what to expect, it is necessary to get a description of the total transfer profile. Reichardt [55] provided an interpolated solution for the depth dependence of $K(z)$ in his studies of turbulence in tubes and channels. His formulation is based on the above presented results of the depth dependence of the turbulence. A satisfactory interpolation was found by iterative comparison with experimental results. The gist of his study is the following formulation for the depth dependence of $K(z)$:

$$K(z) = \kappa u_* z_0 \left(\frac{z}{z_0} - \tanh \frac{z}{z_0} \right) \quad (2.41)$$

As before, κ is the von Karman constant with a value of 0.41. Reichardt [55] provides a value for $z_0 = 11.7\nu/u_*$ to fit the model to experimental data. For large values of z the $\tanh(z/z_0)$ tends to 1 and $K(z)$ is linear dependent on the height, as necessary for a logarithmic profile. For small values of z the $\tanh(z/z_0)$ can be approximated by its Taylor series:

$$\begin{aligned} \tanh(x) &= x - \frac{1}{3}x^3 + \dots \\ \Rightarrow K(z) &= \kappa u_* z_0 \frac{1}{3} \left(\frac{z}{z_0} \right)^3 \\ K(z) &= \text{const} \cdot z^3 \end{aligned} \quad (2.42)$$

For small values of z , equation (2.41) tends to $K(z) \sim z^3$ - equal to what was found in (2.40).

2.3 Transfer Resistance and Velocity

Equation (2.13) states that the flux density j_c is the result of a concentration difference $\partial C/\partial z$ times a proportionality coefficient $(D + K_c(z))$. For a stationary process, the flux density j_c is constant, allowing a calculation of the concentration difference between two heights $z_1 < z_2$ by integration:

$$c(z_1) - c(z_2) = j_c \int_{z_1}^{z_2} \frac{1}{K_c(z) + D} dz \quad (2.43)$$

By dividing both sides of this equation by the flux density $-j_c$, a new parameter can be defined that is, in analogy to Ohm's law, called the transfer resistance R :

$$R_{2,1} = \frac{c(z_1) - c(z_2)}{j_c} = \int_{z_1}^{z_2} \frac{1}{K_c(z) + D} dz \quad (2.44)$$

The concentration difference (which is equivalent to the potential difference in Ohm's law) is proportional to the transfer resistance times the flux density (an equivalent to the electric current).

Another useful parameter is the transfer velocity k , that is defined as the reciprocal of the transfer resistance R and thus equivalent to a conductivity:

$$k_{2,1} = \frac{1}{R_{2,1}} = \frac{j_c}{c(z_1) - c(z_2)} \quad (2.45)$$

Several transport resistances corresponding to different heights of the concentration profile can be added up to get the total resistance. When using transfer velocities, the reciprocals add up:

$$R_{3,1} = R_{2,1} + R_{3,2} \quad (2.46)$$

$$\frac{1}{k_{3,1}} = \frac{1}{k_{2,1}} + \frac{1}{k_{3,2}} \quad (2.47)$$

This is in equivalence to a series circuit of resistances with constant current in electrostatics.

2.3.1 Boundary Layer Thickness

In previous sections the boundary layer, which thickness could not easily be defined, has already been mentioned. A common and helpful formulation is the 'stagnant film model'. This model assumes a boundary layer as a contrived layer on both sides of the air-water interface where the transport flux is maintained only by molecular diffusion. This idea originates from the notion that the turbulence is diminished near the surface and zero at the surface. Directly at the surface, excluding transport via turbulence, equation (2.13) becomes:

$$j_c = D \left. \frac{\partial C}{\partial z} \right|_{z=0} \quad (2.48)$$

This suggests that the flux density can be calculated by the gradient of the concentration profile directly at the surface if the diffusion coefficient is known. The idea of the boundary layer is that the total concentration decline Δc between the well mixed bulk c_b and the surface c_s occurs within the boundary layer by molecular diffusion.

$$\Delta c = c_b - c_s \quad (2.49)$$

Using equation (2.48), the thickness z_* of the boundary layer is defined as:

$$z_* = \frac{\Delta c}{\left. \frac{\partial C}{\partial z} \right|_{z=0}} = \frac{D \Delta c}{j_c} \quad (2.50)$$

With equations (2.44) and (2.45), the boundary layer thickness can directly be linked to the transfer resistance and velocity:

$$z_* = D R_{b,s} = \frac{D}{k_{b,s}} \quad (2.51)$$

$R_{b,s}$ and $k_{b,s}$ are the transfer resistance and transfer velocity between the bulk and the surface. The boundary layer can also be found geometrically if the concentration profile is known. It is the intercept of the tangent to the profile at the surface and the logarithmic shape of the bulk profile. This is shown in figure 2.2.

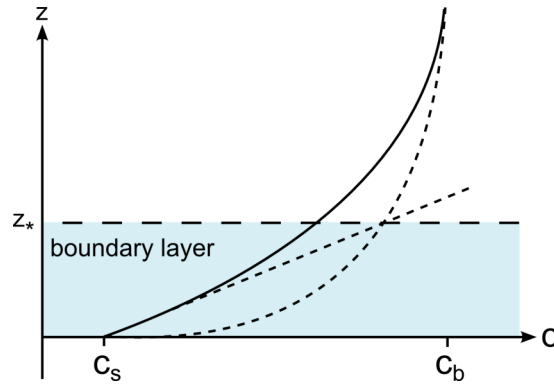


Figure 2.2: Geometric construction of the boundary layer. The solid line represents the actual profile. The dashed lines are the linear and logarithmic portion of the profile.

2.3.2 Air-Water Transfer Partition

When observing a transport process across the air-water interface, it is important to note that both the air- and the water-side take part in the process and provide a resistance to the transfer of molecular tracers. When observing the transport of a chemical admixture into the air down into the well mixed water bulk, it must overcome to a transfer resistance in air and water. The total resistance, as explained above, is the sum of the individual resistances. A peculiarity of the air-water boundary has to be taken into account into account.

To reach a thermodynamic equilibrium at the water surface, the surface concentration in water $c_{w,s}$ has to compensate for the solubility α of the tracer to reach equilibrium with the air-sided concentration $c_{a,s}$. The dimensionless solubility α^1 , as used in this study, is defined as the equilibrium concentration ratio between water and air for a dilute aqueous solution. In this context, dilute is typically defined as less than 0.001-0.01 mole fraction [63]:

$$\alpha = \frac{c_{w,s}}{c_{a,s}} \left[\frac{\text{mol}_w/\text{m}^3}{\text{mol}_a/\text{m}^3} \right] = \left[\frac{\text{g}_w/\text{m}^3}{\text{g}_a/\text{m}^3} \right] = [-] \quad (2.52)$$

Any solubility other than unity causes the concentration profile to have a discontinuity at the water surface. The concentration has to make a jump to accommodate for the requirement of a thermodynamic equilibrium. As the concentration flux density j_c has to be constant, this directly affects the transfer resistance and velocity. The total transfer resistance R_{tot} and the total transfer velocity k_{tot} become:

¹ α is also called the Ostwald solubility and is equal to the reciprocal of the dimensionless Henry's Law Constant k_H . It is important to note that there are several ways to define this value. Staudinger and Roberts [63] provide an overview and conversion factors for the various definitions.

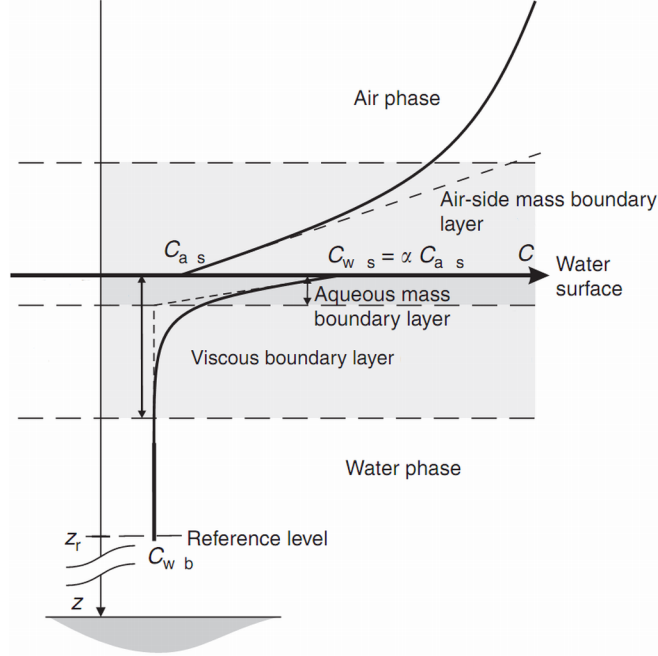


Figure 2.3: Transport of a tracer with solubility $\alpha = 3$ across the air-water interface. Due to the similar values for the viscosity ν_a of air and the diffusion coefficient D_a of most tracers in air, the viscous boundary layer is of about the same height as the mass boundary layer corresponding to concentration transfer. In water, the situation can differ significantly. (Figure adopted from Jähne [37])

$$R_{\text{tot}}^A = R_a + \frac{R_w}{\alpha} \quad (2.53)$$

$$\frac{1}{k_{\text{tot}}^A} = \frac{1}{k_a} + \frac{1}{\alpha k_w} \quad (2.54)$$

When the process is viewed from the water-side, the factor α applies the air-sided values instead:

$$R_{\text{tot}}^W = \alpha \cdot R_a + R_w \quad (2.55)$$

$$\frac{1}{k_{\text{tot}}^W} = \frac{\alpha}{k_a} + \frac{1}{k_w} \quad (2.56)$$

The total transfer resistance observed from the air-side $R_{a,\text{tot}}$ is smaller by factor α than the total resistance $R_{w,\text{tot}}$ observed water-sided:

$$\frac{R_{\text{tot}}^A}{R_{\text{tot}}^W} = \frac{R_a + \frac{R_w}{\alpha}}{\alpha \cdot R_a + R_w} = \frac{1}{\alpha} \quad (2.57)$$

Figure 2.3 shows a sketch of the transfer process across the air-water interface.

2.3.3 Concentration Profiles

Deacon [14] applied the parametrization for the turbulent diffusion coefficient for momentum found by Reichardt [55] to the problem of gas transfer across a wind-driven water surface with great success. He assumed that the turbulent diffusion coefficient for mass transport K_m is equal to the turbulent diffusion coefficient for concentration transport K_c , but even differences as high as 30% would effect the result of his calculations by only 10%. Comparing his results to various experiments showed that formulation for K given above yields good results for low to moderate wind speeds.

In order to calculate the transfer resistance R_a , a concentration admixture faces when traveling from the well mixed air bulk at reference height z_r to the water surface, equation (2.44) has to be integrated:

$$\begin{aligned}
 R_a &= \int_0^{z_r} \frac{1}{K_c(z) + D} dz \\
 &= \int_0^{z_r} \frac{1}{\kappa u_* z_0 \left(\frac{z}{z_0} - \tanh \frac{z}{z_0} \right) + D} dz \\
 &= \frac{1}{D} \int_0^{z_r} \frac{1}{4.8 \cdot Sc \left(\frac{z}{z_0} - \tanh \frac{z}{z_0} \right) + 1} dz \quad \text{with } z_0 = \frac{11.7\nu}{u_*}, \kappa = 0.41 \quad (2.58)
 \end{aligned}$$

$Sc = \nu/D$ is the Schmidt number, a measure of the ratio between viscosity of a fluid and the diffusivity of a substance carried by the fluid.

A problem provided by this formulation is that it can only be integrated numerically. Deacon [14] got the following approximated results depending on Sc for the transfer resistance across the boundary layer. He states a deviation of no more than 1% compared to the numeric integration:

$$R_a \approx \frac{15.2}{u_*} \cdot Sc^{0.61} \quad Sc < 10 \quad (2.59)$$

$$R_a \approx \frac{12.1}{u_*} \cdot Sc^{\frac{2}{3}} \quad Sc > 10 \quad (2.60)$$

To get an idea what to expect when measuring air-sided concentration profiles, the concentration profile was calculated using equation (2.43) and the interpolated turbulent

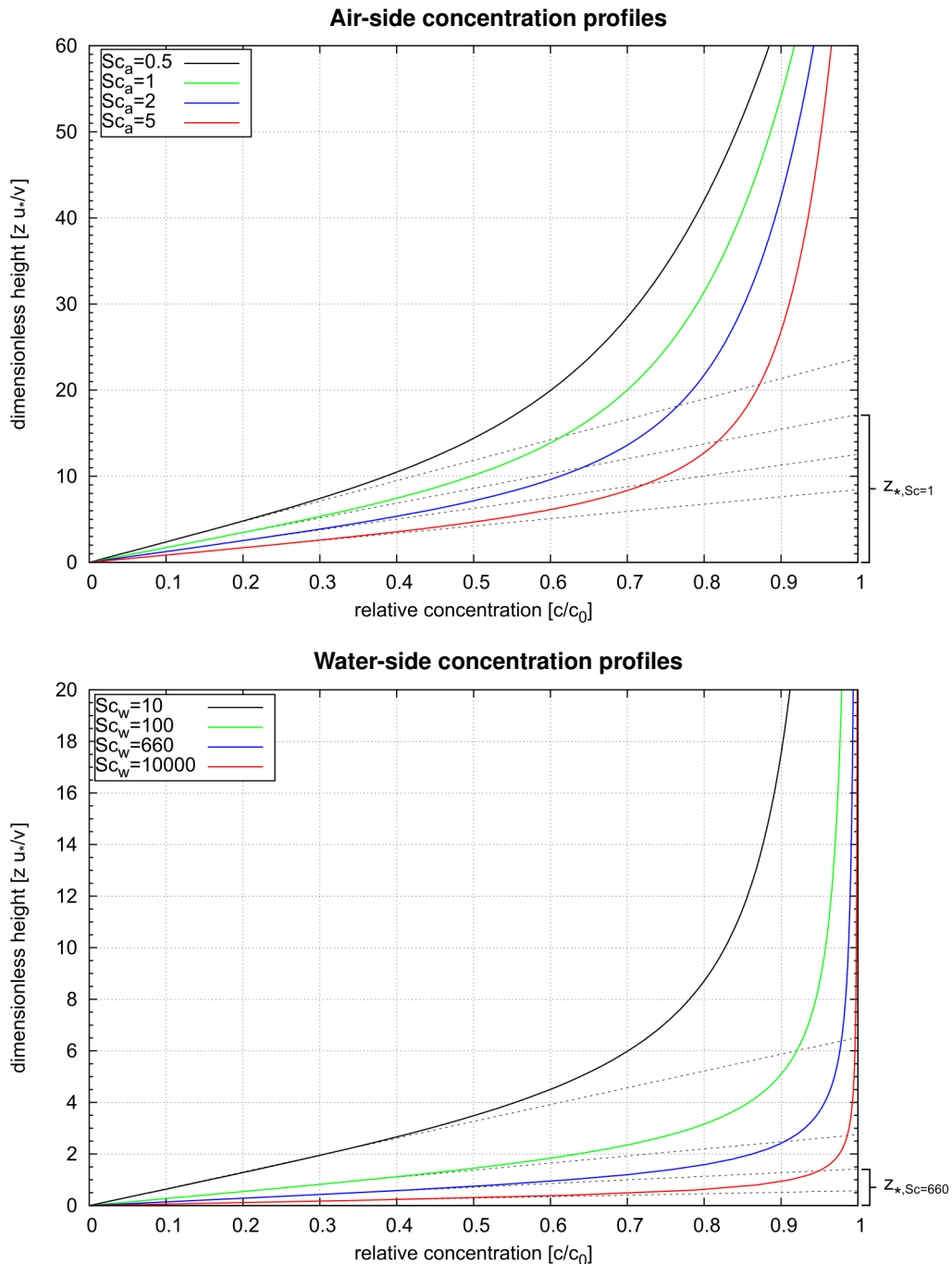


Figure 2.4: The shape of the concentration profiles using Reichardt’s interpolated formulation of the turbulent diffusion coefficient and a dimensionless height $z_+ = z u_*/\nu$. The various profiles correspond to different Schmidt numbers $Sc = \nu/D$. The dotted lines show the extrapolation of the surface concentration gradient. The interception of these lines with the bulk concentration ($c_{\text{bulk}} = 1$) is the mass boundary layer thickness z_* . The higher Schmidt numbers in water result in distinctly thinner boundary layers.

diffusion coefficient (2.41). The numeric integration was realized using Python and the external SciPy library. The results are shown in figure 2.4. The simulation used dimensionless parameters. $z_+ = z u_* / \nu$ was used for the height. With the kinematic viscosity of air ($\nu_a = 0.15 \text{ cm}^2/\text{s}$) and water ($\nu_w = 0.001 \text{ cm}^2/\text{s}$) at 20° C , the expected boundary layer thicknesses can be calculated. In air, the conversion factor for a friction velocity u_{*a} equals 20 cm/s is 0.0725 mm . To get the comparable water-sided conversion factor, u_{*w} is calculated using equation (2.17):

$$\frac{u_{*w}}{u_{*a}} = \sqrt{\frac{\rho_a}{\rho_w}}. \quad (2.61)$$

At 25° C , the density of water is 997 kg/m^3 and the density of air is 1.18 kg/m^3 , which results in a factor of $u_{*w}/u_{*a} = 1/29$. The conversion factor for the dimensionless height in water becomes 0.0145 mm .

The mass boundary layer thickness z_* is highly dependent on the Schmidt number Sc . While it usually is between 0.6 mm and 1.8 mm for the values of Sc_a in air, it can be far below 1 mm in water. CO_2 with a $Sc_w = 660$ would have a boundary layer thickness of $21.75 \mu\text{m}$ according to this calculation.

2.3.4 Controlling Phase

The solubility α plays a key role in the determination of the controlling phase boundary layer of the transport process. As seen above, the total transfer resistance is a sum of the individual transfer resistances, but one of these is modified by the solubility. The following derivation focuses on an air-sided perspective due to the nature of this study.

Equation (2.53) suggests that the ratio $\alpha R_a/R_w$ determines which side of the interface controls the transport process. If R_w is much bigger than αR_a , the total transfer resistance is located in the aqueous mass boundary layer. On the other hand, if αR_a is much bigger than R_w , the total resistance is in the air-side. In addition, there should be a ratio of transfer resistances where the transport process is controlled by both phases.

By using equation (2.59) for the air-sided boundary layer, and assuming that the same relationship holds true for the water-sided transfer resistance at a smooth water surface [37], it is possible to calculate the partition of the transfer resistance within the boundary layers of the air- and water-side:

$$\begin{aligned}\frac{\alpha R_a}{R_w} &= \frac{\alpha \frac{15.2}{u_{*a}} \cdot Sc_a^{0.61}}{\frac{12.1}{u_{*w}} \cdot Sc_w^{\frac{2}{3}}} \\ \frac{\alpha R_a}{R_w} &= 1.26 \alpha \frac{u_{*w}}{u_{*a}} \cdot \frac{Sc_a^{0.61}}{Sc_w^{\frac{2}{3}}}\end{aligned}\quad (2.62)$$

The Schmidt numbers Sc_a and Sc_w depend on the viscosity of and diffusivity of a tracer in air and water respectively. Schmidt numbers in water cover a considerably larger range than those in air. To simplify equation (2.62), Sc_a is assumed to be constant. For the tracers used in this study, $Sc_a = 1.75$ is a reasonable assumption resulting in a constant factor of $Sc_a^{0.61} = 1.4$. The ratio of the friction velocities is again calculated using equation (2.61) to be $1/29$. By making these assumptions and by writing the ratio of the transfer resistances as $r_{a,w} = R_a/R_w$, equation (2.62) becomes:

$$\alpha r_{a,w} = 0.06 \alpha Sc_w^{-\frac{2}{3}} \quad (2.63)$$

With Sc_w as well as α being physical properties of the measured transfer substance, (2.63) provides a way of sorting substances into an air- and water sided regime divided by a transition zone where both transfer resistances are of interest. A typical division of these three zones, as introduced by Jähne [35], has a transition zone $\alpha r_{a,w} = 0.1 - 10$. The transport of a tracer substance is equally controlled by both air- and water-side if $\alpha r_{a,w} = 1$. Substances above this level are assumed to be controlled by the air while substances below this level are assumed to show mainly water-sided control.

For a set ratio $\alpha r_{a,w}$, the solubility α can be given as a function of Sc_w :

$$\begin{aligned}\alpha r_{a,w} = 1 &= 0.06 \alpha Sc_w^{-\frac{2}{3}} \\ \Rightarrow \frac{1}{\alpha} &= 0.06 Sc_w^{-\frac{2}{3}} \\ \Rightarrow \alpha &= \frac{1}{0.06} Sc_w^{\frac{2}{3}}\end{aligned}\quad (2.64)$$

Figure 2.5 shows a range of different tracers and their position on a α/Sc_w diagram. When conceiving ways to measure the gas exchange, it can often be convenient to assume that the whole transport resistance is located in a single boundary layer, as the transfer rate measured in a single phase is effectively equivalent to the measurement of the total transfer resistance.

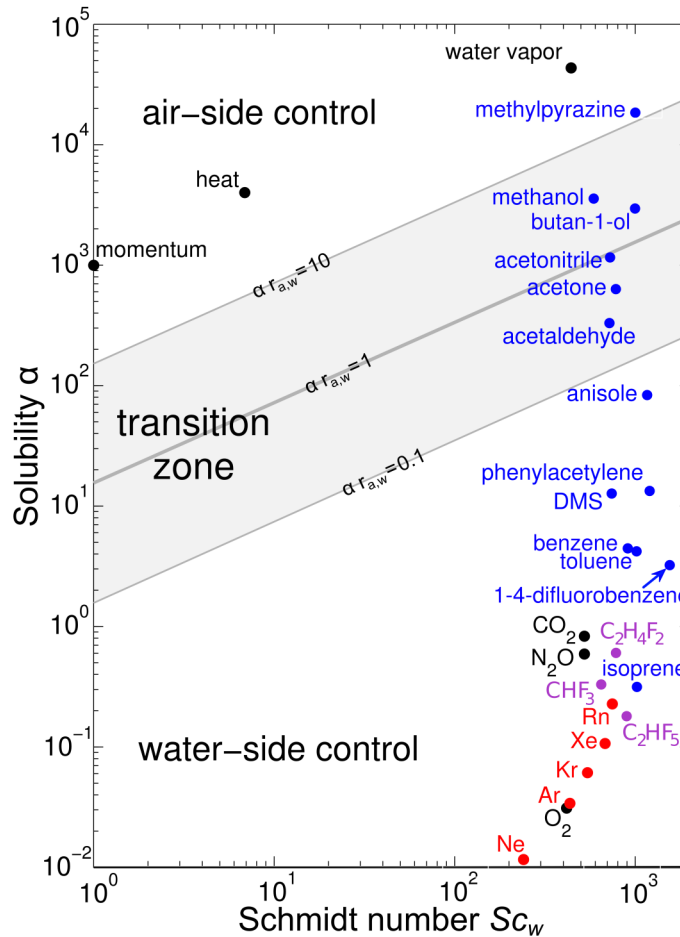


Figure 2.5: The solubilities α and water-sided Schmidt numbers Sc_w of a variety of tracer substances. The shaded area indicates the region of the transition zone calculated with (2.64), where the transport is controlled by both the air- and water-sided boundary layer. (Figure modified from Kräuter et al. [40])

Measuring the Resistance Partition When measuring concentration profiles, it is possible to directly determine the ratio of transfer resistances, and thus the controlling phase. Both the air-sided bulk concentration c_a and the air-sided surface concentration c_{as} can be directly taken from the measured profile. Equation (2.43), solved for the concentration flux j_c , which is constant, becomes:

$$j_c = \frac{c_a - c_{as}}{R_a} = \frac{c_{ws} - c_w}{R_w} \quad (2.65)$$

Here c_{ws} is the surface concentration in the water and c_w is the concentration in the well mixed lower bulk of the water. By assuming an invasion experiment in which the bulk concentration in the water c_w is zero, as is the case for the experiments

conducted within this study, and by using the definition of the solubility α , equation (2.65) becomes:

$$j_c = \frac{c_a - c_{as}}{R_a} = \frac{\alpha c_{as}}{R_w} \quad (2.66)$$

The ratio of the resistances $r_{a,w}$ becomes:

$$\frac{R_a}{R_w} = \frac{c_a - c_{as}}{\alpha c_{as}} \quad (2.67)$$

As the profiles only provide the concentration in the bulk and at the surface, it is helpful to instead solve equation (2.66) for the concentration ratio $c_r = c_{as}/c_a$:

$$\begin{aligned} \frac{c_a - c_{as}}{R_a} &= \frac{\alpha c_{as}}{R_w} \\ \frac{c_a}{R_a} &= c_{as} \left(\frac{\alpha}{R_w} + \frac{1}{R_a} \right) \\ c_a &= c_{as} \left(\frac{\alpha R_a}{R_w} + 1 \right) \\ c_r = \frac{c_{as}}{c_a} &= \frac{1}{\frac{\alpha R_a}{R_w} + 1} \end{aligned} \quad (2.68)$$

For a substance whose transfer resistance is located only in the water-side, $R_w \gg \alpha R_a$, $\alpha R_a/R_w$ becomes zero and $c_r = 1$. The profile is constant; there is no decrease of the air-sided concentration. For air-side controlled substances $\alpha R_a \gg R_w$, resulting in $c_r = 0$, the high solubility acts as a short-circuit for the water-sided transfer resistance. If the water-sided transfer resistance is just high enough to cancel the effect of the solubility, $R_a/R_w = 1/\alpha$, the concentration ratio becomes $c_r = 0.5$ and the transfer process is equally controlled by each side of the interface. The transition zone, with $r_{a,w} = R_a/R_w = 0.1 - 10$, has concentration ratios of $c_r = 0.5$

Air-Water Signal Partition The fluorescence signal is proportional to the tracer concentration (see chapter 3 and chapter 5). At the interface the solubility determines the concentration in air and water. When measuring the signal of a fluorescent tracer in air the camera needs to cover the signal generated by the air- and water-side. If there is no limit to this partition the signal of highly soluble tracers cannot be covered with most camera systems.

The concentration ratio c_{aw} between the bulk of the air phase and the surface of the water phase and thereby the signal ratio can be calculated by combining equations (2.52) and (2.68):

$$c_{aw} = \frac{\alpha a_s}{c_a} = \frac{c_{ws}}{c_a} = \frac{\alpha}{\frac{\alpha R_a}{R_w} + 1} = \frac{\alpha R_w}{\alpha R_a + R_w} \quad (2.69)$$

For a solubility $\alpha = 0$ the concentration ratio c_{aw} is zero. For an equal partition of the transfer resistances with $\alpha = R_w/R_a$ it becomes $R_w/2R_a$. For the critical case of a very high solubility $\alpha = \infty$ the concentration ratio is $c_{aw} = R_w/R_a$ resulting in the following correlation between the air-sided bulk concentration c_a and the water-sided surface concentration c_w :

$$c_w = \frac{R_w}{R_a} c_a \quad (2.70)$$

Not only are signal dynamics limited by the ratio of the transfer resistances, in the case of high solubilities the ratio of the resistances can be directly measured if both the air-sided bulk concentration and the water-sided surface concentration can be acquired.

3 Fluorescence Theory

This chapter provides a brief summary of the physical processes involved in fluorescence light generation. For a more in depth treatment of the subject matter see for example Lakowicz [41]. A more detailed analysis of planar laser induced fluorescence as a method for species concentration measurements is given in chapter 5.

Fluorescence is a special case of luminescence, which is the emission of light by substances. Luminescence occurs when an electronic state within an atom or molecule decays into a state of lower energy by emitting a photon according to the selection rules of quantum mechanics. Depending on the life-time of the excited state, this process is called fluorescence or phosphorescence. Usually, the excited state is created by the absorption of a photon. This process is called chemiluminescence if the electron was moved to the excited state as a result of a chemical reaction.

After excitation by the laser, various processes are open to the excited molecule. A common way to illustrate the processes involved during the timespan between absorption and emission of light by a molecule, is the so called Jablonski diagram. Figure 3.1 shows such a diagram, showing processes of interest for this study.

An electron in the singlet ground state S_0 , which can exist in a variety of vibrational energy levels, can be excited into a higher electronic energy level via absorption of a photon of appropriate wavelength¹ λ . This process is nearly instantaneous: the transition occurs on a time scale of about 10^{-15} s.

3.1 Stokes Shift

Depending on the wavelength of the absorbed photon, the molecule is usually either lifted into the first or second excited singlet state, S_1 or S_2 , respectively. The fastest path of energy loss open to the excited molecule is non-radiative internal conversion (IC) to the lowest vibrational level of the S_1 state. IC typically happens within 10^{-10} s. Dipole-dipole interaction with the solvent surrounding the excited molecule can shift the energy level of the excited state downwards. The time scale of this process is typically 10^{-10} s, depending on solvent properties.

¹The energy of a photon of wavelength λ is $E_\lambda = \frac{hc}{\lambda}$. $c = 3 \times 10^8$ m/s is the speed of light and $h = 6.626 \times 10^{-34}$ J s is Planck's constant.

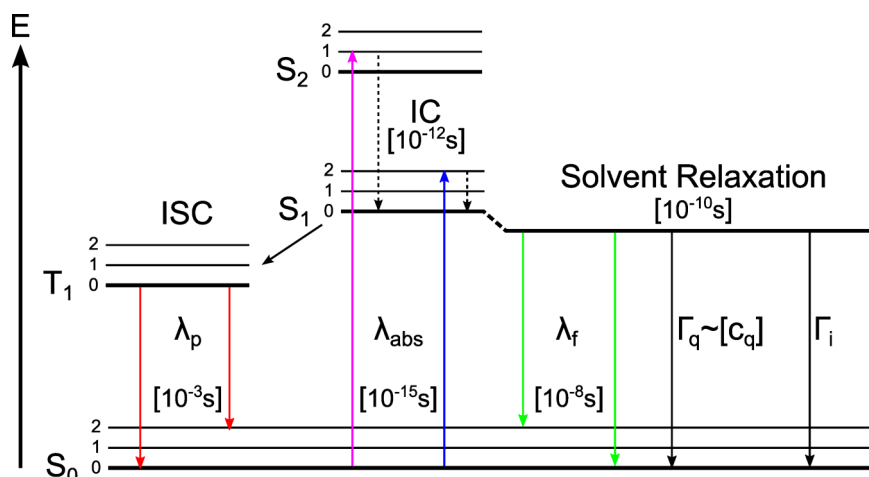


Figure 3.1: Example Jablonski diagram depicting various processes involved in the generation of fluorescent light. Light of sufficiently short wavelength (λ_{abs}) lifts an electron to a higher electric state S_1 or S_2 , whereas internal conversion (IC) quickly shifts the electron down to the lowest vibrational state of the S_1 energy level. The energy can be further dissipated by interaction with the solvent and by intersystem crossing (ISC) into an excited triplet state T_1 . The emission of fluorescent light λ_f is in direct competition to non-radiative paths to the ground state Γ_i , especially Γ_q , collisional quenching. The triplet state can emit phosphorescent light λ_p to get into the lowest energy level.

All aforementioned processes are complete before the typical life-time of fluorescence is reached, which is in the order of 1-10 ns. The energy of the emitted photons depends on the lowest vibrational level of the S_1 state, which is shifted towards an even lower level when observing the fluorescence of a tracer in a solvent. Water has a strong dipole moment and can shift the energy of the S_1 state significantly.

The result of these effects is a shift of the emitted light towards longer wavelength, a so called red shift. This phenomenon is named 'Stokes Shift' after its discoverer Sir G. G. Stokes.

3.2 Phosphorescence

An electron in an excited S_1 singlet state can convert into the first excited triplet state T_1 by a process called intersystem crossing (ISC). It can reach the ground state via another ISC process by phosphorescence. As the $T_1 \rightarrow S_0$ conversion is a so called forbidden transition, this process is very slow. This results in the significantly longer life-time of the phosphorescence when compared to that of the fluorescence in the order of milliseconds. The energy level of the T_1 state is below that of the S_1 state. The wavelength of the emitted phosphorescence light is shifted to an even longer wavelength.

The actual efficiency of the $S_1 \rightarrow T_1$ process is dependent on the molecular structure of the observed tracer. In general, the presence of heavy ions (bromine, iodine) tends to create phosphorescent molecules [41].

3.3 Fluorescence Quantum Yield and Life-Time

The most important characteristics of a fluorescent tracer used in a LIF experiment are the fluorescence quantum yield η_f and the fluorescence life-time τ_f . The quantum yield is defined as the ratio of the number of photons absorbed by the tracer and the number of photons emitted via fluorescence.

$$\eta_f = \frac{\Gamma_f}{\Gamma_{\text{abs}}} = \frac{\Gamma_f}{\Gamma_f + \Gamma_{\text{nr}}} \leq 1 \quad (3.1)$$

Γ_{abs} is the rate of photons absorbed per second and Γ_f is the rate of photons emitted by fluorescence. Γ_{nr} is the sum of all non radiative decay rates transferring the electrons from the excited S_1 state into the ground state. If there were no other decay channels than the emittance of fluorescence photons, η_f could reach a value of 1. It can actually reach values close to 1 for highly efficient tracers.

The fluorescence life-time is defined as the time the tracer molecule spends in an excited state before returning to the ground state.

$$\tau_f = \frac{1}{\Gamma_f + \Gamma_{\text{nr}}} \quad (3.2)$$

Applied to a LIF setup, the quantum yield η_f is needed to estimate the signal rating SR (see 5.4) while the fluorescence life-time τ_f is needed to estimate the saturation excitation (see 5.3).

3.4 Quenching

If other molecules besides the observed tracer are present, they can interact with it and change the efficiency of the fluorescence. This process is called quenching. One distinguishes static and dynamic quenching. In the case of static quenching, the tracer forms a non-fluorescent complex with the quencher. In general, the absorption characteristics of this new complex differ from those of the tracer itself. LIF experiments based on the pH indicator method [21, 46] exploit this to visualize acidic compounds.

Dynamic quenching occurs when an excited tracer molecule is transferred into the ground state upon contact with another molecule (called quencher). On a molecular

level, there are several distinguishable mechanisms of dynamic quenching: The most important process is the Förster resonance energy transfer (FRET). It is based on a dipole-dipole interaction between the excited tracer and the quencher, transferring the quencher into an excited state and relaxing the tracer. This process is proportional to the overlap of the quencher absorption spectrum and the tracer emission spectrum. Other possible quenching processes are electron transfer from the tracer to the quencher and the spatial overlap of the tracer and quencher orbitals.

The exact mechanisms and efficiency of these differ for every tracer-quencher pair. They all have in common that the reduction in fluorescence light intensity I , which is proportional to Γ_f , is dependent on the quencher concentration. This is described by the Stern-Volmer equation:

$$\frac{I}{I_0} = \frac{1}{1 + k_q \tau_f c_q} = \frac{1}{1 + K_{SV} c_q} \quad (3.3)$$

k_q is the bimolecular quenching constant equal to the rate of the quenching process Γ_q per quencher concentration c_q ($\Gamma_q = k_q c_q$). K_{SV} is the Stern-Volmer quenching constant of the specific tracer-quencher pair. This effect has been used in LIF experiments to visualize the transfer of oxygen by using a tracer sensible to oxygen presence [21, 74].

Specific knowledge of the effect of quenching on a specific tracer can be an important parameter if the concentration of the quencher changes throughout the measurement either intentionally (as mentioned above) or by accident. If the concentration of the quencher is constant though, it only influences the experiments by reducing the overall fluorescence yield in an unspecific, yet always negative way. As the quenching constant K_{SV} is directly proportional to the life-time of the excited state, it is much higher for phosphorescence, significantly reducing the possible negative influence of simultaneous phosphorescence measurements.

4 Absorption Spectroscopy

The number of photons originating in the excitation light source (the laser) is proportional to the number of fluorescence photons emitted by the chosen tracer substance via the factor η , the fluorescence quantum yield. Calibrating the signal intensity measured by the camera observing the laser induced fluorescence is a difficult task if no reference value is available. Knowledge of the chosen substances' absorption spectrum helps to decide which tracers to use, while measuring the absorbance in the bulk area of the wind-wave tank during the LIF experiments provides the much needed calibration.

The basic principles of absorption spectroscopy, as applied in this study, are explained below. More complex methods can be used to improve the current implementation by reworking of data analysis methods to use fitted prerecorded spectra¹ and by adding a cavity setup similar to what has been done by Gliß [23] to compensate for the very short absorption path available in the wind-wave tank.

4.1 Lambert-Beer Law

When electromagnetic radiation of intensity I_0 crosses matter of a thickness d , the *Lambert Law* describes the relation of the incident radiation, the thickness and the absorbed radiation ΔI .

$$\frac{dI}{dx} = -k(\lambda, x) I_0 \quad (4.1)$$

The constant of proportionality k is called the absorption constant and is dependent on the wavelength λ of the incident light and can change within the medium. Its dimension is a reciprocal length. By integration of equation (4.1), the intensity decrease across a distance 0 to x can be calculated:

$$I(x) = I(0) e^{-\int_0^x k(\lambda, x') dx'} \quad (4.2)$$

If the medium is homogeneous, k is not dependent on x and equation (4.2) becomes:

¹By using Differential Optical Absorption Spectroscopy, or DOAS, as has been previously implemented for wind-wave tank experiments by Degreif [16]. This method is more robust in long-term measurements as the effects of an unstable or drifting light source are corrected for.

$$I(x) = I(0) e^{-k(\lambda) x} \quad (4.3)$$

Light passing through a medium of homogeneous absorption constant k is reduced to $1/e$ after traveling a distance of $1/k$. A peculiarity of the *Lambert Law* is its common formulation based on the decadic logarithm instead of the natural logarithm:

$$-\ln \frac{I(x)}{I(0)} = k(\lambda) x \quad (4.4)$$

$$-\log_{10} \frac{I(x)}{I(0)} = \ln(10) k(\lambda) x \quad (4.5)$$

$k(\lambda)$ can be calculated by *Beer's Law*, that states

$$k(\lambda) = \epsilon_e(\lambda) c \quad (4.6)$$

$\epsilon_e(\lambda)$ is the molar extinction coefficient in L mol/cm and c is the concentration of the absorbing substance in mol/L . By combining equations (4.5) and (4.6) and integrating the conversion factor $\ln(10)$ into the extinction coefficient, which is now defined for the base of 10, the *Lambert-Beer Law* reads:

$$A = -\log_{10} \frac{I(x)}{I(0)} = \epsilon(\lambda) c x \quad (4.7)$$

where $\epsilon(\lambda)$ is the decadic molar extinction coefficient in L mol/cm and A is the dimensionless absorbance, commonly abbreviated 'Abs'. If $\epsilon(\lambda)$ for a given wavelength is known for a tracer of interest, its concentration can be measured using a relatively simple spectroscopy setup with a fixed optical length x by measuring the intensity $I(0)$ without a tracer substance and monitoring the intensity at any given time during the measurement. For practical applications, several sources of error have to be considered, though: the dark current of the sensor measuring the concentration, the stability of the light source providing the incident light and cross-correlations between the spectra of the tracer substances if more than one is used. A more in depth discussion of these effects and solutions can be found in Degreif [16] and W. Gottwald [70]. The comparatively simple problem of observing a single tracer injected into a wind-wave tank that would otherwise be free of absorbers can be solved using this simple approach.

4.1.1 Absorption Cross Section

When observing the laser induced fluorescence in chapter 5, it will generally be favorable to use the absorption cross section $\sigma(\lambda)$ in $1/\text{cm}$ for calculations. This reflects the common parameter used in many treatises about this subject. In general, it can be said that, while there certainly are studies using the molar extinction coefficient $\epsilon_e(\lambda)$ to the base e , none have been found using the decadic molar extinction coefficient $\epsilon(\lambda)$. On the other hand, most of the chemical literature playing an integral part in this research uses the formulation of the *Lambert-Beer Law* and definition of A to the base 10.

As $\sigma(\lambda)$ and $\epsilon(\lambda)$ describe essentially the same physical process, they can be easily converted into each other. The differences are that $\sigma(\lambda)$ is defined per absorber instead of per mole, for an exponential decay to the base e and for an area of cm^2 instead of L/cm . The formula of the conversion is:

$$\begin{aligned} \sigma(\lambda) &= \underbrace{1000}_{1/\text{cm} \rightarrow \text{cm}^2} \overbrace{\ln(10)}^{10^x \rightarrow e^x} \underbrace{N_A^{-1}}_{\frac{1}{\text{mol}} \rightarrow 1} \epsilon(\lambda) \\ &\approx 3.82 \times 10^{-21} \epsilon(\lambda) \end{aligned} \quad (4.8)$$

4.2 UV/Vis Spectra and the Molecular Structure

When electromagnetic radiation interacts with a molecule, it is able to transfer energy to and put the molecule into an excited state. The relatively high energies present in visible and ultraviolet light are sufficient to excite valence electrons of a molecule. A simple theory describing the excitation of electronic states within a molecule is the HOMO-LUMO theory. Instead of considering all possible electronic transitions, the focus is on two important orbitals: the *highest order occupied molecular orbital* (HOMO) and the *lowest order unoccupied molecular orbital* (LUMO). As the transition between these two orbitals requires the lowest energy of all electronic transitions, it is also the most probable. The spectrum of a molecule is dominated by the HOMO-LUMO transition.

There are three types of electron orbitals in a molecule. The σ -electrons participate in single bonds of two atoms. These electronic states have comparatively high excitation energies, i.e. they occupy a state of low energy within the molecule. The π -electron orbitals originate in double bonds between atoms of the molecule and have lower excitation energies than the σ -electrons but higher excitation energies than the n -electrons, that do not participate in molecular bonds. The orbital energies E are sorted in the following way:

$$E_{\sigma} < E_{\pi} < E_n < E_{\sigma^*} < E_{\pi^*} \quad (4.9)$$

Where E_{σ^*} and E_{π^*} are the excited σ and π states. An excited n state cannot exist since this would be a free electron. It is possible to excite a n -electron into an excited σ or π orbital, resulting in the following possible transitions:

$$\begin{aligned} \sigma &\rightarrow \sigma^* \\ \pi &\rightarrow \pi^* \\ n &\rightarrow \sigma^* \\ n &\rightarrow \pi^* \end{aligned}$$

The $\sigma \rightarrow \sigma^*$ transition usually needs the highest energy to excite, the $n \rightarrow \pi^*$ transition is usually of the lowest energy. For many molecular substructures, so called chromophores, the HOMO-LUMO transition and the wavelength related to the energy needed for its excitation are well known.

In this work, most experiments were conducted using a laser with a wavelength of 266 nm. To choose substances with a good extinction coefficient at 266nm wavelength, it is important to recognize typical chemical structures that cause absorption within this wavelength regime. Some of these so called chromophores are listed in table 4.1. When multiple chromophores are combined into a single molecule, the absorption wavelength can be considerably higher. When the chromophores are present in conjugated systems, the energy of the HOMO-LUMO transition can be significantly lower. A conjugated system is a molecule with alternating single and double bonds.

A prominent example of a conjugated system is the aromatic ring structure of benzene. Benzene's molecular formula is C_6H_6 . The six carbon atoms form a cyclic structure with alternating double and single bonds. The double bonds have no preferred position

Chromophor	Transistion	Wavelength [nm]
-C=C-	$\pi \rightarrow \pi^*$	190 nm
=C=O	$\pi \rightarrow \pi^*$	180 nm
	$n \rightarrow \pi^*$	280 nm
-O-	$n \rightarrow \sigma^*$	180 nm
-I	$n \rightarrow \pi^*$	250 nm
-S-	$n \rightarrow \sigma^*$	235 nm

Table 4.1: Some chromophores of interest for this study. (Source: W. Gottwald [70])

and the resulting absorbance of this system that is essentially three conjugated -C=C- systems is very high with, among others, an absorbance peak at 256 nm.

Apart from the chromophores, there are also the so called auxochrome groups. These are essentially atoms or atomar groups that have a n -orbital. When these are bound directly to a chromophore group, they change the absorption characteristic towards a higher wavelength (lower energy) and higher probability (extinction coefficient). Some auxochrome groups are: -OH , -O- , -NH_2 and -NH- .

This knowledge helps to make first decisions when searching for a new tracer substance, but is by no means sufficient. It is merely a first step when sorting through the seemingly endless catalog of substances available.

Part II

Experimental Methods

5 Applied Planar Laser Induced Fluorescence

Laser-induced fluorescence (LIF) is a well established experimental technique used in various applications. Initial experiments were conducted in the fields of spectroscopy and chemical analysis using single-point detectors [39]. Results of these early experiments could be transferred to one- and two dimensional detectors with relative ease. Nowadays, LIF techniques are used in the analysis of liquid and gaseous flows, having the potential to monitor parameters as diverse as species concentration, mixture mole fractions, density, temperature, velocity and pressure.

A typical LIF experiment comprises a molecular tracer within a substance or flow field, a laser tuned to excite a particular transition of this tracer and a photo detector aligned to the emitted light. The incident laser light shifts some of the tracer molecules into a higher energy state. One of the processes open to these excited molecules is radiative decay. They lose their excess energy by emitting a photon. This is called fluorescence. A photo detector like a CCD camera, combined with appropriate filters, is used to detect the generated fluorescence light.

Planar laser induced fluorescence (PLIF) is a well established and as such well documented technique in fluid research. In PLIF, a flow is illuminated by a laser, that is widened to form a two dimensional sheet. Fluorescence is either stimulated in particles of the flow itself (i.e. SO_2 in combustion processes) or in tracers that are mixed into the flow. Van Cruyningen, Lozano and Hanson [66] provide a description of the application of PLIF in gaseous flows, specifically for its application in combustion processes, Crimaldi [12] examines the technique thoroughly for its use in aqueous flows.

The following sections provide the application of PLIF as described in the sources above to the measurements provided within this work, and are not intended to be an exhaustive treatise of the general subject matter.

5.1 Effective Fluorescence Quantum Yield

The following considerations assume that the quencher concentration c_q is constant during the measurement. The influence of quenching will be accounted for in the effective fluorescence quantum yield η_{eff} and is no longer explicitly considered. η_{eff}

replaces the actual fluorescence quantum yield η_f for the following considerations. When comparing measurement results with theoretically calculated values, the possibility of significant intensity loss due to quenching must be considered.

$$\begin{aligned}
 K_{SV} c_q &= \text{const.} \\
 \Rightarrow \eta_{\text{eff}} &= \frac{\Gamma_f}{\Gamma_f + \Gamma_{\text{nr}} + K_{SV} c_q} = \text{const.}
 \end{aligned}
 \tag{5.1}$$

The rates of fluorescence photon emission Γ_f , quenching $K_{SV} c_q$, and of other excitation deactivation processes Γ_{nr} are closer examined in chapter 4. The most likely quencher in wind-wave tank measurements is oxygen. Since all measurements were conducted in an equilibrated state of oxygen concentration in the air and water, the assumption stated above is feasible.

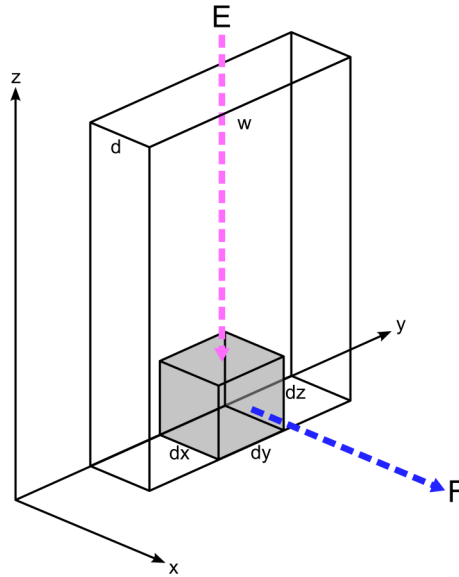


Figure 5.1: The volume $dV = dx \times dy \times dz$ is illuminated by a laser sheet of width w and depth d with an irradiance E . The detector observes the fluorescence F passing through an area $dA = dy \times dz$.

5.2 Concentration Measurements

Assuming there is a laser irradiance E in $\text{photons}/\text{s}\cdot\text{m}^2$ and a path of length dz (see figure 5.1), the number of absorbed photons is equal to the attenuation dE of the incident irradiance. It can be calculated using the absorption cross section σ_λ for the incident

light's wavelength λ and the particle density of tracer molecules ρ_{tr} in the observed volume. A constant tracer concentration is assumed in the bulk of the gaseous phase, which is used for the tracer efficiency comparisons.

$$dE = -E \sigma_\lambda \rho_{tr} dz \quad [\text{photons/s m}^2] \quad (5.2)$$

The number F of fluorescence photons emitted per second by a volume of height dz and area $dx \times dy$, that has been irradiated by the laser, is equal to the number of photons absorbed within the volume times the fluorescence quantum yield η_{eff} :

$$d^3F = -\eta_{\text{eff}} dE dx dy \quad [\text{photons/s}] \quad (5.3)$$

Combining equations (5.2) and (5.3) the number of fluorescence photons emitted is equal to:

$$d^3F = \eta_{\text{eff}} E(z) \sigma_\lambda \rho_{tr} dx dy dz \quad [\text{photons/s}] \quad (5.4)$$

With η_{eff} (see 5.1) and σ_λ being constant properties of the fluorescent tracer, the concentration ρ_{tr} can be directly calculated from the observed fluorescence signal F if the incident laser irradiance $E(z)$ is known.

5.3 Saturation Excitation

Equation 5.4 is based on the assumption that the observed fluorescence F is proportional to the amount of photons absorbed per time from the incident laser irradiance E . This assumption is valid only if the excitation irradiance of the laser beam is well below the saturation irradiance, which is a tracer property.

This is called 'linear fluorescence regime' and is presumed in most PLIF experiments. The general relation of the fluorescence F to the incident irradiance E , which can be derived from the rate equations [26], is:

$$F \sim \frac{E}{1 + \frac{E}{E_{\text{sat}}}} \rho_{tr} \quad (5.5)$$

E_{sat} is the saturation irradiance, which is a tracer dependent value. Saturation occurs when the rate of excitation surpasses the rate of excitation deactivation. A common model to calculate E_{sat} [66] is:

$$E_{\text{sat}}(\lambda) = \frac{1}{\tau_f \sigma(\lambda)} \quad [\text{photons/s m}^2] \quad (5.6)$$

where $\sigma(\lambda)$ is the absorption cross section at the excitation wavelength λ and τ_f is the life-time of the fluorescence. If the irradiance of the laser sheet is far below E_{sat} , the excitation is called *weak* and the fluorescence F is proportional to the laser irradiance:

$$F \sim E \rho_{\text{tr}} \quad (5.7)$$

This is the usual assumption and also the assumption made for the calculations within this section. There are other cases to consider though. If E is much higher than E_{sat} , the fluorescence is no longer dependent on the irradiance and becomes directly proportional to the concentration ρ_f of the tracer. This excitation is called *strong*:

$$F \sim \rho_{\text{tr}} \quad (5.8)$$

Planning an experiment in the intermediate excitation region should be avoided, since the nonlinear dependence of F and E unnecessarily complicate the problem.

5.3.1 Calculating the Laser Irradiance

The calculation of the laser irradiance is relatively straight forward. If a pulsed system is used, it has to be distinguished between the average irradiance E_{avg} and the peak irradiance E_{peak} . While E_{avg} would nearly always result in weak excitation, pulsed systems can have extremely high peak irradiances that can result in strong or intermediate excitation. For a laser system of given wavelength λ in nm and output power P_{out} in W/s, the number of photons emitted per second Φ_{avg} can be calculated by:

$$\Phi_{\text{avg}} = \frac{P_{\text{out}} \lambda}{h c} \quad (5.9)$$

with the speed of light c and Planck's constant h . For a pulsed system it is important to calculate the flux per pulse:

$$\Phi_{\text{peak}} = \frac{P_{\text{out}} \lambda}{h c f_p \tau_p} \quad (5.10)$$

with the number of pulses per second f_p and the pulse length in seconds τ_p . The irradiance is defined as the flux per area. This results in the following equation for the laser irradiance in dependence of the laser sheet area A :

$$E_{\text{avg}} = \frac{\Phi_{\text{avg}}}{A} = \frac{P_{\text{out}} \lambda}{h c A} \quad (5.11)$$

$$E_{\text{peak}} = \frac{\Phi_{\text{peak}}}{A} = \frac{P_{\text{out}} \lambda}{h c f_p \tau_p A} \quad (5.12)$$

5.3.2 Optical Thickness

Integration of (5.2) gives the following equation for the attenuation of the laser beam within the medium:

$$E(x) = E(x_0) \exp \left[-\sigma_\lambda \int_{x_0}^x \rho_{tr}(x) dx \right] \quad [\text{photons/s m}^2] \quad (5.13)$$

Provided that the concentration along the beam path is constant, the attenuation becomes:

$$E(x) = E(x_0) e^{-\sigma_\lambda \rho_{tr} \Delta x} \quad [\text{photons/s m}^2] \quad (5.14)$$

$E(x)$ can be considered a constant if the exponent is much smaller than one. The maximum distance Δx for which this relation holds true is the optical thickness of the medium.

$$\sigma_\lambda \rho_{tr} \Delta x \ll 1 \quad (5.15)$$

If the measurement is done in an optically thin medium, accurate PLIF measurements can be conducted regardless of the excitation irradiance calculated and discussed in section 5.3. Without any change in E , all considerations concerning the relation of F and E become moot [12].

For this reason, all measurements taking in the course of this study were conducted using tracer concentrations that ensure an optically thin medium as the fluorescence life-time of some tracers was not known.

5.4 Signal Rating

To compare the sensitivity of different tracers, a new parameter is introduced: the signal rating SR that depends upon several tracer characteristics. It is obvious that the expected brightness of a fluorescence signal depends on η_{eff} , the tracer's fluorescence quantum efficiency, on σ_λ , the tracer's absorbance at the excitation wavelength λ , and on the tracer concentration ρ_{tr} , which can be limited both by the tracers vapor pressure and the desire to measure in an optically thin medium.

To motivate the signal rating SR , the radiance L of the fluorescent light sheet is calculated. L is the number of fluorescence photons F emitted per second, per square area $dA = dy dz$ illuminated by the laser sheet and per solid angle Ω between the area dA and an observer.

$$L = \frac{d^2 F}{dA d\Omega} \quad [\text{photons/s m}^2 \text{ sr}] \quad (5.16)$$

5.4.1 Calculating the Signal Rating

Assuming operation in an optical thin medium, $E(z)$ can be assumed to be constant (see section 5.3.2). The camera only sees a projection of the fluorescence generated in the volume dV . Assuming a homogeneous fluorescent sheet parallel to the camera detector plane with thickness d , integration in camera viewing direction dx of equation (5.4) gives:

$$d^2 F = \eta_{\text{eff}} E \sigma_\lambda \rho_{tr} d dy dz \quad [\text{photons/s}] \quad (5.17)$$

The observed area dA was defined as $dy dz$. With equation (5.16), the result becomes:

$$L = \frac{\eta_{\text{eff}} E \sigma_\lambda \rho_{tr} d}{d\Omega} \quad [\text{photons/s m}^2 \text{ sr}] \quad (5.18)$$

Since fluorescence is an isotropic process, the photons can be assumed to be distributed evenly across a sphere. The solid angle of a sphere is 4π , which results in the following equation for the radiance:

$$L = \frac{1}{4\pi} \eta_{\text{eff}} E \sigma_\lambda \rho_{tr} d \quad [\text{photons/s m}^2 \text{ sr}] \quad (5.19)$$

Using equation (5.9), the irradiance E of a laser sheet is:

$$E = \frac{\Phi}{dw} \quad [\text{photons/s m}^2] \quad (5.20)$$

where d is the thickness of the laser sheet in viewing direction dx of the camera and w is the width of the laser sheet (in y direction). For a LIF setup, L does not depend on the laser sheet thickness but on its width:

$$L = \frac{1}{4\pi} \eta_{\text{eff}} \sigma_\lambda \rho_{tr} \frac{\Phi}{w} \quad [\text{photons/s m}^2 \text{ sr}] \quad (5.21)$$

This is reasonable as the camera integrates over d while a wider laser sheet has a lower irradiance. In equation (5.21), only three parameters of L depend on the used tracer - η_{eff} , σ_λ and ρ_{tr} - while the rest of the equation depends on the laser sheet and the solid angle covered by the imaging system. This leads to the following definition of SR :

$$SR = \eta_{\text{eff}} \sigma_\lambda \rho_{tr} \quad [1/\text{m}] \quad (5.22)$$

5.4.2 Measuring the Signal Rating

The signal rating SR cannot be measured directly. Instead, the camera can measure the radiance L . Combining equations (5.21) and (5.22), the radiance L can be written as:

$$L = \frac{1}{4\pi} \frac{\Phi}{w} SR \quad [\text{photons}/\text{s m}^2 \text{ sr}] \quad (5.23)$$

In order to measure the radiance, the conversion factor $R(\lambda)$ of the employed camera's digital gray value μ to the number of photons arriving at a single pixel of the sensor needs to be known. R is equal to the sensor's quantum efficiency $\eta_{\text{cam}}(\lambda)$ times the gain of the camera electronics K .

$$F = \frac{\mu}{R(\lambda)} = \frac{\mu}{\eta_{\text{cam}}(\lambda) K} \quad [\text{photons}/\text{s}] \quad (5.24)$$

The dark current of the sensor has to be taken care of, either as an offset in the formula or by subtracting the dark signal before employing the conversion. Otherwise, the number of photons would be overestimated.

L is defined per area and solid angle. The number of photons detected at a single pixel is converted, using the pixel area A_{pix} and the camera optics solid angle Ω_{cam} .

$$L = \frac{\mu}{R(\lambda) A_{\text{pix}} \Omega_{\text{cam}}} \quad [\text{photons}/\text{s m}^2 \text{ sr}] \quad (5.25)$$

To calculate precise values of L , the transmission characteristics of the optical path between the sensor and the fluorescent light sheet need to be known and corrected for. The total transmission efficiency $T_{\text{total}}(\lambda)$ is the product of the transmission of all elements within the optical path between the light sheet and the camera sensor. Typically, these are the transmission efficiency of the used camera lens $T_{\text{lens}}(\lambda)$, the transmission of the wind-wave tanks window $T_{\text{tank}}(\lambda)$ and of any additional filters employed $T_{\text{filter}}(\lambda)$.

$$T_{\text{total}}(\lambda) = T_{\text{tank}}(\lambda) T_{\text{lens}}(\lambda) T_{\text{filter}}(\lambda) \quad (5.26)$$

$$L = \frac{\mu}{R(\lambda) A_{\text{pix}} \Omega_{\text{cam}} T_{\text{total}}(\lambda)} \quad [\text{photons/s m}^2 \text{ sr}] \quad (5.27)$$

All of these values are dependent on the wavelength λ of the signal. By combining equations (5.23) and (5.27), the signal rating can be derived from the measurement results:

$$SR = \frac{4\pi w}{\Phi} \frac{\mu}{R(\lambda) A_{\text{pix}} \Omega_{\text{cam}} T_{\text{total}}(\lambda)} \quad [1/\text{m}] \quad (5.28)$$

Knowledge of the fluorescence spectrum is necessary for accurate calculations. Often, the actual wavelength dependence of one or more of these characteristics is not known. Equation (5.28) can still be used to estimate SR to get a quantitative assessment of the employed LIF system.

5.5 Resolution

In general, the resolution of a PLIF setup depends upon the volume that is imaged by a single pixel of the imaging system. If the volume a single pixel sees is equal to the shaded volume dV in figure 5.1, the resolution in y and z direction is dependent on the imaging system's resolution while the resolution in the z direction depends on the sheet thickness d .

In this study, only the resolution in z direction was of any interest, which simplifies the problem considerably. In theory, the laser sheet thickness d should have no effect on the z resolution. To avoid obfuscation of the concentration characteristics close to the surface the camera is mounted at an angle α . The consequence is that the measured concentration is effectively integrated over a sloped volume within the laser sheet, reintroducing a d dependence to the resolution. Figure 5.2 shows the relation.

The laser sheet width d limits the maximal proximity Δm to the water surface, where only air sided fluorescence signals can be measured. As can be seen in figure 9.2, any signals imaged by a pixel at least partially in between a and b is actually integrated over both water- and air-sided signals. The height between a and b is equal to the sheet width d times the tangents of the camera angle α .

$$\Delta m = d \tan \alpha \quad (5.29)$$

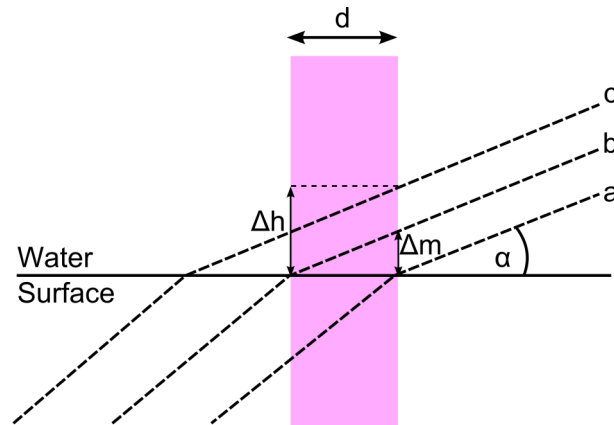


Figure 5.2: Effect of the camera slope α on the vertical resolution of the acquired image. The concentration imaged by a pixel between a and b is dominated by water sided fluorescence. Pixel between b and c image a concentration averaged over the height Δh .

If b is the lower limit of a pixels projection and c is the upper limit, then Δh is the height that defines the volume the monitored concentration was integrated over. It is equal to the height resolution of a single pixel plus Δm .

Water-side Resolution The fluorescence signal is proportional to the concentration which is often higher at the water side of the interface (see section 2.3.4). To estimate if a single image acquisition system can be used to acquire both air- and water-side concentration profiles, the highest possible vertical resolution in the water was estimated. All considerations made above remain valid, but the angle of the camera changes due to refraction at the water surface. This is shown in figure 5.3.

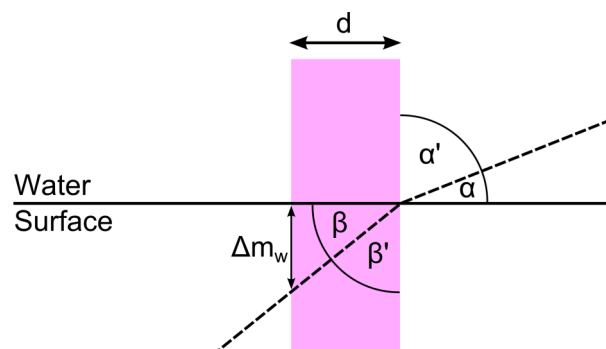


Figure 5.3: Effect of the camera slope α on the vertical resolution of fluorescence profiles originating in the water-side.

According to Snell's law, the ratio between the angle of incidence α' and the angle of refraction β' is:

$$\frac{\sin \alpha'}{\sin \beta'} = \frac{\cos \alpha}{\cos \beta} = \frac{n_w}{n_a} = n_w \quad \text{with} \quad n_a = 1 \quad (5.30)$$

n_a and n_w is the refractive index in air and water, respectively. The angle β is:

$$\beta = \arccos \left(\frac{\cos \alpha}{n_w} \right) \quad (5.31)$$

For the calculation of the maximum proximity to the water surface Δm_w where an undisturbed water-sided fluorescence signal can be measured, β replaces α in equation (5.29):

$$\Delta m_w = d \tan \beta = d \tan \left(\arccos \left(\frac{\cos \alpha}{n_w} \right) \right) \quad (5.32)$$

This function has a minimum at $\alpha = 0$. With the refractive index of water $n_w = 1.33$, the correlation between Δm_w and the laser sheet thickness d for the water-side becomes:

$$\Delta m_w = 0.88 d \quad (5.33)$$

As shown in (5.33) the maximum possible resolution in the water-side is approximately 90% of the laser sheet thickness d . Typical water-sided boundary layer thicknesses are 250 μm and below (see section 2.3). To measure water-sided concentration profiles using a single camera mounted above the water surface the laser sheet cannot be thicker than $\approx 25 \mu\text{m}$. The currently employed laser system and optics do not allow for a sheet this thin (see section 6.2).

6 Setup

A series of experimental setups were constructed during the course of this work with the goal to test as many of the tracer substances described in chapter 8 as possible. The following chapter focuses on these setups in detail.

As there was neither a suitable laser system nor a wind-wave tank available, first measurements were conducted using a simpler test setup. This test setup was able to simultaneously measure the laser induced fluorescence (LIF) signal strength as well as the absorption cross-section of a given tracer at high concentration and low laser intensity. As a result of these measurements, it was possible to estimate the necessary power output of a laser needed for actual wind-wave tank experiments.

The next step was to perform several tests at the Aeolotron wind-wave tank, using a new laser system which was acquired as a result of the preliminary measurements. Experiments at this facility proved to be cumbersome and time-consuming. While a number of important facts about the difficulties of air-sided profile measurements were learned, the measurements themselves were mostly without success. Experience gathered with through experiments helped to get a better understanding of the conditions necessary for a successful visualization of the air-sided gas transfer.

Using the previously obtained information, a new wind-wave-channel was constructed (see appendix A for details). It is a very small facility, allowing easy optical access and experiments with comparably small amounts of chemical substances: optimal conditions for testing a new setup and finding suitable tracers. The construction of this wind-wave tank took into consideration the problems encountered at the Aeolotron. The LIF setup at this facility enabled quantitative tracer assessment measurements as well as first profile measurements.

6.1 Preliminary Measurement Setup

A preliminary setup was constructed to estimate the necessary laser output and tracer properties for measurements in a wind-wave tank. As the system is very small and air-tight compared to a wind-wave tank and can be cleaned with relative ease, some tracers that were considered too risky in terms of health or contamination issues could still be analyzed. A sketch of the setup is shown in figure 6.1. It was realized upon an

optical table manufactured by Newport. The preliminary setup consists of three main parts: the tracer injection, the LIF setup, and an absorption spectrometer.

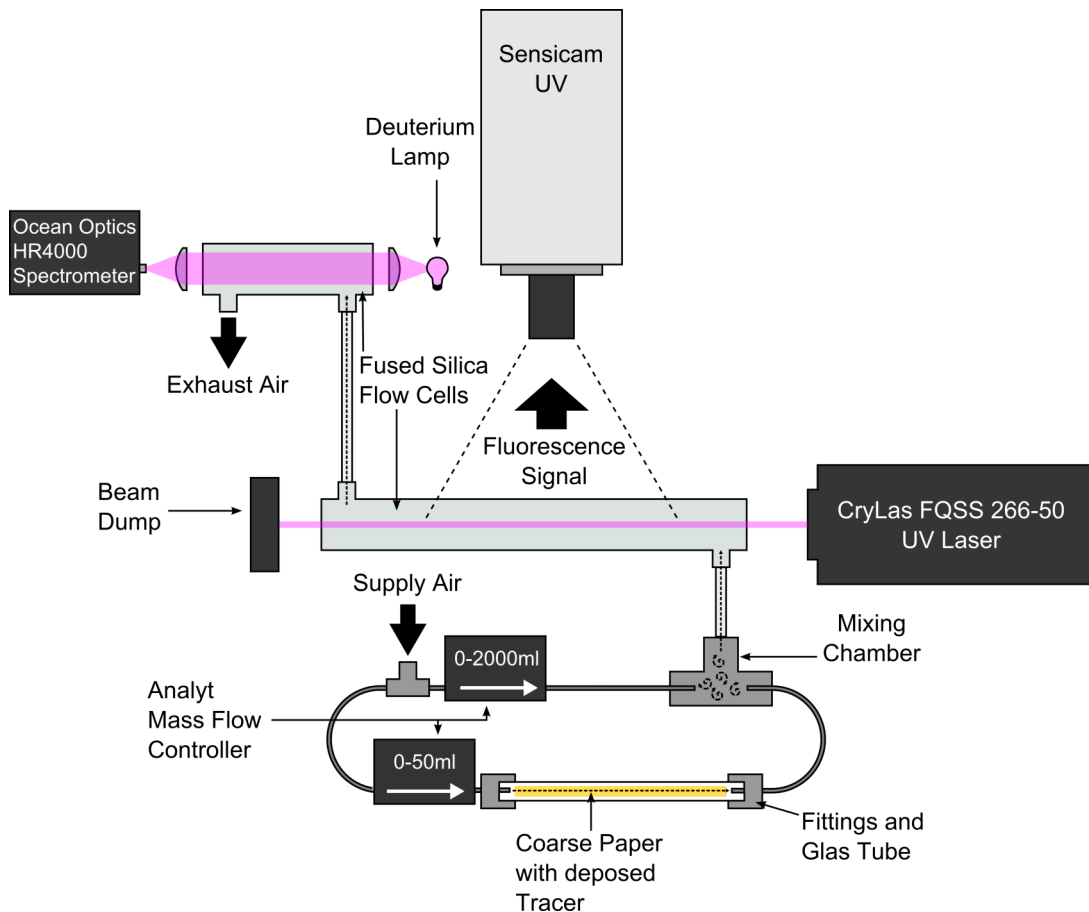


Figure 6.1: Preliminary Measurement Setup An air flow passing above a sheet of coarse paper drenched in tracer substance is mixed with a flow of clean air to create a combined flow of defined tracer concentration. A UV-laser excites fluorescence within the first cuvette, that is recorded by a UV-sensitive camera. The flow passes through a second cuvette, where a spectrometer measures the tracer absorbance.

6.1.1 Tracer Injection

The tracer injection was built to ensure a defined concentration of tracer vapor within the system. Two streams of air - one saturated with tracer vapor the other clean - are combined in a mixing chamber and then injected into the measurement device (see figure 6.1). The stream of saturated vapor is generated within a glass chamber that contains a sheet of coarse paper drenched in tracer substance. Due to the huge surface provided by this paper, the evaporation process is accelerated. The glass chamber has

a length of 25 cm and an inner diameter of 8 mm, resulting in a volume of 12.57 ml. The sheet of coarse paper used for tracer evaporation has a surface area of 25 cm². It is folded before being inserted into the chamber, allowing the air to flow both above and below the paper sheet.

The saturated flow is set to 5 ml/min via the mass flow controllers, resulting in a residence time of 75.4 s for the air within the chamber. Since no evaporation rate measurements were available, it had to be assumed that these parameters were sufficient to ensure a saturated vapor environment. Even if that was not the case for an individual tracer, the spectrometer should be able to provide information about the actual concentration within the system at a given time.

The tubing system and the fittings were produced by Swagelok. The inner diameter of the stainless steel tubing is 1.75 mm. The mixing chamber is a stainless steel T-fitting, which has an inner diameter of 9.5 mm. The flow rate of the two individual streams can be controlled using two mass-flow controllers produced by Analyt-MTC. The clean air flow can be adjusted between 0 ml/min and 2000 ml/min. The flow of saturated tracer vapor can be set between 0 ml/min and 50 ml/min resulting in a vast range of possible concentration ratios. These mass-flow controllers are equipped with an RS-232 interface permitting simple remote controlling via computer.

6.1.2 Fluorescence Measurement

The fluorescence measurement of the preliminary setup is realized with a low powered pulsed UV-laser system and a UV-sensitive camera. The combined air-vapor flow leaving the mixing chamber passes through a 250 mm long and 22 mm wide cylindrical flow cell made of fused silica. This flow cell was custom built at the glass workshop of the Physikalisches Institut Heidelberg.

The beam of a CryLas FQSS 266-50 UV-laser system (figure 6.2) passes the flow cell lengthwise, exciting fluorescence along its way. The laser is a frequency quadrupled Nd:YAG¹ system operating at a frequency of 100 Hz with a pulse energy of 60 μ J and a pulse width of 1 ns. This results in a peak power of 60 kW and an average power of 6 mW. The laser beam is dumped upon a dull black anodized aluminum surface positioned 4 cm behind the cuvette.

The excited fluorescence is monitored using a Sensicam UV manufactured by PCO (figure 6.3) and a Pentax H2520-UVM UV-lens. The UV-quantum efficiency of the CCD-sensor built into the Sensicam UV and the transmission of the lens are shown in figure 6.4. The Sensicam-UV is a 12 bit camera with an integrated electron multiplier that can amplify the signal up to 500 times. It has a resolution of 1004 \times 1002 pixel with an individual pixel size of 8.0 μ m \times 8.0 μ m. The maximum frame rate depends on the

¹neodymium-doped yttrium aluminium garnet



Figure 6.2: CryLas FQSS 266-50 laser head (Source: CryLas FQSS 266-50 datasheet)



Figure 6.3: PCO Sensicam UV camera (Source: PCO Sensicam UV datasheet)

resolution used. At maximum resolution, the camera has a frame rate of 12.9 frames per second. Reducing the vertical resolution to 501 lines, the camera can operate at 25.0 frames per second. Using X95 profiles, the camera was mounted at a distance of 25 cm above the laser beam crossing the flow cell. It was set to a binning of 2×2 pixel with an exposure time of 500 ms. The very long exposure time was necessary for the preliminary measurements due to the low fluorescence intensity caused by the low laser output power.

6.1.3 Spectrometer

To measure the tracer concentration in the setup an absorption spectrometer was integrated. The spectrometric setup contains a 100 mm long and 20 mm wide cylindrical fused silica flow cell manufactured by Agilent. The combined air-vapor flow enters this cell after passing through the fluorescence flow cell. The cell's exit is attached to the exhaust air system of the laboratory. The tracer concentration within the flow cell is measured by UV-absorption spectroscopy. The spectroscopic unit was assembled upon a OWIS SYS 65 System Rail of 100 cm length, using a pair of adjustable lens mounts and custom built mounts for the light source, spectrometer, and flow-cell.

A Heraeus-Noblelight FiberLight UV-Vis lamp (figure 6.5) serves as the setups light source. It contains both a deuterium lamp emitting UV light and a tungsten lamp emitting visible light. A fused-silica lens with a focal length of 25 mm is employed to parallelize the light coming from the lamp. The parallel beam passes through the flow cell and is focused onto the opening slit of the spectrometer, using another lens of the same type. Both lenses have a diameter of 22.4 mm, a broadband anti-reflex coating in the UV range (see appendix B), and were made by Linos/Qioptiq. The spectrometer

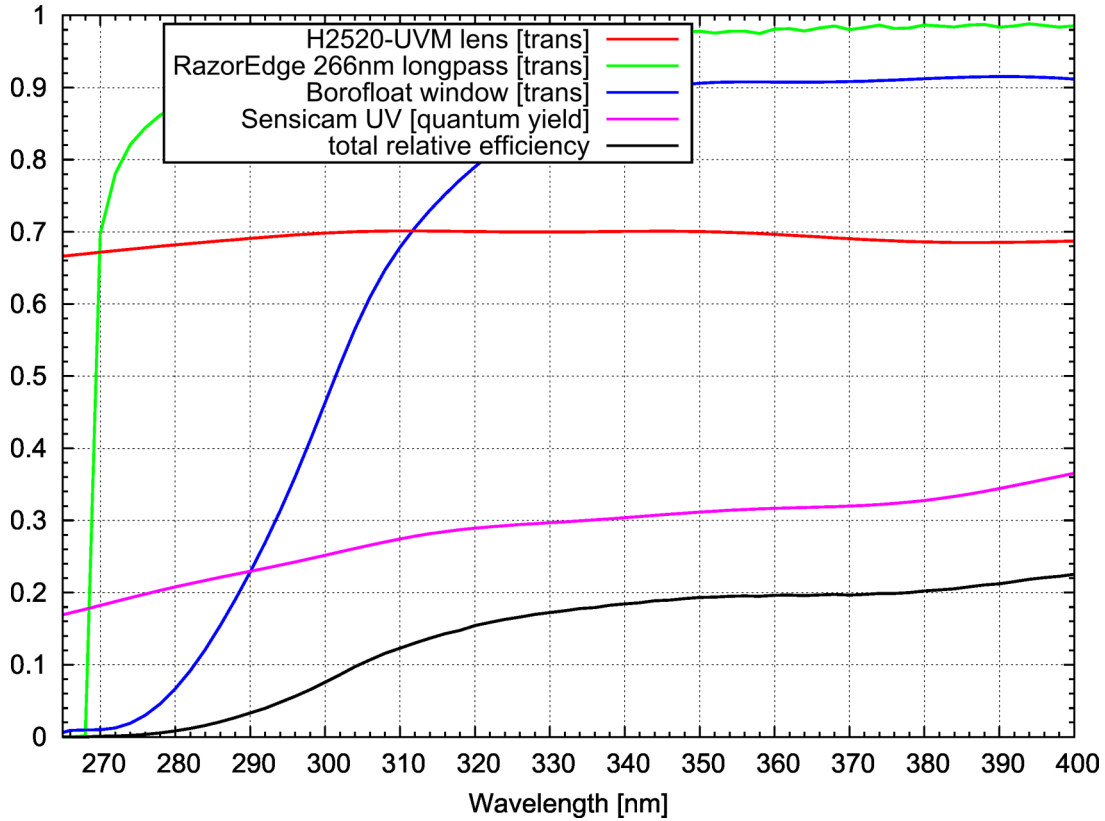


Figure 6.4: UV-Optics Quantum efficiency of the Sensicam UV (purple) and the transmission of the Pentax H2520-UVM UV-lens (red), the Borofloat window of the wind-wave tank (blue) and the Semrock RazorEdge 266 nm longpass filter in front of the camera (green) in dependence of the wavelength of incoming photons. The black line is the relative efficiency of the combined system's photon transport. (Data source: Digitized spectra from vendor data sheets.)

used is an OceanOptics HR4000 (figure 6.6) with a spectroscopic range of 200-305 nm. Light entering the 25 μm opening slit of the HR4000 is focused upon a grating element by a collimating mirror. The diffracted light is focused upon a CCD array with 3658 pixel arranged in a single row. The spectrometer has a wavelength dependent resolution of 0.02-8.4 nm and the pixel are read out by a 14 bit analog-digital converter.

6.2 Wind-Wave Tank Setup

As mentioned before, a new wind-wave tank optimized for visualization techniques was built. At this wind-wave tank, experiments can be set up and conducted with less expenditure of time. For details on the general setup of the facility see appendix A. This section provides an overview of the devices added for air-sided profile measurements.



Figure 6.5: Heraeus Noblelight Fiberlight UV-Vis light source with attached optical fiber (Source: Heraeus Noblelight website)



Figure 6.6: OceanOptics HR4000 spectrometer (Source: OceanOptics website.)

These are mostly non-stationary and not an inherent part of the wind-wave tank. Most of them can be used with relative ease at other facilities.

6.2.1 Cover Plate

A new cover plate for the measurement section of the visualization-test wind-wave tank had to be constructed. This plate allows for UV-laser beam entrance into the wind-wave tank and for measurements of absorption spectra in the air volume of the tank. The cover plate is shown in figure 6.7 from above and side view. Like the other cover plates described in appendix A, it is made of PVC covered with adhesive PTFE foil (Teflon) of 0.1 mm thickness manufactured by Polytera to prevent damage from chemical substances.

The design of the cover plate originates in two specific needs of the planned LIF-measurements. The opening for the UV-laser beams should be large enough to render the simultaneous use of two lasers for comparison measurements possible. An absorption spectrometer must be fitted into the setup to monitor the tracer concentration in the bulk close to the fluorescence generating laser beam.

The price of fused silica windows, which are necessary for the use of UV-lasers rises disproportionately for sizes above a diameter of 50 mm. Two UV-grade fused silica plane plates with a diameter of 50 mm and a thickness of 5 mm by Linos/Qioptic are placed into the cover plate close to each other. This setup provides the desired conditions for measurements with beams originating from two different lasers and for the use of laser sheet widths of up to 40 mm.

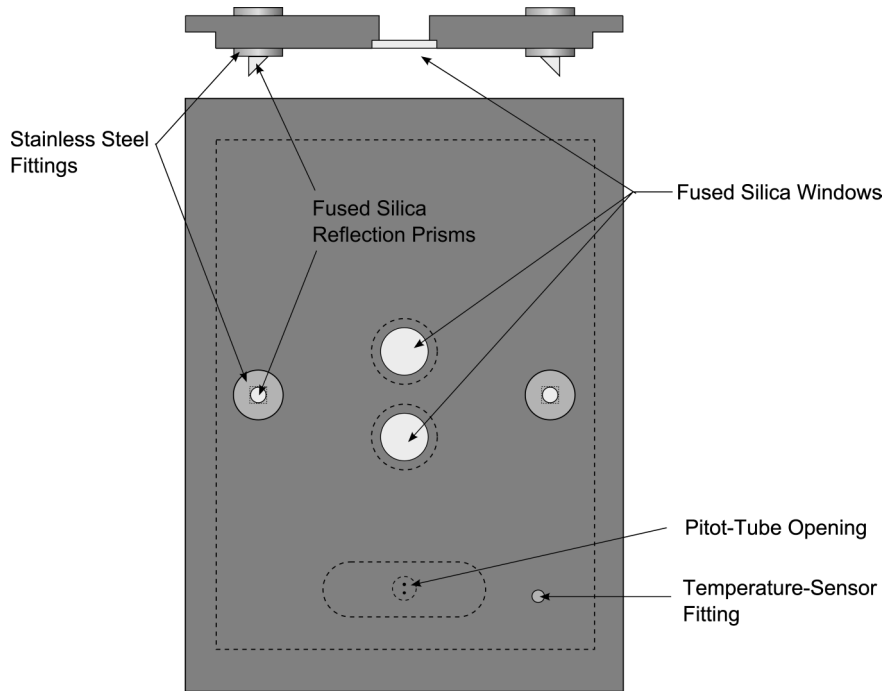


Figure 6.7: UV-LIF Cover Plate The cover plate constructed for UV-LIF measurements at the visualization-test wind-wave tank. The plate's dimensions are $27\text{ cm} \times 40\text{ cm} \times 2.5\text{ cm}$. **Top:** Sectional view of the coverplate. **Bottom:** View from above.

To perform UV-absorption measurements, two stainless steel fittings were designed that can be screwed into the cover plate in between the two openings for the excitation lasers. Into each of the fittings, a $16\text{ mm} \times 16\text{ mm}$ fused silica reflection prism is glued, opening an optical path from one fitting to the other and sealing the fittings. Using an o-ring, the fittings seal the cover plate hermetically. On the upper side of the fittings, a C-mount thread is installed for an easy setup of a spectrometer. In addition, the cover plate contains an opening for a Pitot-tube for wind profile measurements and a compressing fitting for a Greisinger Pt100 air temperature sensor. For further details on the Pitot-tube and the temperature sensor, see appendix A.

6.2.2 Tracer Injection

For experiments with highly soluble tracers, a defined amount of the substance needs to be inserted into the wind-wave tank. To create such a defined amount of air saturated with the tracer gas, the tracer substance is put into a sample bag filled with air. The volatile tracer evaporates, hence filling the bag with a saturated air and tracer mixture. The sample bags of 11, 101 and 301 volume are manufactured by SKC from Tedlar (Polyvinylfluorid), a chemically inert foil that is produced by Dupont.

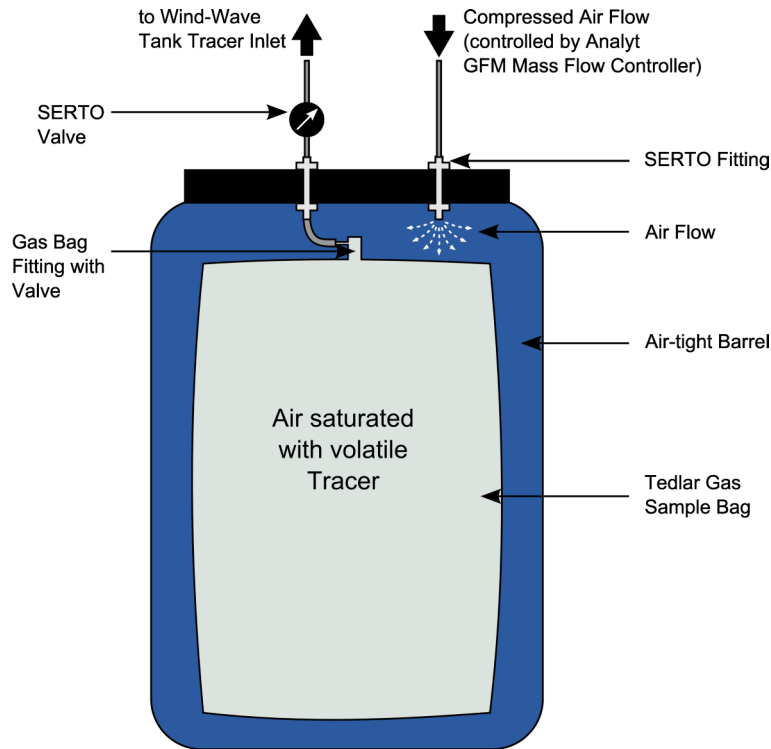


Figure 6.8: A Tedlar bag filled with a saturated air and tracer vapor mixture is put inside an air-tight barrel. The mixture is pressure injected into the wind-wave tank by a controlled air flow into the barrel.

To inject the tracer vapor air mixture into the wind-wave tank, the bag is put inside a 301 air-tight barrel. This barrel is equipped with two SERTO fittings. The sample bag volume is connected to the wind-wave tank; the other is attached to an Analyt GFC 171 mass flow controller. Using the mass flow controller, a defined amount of air is pumped into the barrel. The positive pressure this action creates presses the vapor air mixture inside the bag into the wind-wave tank. A sketch of the setup is given in figure 6.8.

6.2.3 Pulsed UV-Laser System - Big Sky Laser CRF 200

All measurements presented in this study were conducted with a single high-power pulsed UV-laser system. This section illustrates the setup of this system at the visualization-test wind-wave tank.

The laser system acquired after initial measurements using the setup outlined in section 6.1 is a Big Sky Laser CRF 200 UV (266 nm) produced by Big Sky Laser (now Quantel-USA). It is a Nd:YAG system whose natural 1064 nm emission is frequency doubled

twice by harmonic generation in two non-linear crystals, resulting in an emission wavelength of 266 nm. The CRF laser head (figure 6.9) features a compact design of 51 cm×170 cm×130 cm size and 0.9 kg weight. It is of high stability according to military laser standards, therefore being able to operate in a temperature range from 5 °C to 60 °C. It can be transported without need of realignment, has been tested upon a vibration rig for mechanical stability, and is splash water proof. These characteristics



Figure 6.9: Big Sky Laser CRF 200 Laser Head (Source: Quantel data sheet)



Figure 6.10: ICE 450 integrated cooling and electronic unit (Source: Quantel data sheet)

render the system ideal for use at wind-wave tanks. The device provides a pulsed beam at 266 nm with an energy of 51.5 mJ and 20 pulses per second. The pulses have a width of 6.5 ns, resulting in a peak power of 7.92×10^6 W and an average power of 1.03 W. The beam diameter at the laser head aperture is 4.9 mm and the emitted beam's divergence is 0.7 mrad. The laser head is controlled by the ICE 450 power supply and cooling unit (figure 6.10). The ICE 450 is linked to the laser head by two electrical cables and two coolant lines of a length of 3 m each allowing for a flexible setup of the laser head. The unit permits direct triggering of both the flashlamp pumping the laser and the Pockels cells within the laser head responsible for q-switching². Concerning the experiments described here the most convenient way of triggering the laser output is the flashlamp, resulting in a delay between trigger signal and laser output of 675 μ s. Triggering is necessary to achieve synchronization with the camera.

The average power output of the laser system is not a concern since it stays well below critical power levels for matter vaporization. The unfocused beam has an irradiance

²Q-switching refers to a technique of short laser pulse generation, where intracavity losses are modulated to generate a high energy, pulsed laser output.

of 55000 W/m^2 . Even focused down to a beam diameter of 1 mm, which proved to be the applicable limit of this system, the irradiance of $1.311 \times 10^6 \text{ W/m}^2$ does not cause any problems. The peak power, however, causes serious trouble for practical experimentation in a wind-wave tank. The unfocused beam has a peak irradiance of $4.2 \times 10^{11} \text{ W/m}^2$. Typical laser irradiances used for material vaporisation³ are of the order of $1 \times 10^{10} \text{ W/m}^2$. The unfocused beam is able to evaporate non-transparent matter. The effects of pulsed laser radiation on the water surface are hard to quantify or predict. The absorption of water is shown in figure 6.11. At the excitation wavelength of 266 nm, the extinction coefficient is below 10^{-7} cm^{-1} , which results in an energy deposition of $6.37 \times 10^{-7} \text{ J/cm}^3$. The usual threshold for laser evaporation of water is 10-40 J/cm^2 and thus well above this limit.

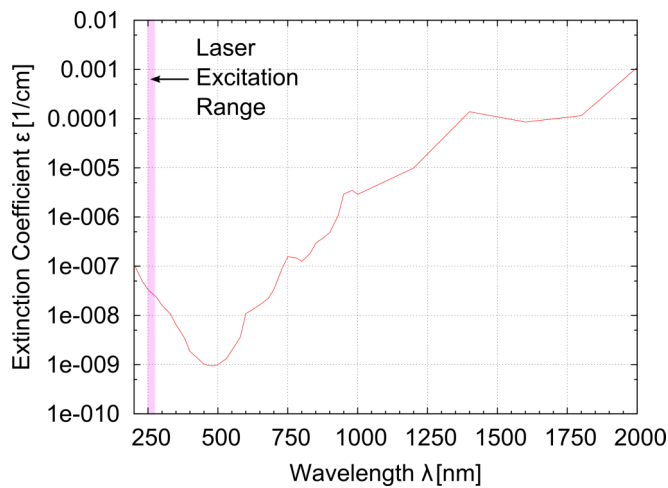


Figure 6.11: The absorption spectrum of water in the UV to near IR range adopted from Hale and Querry [24]. At the laser excitation wavelength of 266 nm the absorption is below 10^{-7} cm^{-1} .

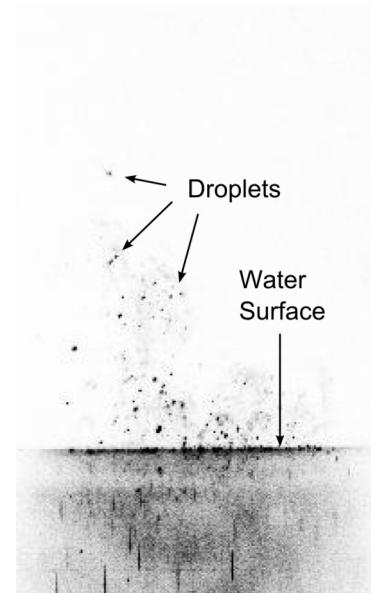


Figure 6.12: The evaporation of water in the laser sheet focus. Bursting bubbles produce water droplets that refract light into the camera

Water impurities like the fluorescent tracers entering the water during the experiments enhance the energy absorption of water. Further, the absorption characteristics of water for short high energy pulses can be significantly higher than for continuous light [49]. First experiments using this laser system showed water evaporation in the laser focus. This creates a severe problem for experiments and was not taken into consideration

³For an in depth review of laser induced ablation and plasma generation and its application in life-sciences see Vogel and Venugopalan [67]

when the CRF 200 laser system was chosen. If the water surface was constantly being evaporated the gas transfer would also be influenced. In this way the experiments would be complicated or even invalidated. To reduce the irradiance of the laser beam a cylindrical lens was inserted into the beam path to expand the beam into a light sheet parallel to the focal plane of the camera. The fluorescence signal is later attained by horizontal summation across the sheet. If the sheet is not wide enough, the energy density can still be sufficient to evaporate water. In figure 6.12 water evaporation and bubble bursting in the focus of a laser sheet is shown. In contrast to a reduction of the laser output energy, the method of widening the beam has the advantage of preserving the signal strength but the disadvantage of complicating the data analysis (see section 7.3.3).

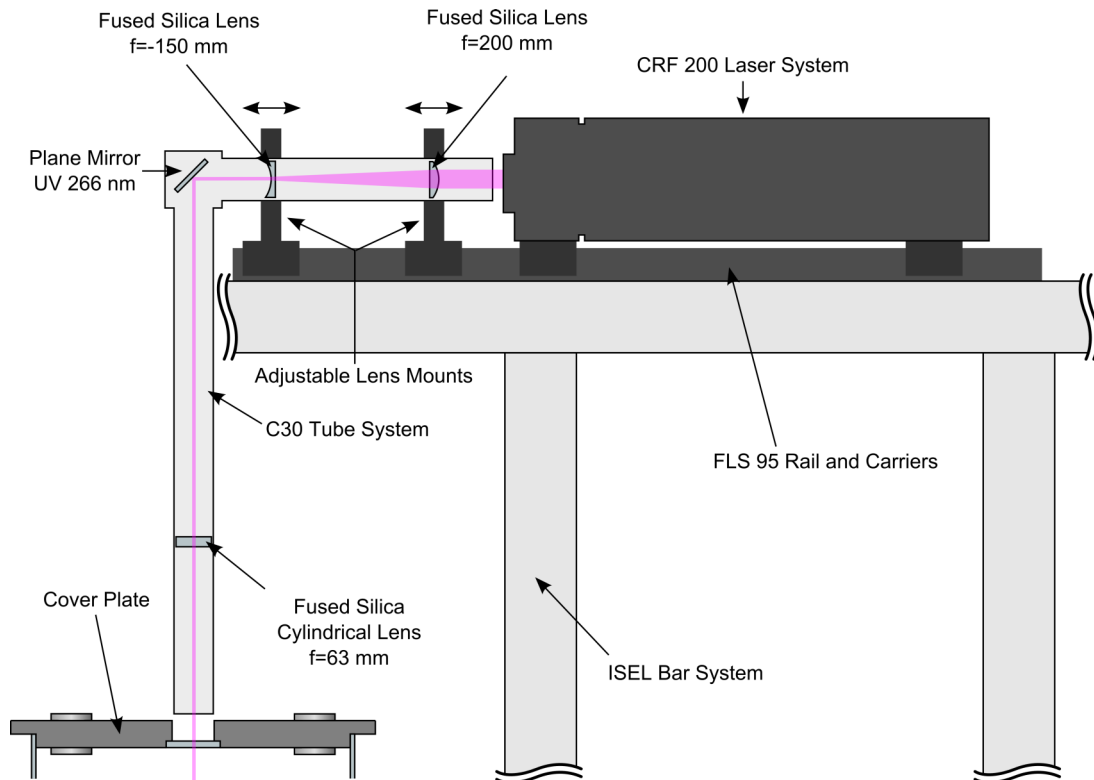


Figure 6.13: Laser setup at the visualization-test wind-wave tank The laser head is set up on the ISEL bar system of the wind-wave tank. Focusing optical elements are directly attached to the laser head while the cylindrical lens responsible for expanding the beam into a sheet is installed inside the C30 tube system closer to the tank.

The general setup of the laser system at the visualization-test wind-wave tank is shown in figure 6.13. The laser head is bolted to a pair of Linos X95 carriers, which are mounted on a FLS 95 rail of 750 mm length. In addition to the laser head, there are two carriers with Linos Microbench lens mounts. These hold a pair of fused silica

lenses used as a beam focusing unit. The rail is attached to the ISEL bar system of the visualization-test wind-wave tank allowing for flexible positioning of the laser system and the associated optical components.

Beam Focusing Unit As stated in chapter 5 the width of the beam directly influences the achievable resolution. For mass transfer measurements the resolution at the surface is of greater importance than in the bulk. A focused beam at the water surface gives a better resolution at the surface while deteriorating some resolution in the bulk. Two lenses are used to focus the beam on the water surface. Equation (6.1) shows how the focal lengths of two lenses are added to obtain the overall focal length, whereas equation (6.2) shows how the distance between the lenses can be determined for a given total focal length. The flexibility of the X95 carriers carrying the lenses is employed to focus the laser beam on the water surface.

$$\frac{1}{f_{\text{total}}} = \frac{1}{f_1} + \frac{1}{f_2} - \frac{d}{f_1 f_2} \quad (6.1)$$

$$d(f_{\text{total}}) = f_1 f_2 \left(\frac{1}{f_{\text{total}}} + \frac{1}{f_1} - \frac{1}{f_2} \right) \quad (6.2)$$

f_{total} is the combined focal length of two lenses with the focal length f_1 and f_2 while d is the distance between the two lenses. As can be easily derived from equation (6.1) f_{total} becomes infinite if $d = f_1 + f_2$. In this case the focusing unit acts like a telescope narrowing or widening the beam (depending on the lenses focal lengths) by f_1/f_2 . This is shown in figure 6.14. Using a diverging and a converging lens creates a virtual focal point outside the system, removing possible complications caused by a focused high powered laser beam within the setup. The combined lens system acts as a converging one if d is chosen to be greater than $f_1 + f_2$. This is shown in figure 6.15. In theory, it would be possible to use two converging lenses to create a telescope. The resulting focusing unit would have two distinct disadvantages: The system would be longer than a system containing one lens with a negative focal length as the distance for infinite f_{total} is the sum of the individual focal lengths and the system would have a real focal point within the system.

In this setup the first lens is a plano-concave lens with $f_1 = -150$ mm and the second lens is a plano-convex lens with $f_2 = 200$ mm. Both fused silica lenses have a diameter of 22.4 mm, a broadband anti-reflex coating in the UV range (see appendix B) and were manufactured by Linos/Qioptiq. The distance to the water surface of about 800 mm results in a distance of 87.5 mm between the two lenses. While this is a good starting value, manual adjustments to the distance d between the lenses had to be made before any series of measurements to ensure a good laser focus at the water surface as the formulas assume perfect thin lenses and no intrinsic laser beam divergence. As the

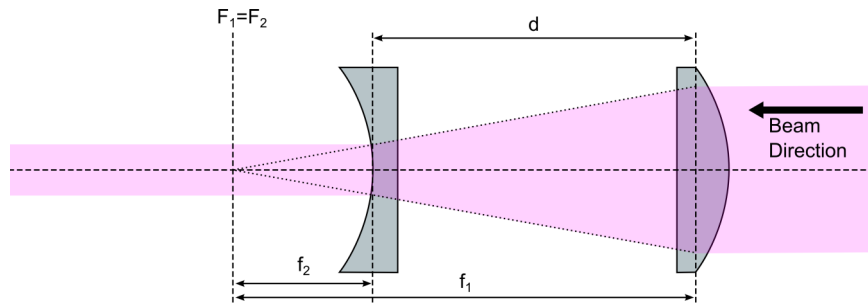


Figure 6.14: Beam 'Expander' The focal points F_1 and F_2 of the two lenses are identical. The beam is narrowed by a factor of f_1/f_2 , but remains collimated.

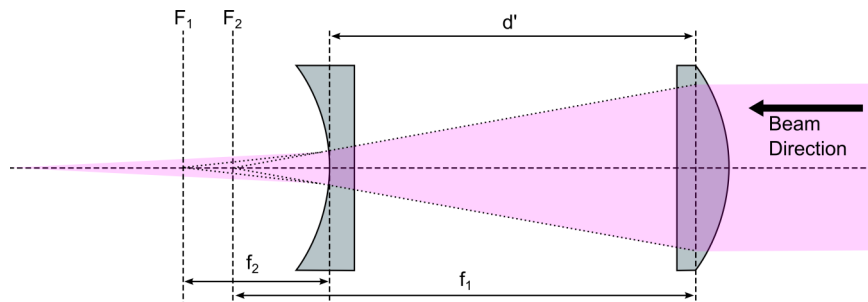


Figure 6.15: Focusing By choosing the distance d' between the two lenses to be greater than $f_1 + f_2$ they act as a converging lens. Was d smaller than $f_1 + f_2$, the beam would be divergent (not shown).

laser head cannot be mounted vertically, a dielectric-coated plane mirror suitable for application with high energy light sources deflects the laser beam into the wind-wave tank. The mirror is of elliptical shape, its size is 22.4 mm \times 31.5 mm, and it is produced by Linos/Qioptiq.

Laser Sheet Forming As mentioned above, the high radiance of the CRF 200 laser beam had to be reduced. To preserve as much signal as possible the beam is expanded into a laser sheet. In the data analysis the fluorescence signal perpendicular to the laser sheet is added to calculate a single concentration depth profile. Tests showed that a sheet width of 25 mm and above was sufficient to eliminate laser ablation at the water surface. To produce a sheet of that proportion a cylindrical fused silica lens with a diameter of 22.4 mm made by Linos/Qioptiq was mounted inside the C30 tubing system. Due to supply constraints of the manufacturer, this lens is not anti-reflex coated. The lens has a focal length of 65 mm and is mounted 30 cm above the water surface which results in a sheet width of 25 mm. Figure 6.13 depicts the position of the cylindrical lens within the system.

Laser Safety To ensure safe operation of the setup which is mounted at eye level, the beam is enclosed in a blackened tubing system. The C30 tubing system produced by Linos/Qioptiq has a diameter of 30 mm and allows for simple mounting of lenses with a diameter of 22.4 mm. A beam deflector cube, that is part of the setup, is used to hold the mirror that deflects the beam into the wind-wave tank.

6.2.4 Camera Setup

The Sensicam UV by PCO and the Pentax H2520-UVM UV objective lens detailed in section 6.1.3 were used for the CRF 200 setup as well. The camera was mounted on a Manfrotto 410 Junior geared head, allowing for flexible adjustment of the camera in three angles. The geared head was attached to the wind-wave tank's ISEL bar system making further adjustments in each of the three spatial directions possible. This very versatile setup was employed to move the camera close to the wind-wave tank and thus the fluorescence signal. To avoid occlusion of the fluorescence signal at the surface by water waves the camera was slightly tilted. Via simple geometry it can be calculated that for a camera distance of 25 cm an angle of 5° is sufficient for a wave height of up to 1 cm. Higher waves cannot be generated in the visualization-test wind-wave tank without spilling water out of the basin. Figure 6.16 shows the setup in detail.

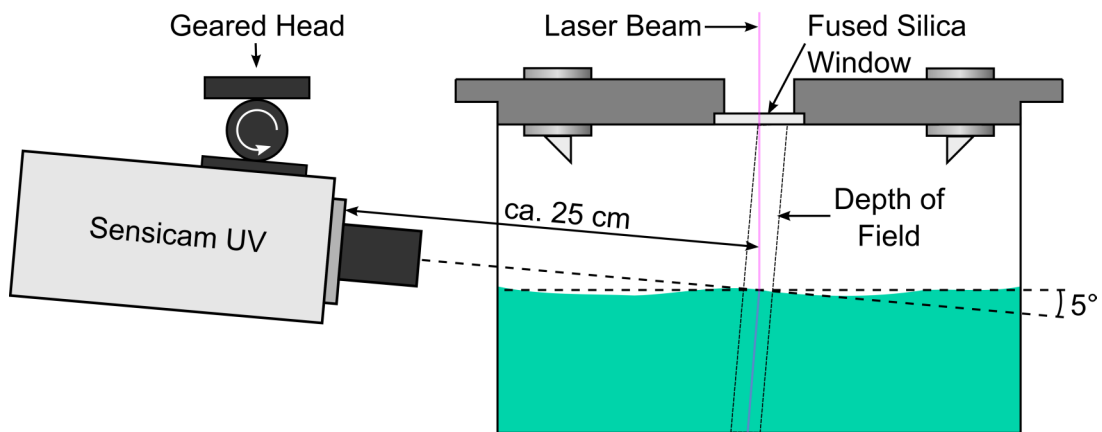


Figure 6.16: Camera Setup The Sensicam UV can be rotated along three angles via a geared head and moved in three spatial directions via the ISEL bar system. The depth of field and laser beam alignment are also shown.

The camera tilt can create a significant problem. If the angle between the laser beam and the camera is too high part of the fluorescent signal imaged by the camera will get blurred. The camera is always focused on the intersection of the laser beam and water surface, as this is the most interesting part of the concentration profile when investigating the air-water gas transfer. However, from the signal strength in the upper bulk of the air phase calibration, measurements for the tracer's concentration

are obtained (see section 7.3.3). To estimate the effect of blur, the imaging system's depth of field is calculated (for further information on depth of field and the equations used see [36, chap. 7]). At a given magnification m the maximum distance Δd between the focal plane and an object whose blur does not exceed the radius r_{pxl} of a single pixel is

$$\Delta d \approx 2 n_f r_{\text{pxl}} \frac{1 + m}{m^2}. \quad (6.3)$$

n_f is the f-number of the lens. It is defined as the ratio of the focal length f of the lens and its aperture diameter d_{lens} as $n_f = f/d_{\text{lens}}$.

The imaging system used in this setup has a f-number n_f of 2.0 and a magnification m of 0.228 at a distance d of 25 mm. Because of the low light intensities involved in the measurements, the camera was always working with a 2×2 binning where 4 pixel are read out as one. This results in an actual magnification m of 0.114 and an actual pixel radius of $8 \mu\text{m}$. Inserting these parameters in equation (6.3), the depth of field for the imaging system is evaluated to $(25.0 \pm 5.5) \text{ mm}$. With the camera tilted by 5° the signal is mapped without blur up to a distance of 62.7 mm or 448 pixel in the image taken from the water surface.

The camera is synchronized with the CRF 200 laser system, using a trigger signal generated by a Tektronix AFG 3022B arbitrary function generator. The generated signal was a 20 Hz and 5 V pulse train with a duty cycle of 5%. As described above the laser system is triggered via the flashlamp input connector. There is a $500 \mu\text{s}$ processing delay between the input signal and the flashlamp activation. With the Q-switch delay set to $175 \mu\text{s}$, the total delay between the trigger signal and the laser pulse is $675 \mu\text{s}$. Adding a laser pulse width of 6 ns and a fluorescence life-time of 100 ns or below [19] the signal is located at $675.0 \mu\text{s}$ to $675.1 \mu\text{s}$ after the triggering event. The Sensicam UV has a phasing delay of $0\text{-}75 \mu\text{s}$ and a system specific delay of $375 \mu\text{s}$. The exposure time of the camera has to be set to 8 ms or higher to avoid smearing effects. This results in an image acquisition starting $375\text{-}450 \mu\text{s}$ after the arrival of the trigger signal and ending 8 ms later. The fluorescence signal will always be generated and fade away within the cameras exposure time.

To measure the camera resolution, a checkerboard target with individual tiles of 3.3 mm width is put into the camera focus after the camera has been aligned with the laser beam. Recording the checkerboard, the resolution can be calculated by the ratio of pixel to checkerboard tiles in the image.

6.2.5 Spectrometer

As pointed out in chapter 5, obtaining actual tracer concentrations from a fluorescence measurement can be very difficult without reference values. To measure tracer vapor

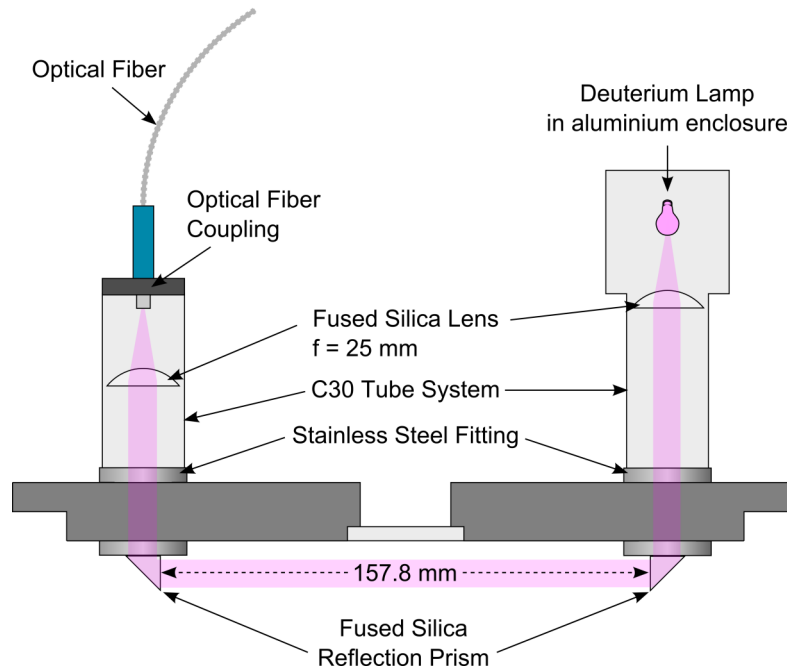


Figure 6.17: Spectrometer Setup Light emitted by a deuterium lamp is made parallel by a lens. The beam passes through the air volume of the wind-wave tank via two reflection prisms and is focused on the aperture of an optical fiber.

concentrations during the LIF measurements, an absorption spectrometry setup was built into the cover plate for the wind-wave tank. The absorption path of this setup is in the upper bulk of the wind-wave tank where concentrations can be assumed to be constant over a large area, which results in a good reference for the LIF measurements. The stainless steel fittings described in section 6.2.1 are an essential part of the spectroscopic setup. They provide optical access to the air volume of the wind wave tank. The setup is sketched in figure 6.17.

A 30 W deuterium lamp emitting light in a spectral range from 185 nm to 400 nm manufactured by Heraeus-Noblelight serves as light source (figure 6.18). It is enclosed in an aluminum body that can be screwed to the Linos/Qioptiq C30 tube system which is installed on the fittings C-mount threads. A fused silica lens with a focal length of 25 mm manufactured by Linos/Qioptiq held by the C30 tube creates a parallel beam. This beam passes through the wind-wave tank's cover plate via the fitting. The reflection prism glued to the lower surface of the fitting redirects the beam onto the second prism where the beam passes through the second fitting. The emerging light is focused by a second fused silica lens of the same type and focal length as the one before on the aperture of an optical fiber. The optical fiber was produced by Ocean Optics and is suitable for wavelengths from 180 nm to 900 nm. The optical fiber is attached to an Ocean Optics Maya2000 Pro spectrometer which gathers the spectral information



Figure 6.18: Heraeus Noblelight Deuterium Lamp (Source: Heraeus Noblelight website)



Figure 6.19: OceanOptics Maya2000 Pro spectrometer (Source: OceanOptics website.)

(figure 6.19). The Maya2000 Pro operates in a similar fashion as the HR4000 detailed in section 6.1.3. Light entering the opening is diffracted and then focused upon a CCD array with 2048×64 pixel. It has a resolution of 0.1 nm with a spectral bandwidth of 190-290 nm. The pixel are read out by a 16 bit analog-digital converter.

7 Experimental Procedure

To compare a variety of tracer substances a measurement and evaluation scheme was developed. All measurements and results presented in chapter 8 were conducted following this outline. Before the measurements were conducted several substance properties had to be researched. Since the preliminary measurement setup described in section 6.1 did not provide the intended quantifiable fluorescence quantum yield and absorption cross section results the optical properties were obtained from literature data, too. The measurements themselves use a common set of experimental conditions provided in section 7.2. Subsequently the data acquisition and evaluation is detailed for each of the measurement systems involved.

7.1 Important Tracer Attributes

Before any measurements could be conducted an extensive literature review was carried out in order to collect important tracer data.

Substance Property Sources Common substance properties like the molar mass, density, melting point and boiling point were taken from the chemical suppliers data sheet, unless otherwise noted. All substances employed in this study were supplied by Alfa Aesar. Other properties like the fluorescence quantum yield, absorbance, solubility and diffusivity of the individual tracer substances were taken from a large variety of sources. The references can be found in the individual tracer sections in chapter 8.

Health Considerations Wind-wave facilities are complex and big instruments. While they can usually be considered to be closed systems in the sense of the processes to be observed, there is always a chance of tracer molecules leaking into the laboratory. To prevent this, the pressure inside the facility is kept below the outside pressure. Nonetheless, tracers with a low risk to personal health are preferable. Substances that pose a severe health risk, either due to high carcinogenicity or direct effects on the experimenters health, are unsuitable for experiments in wind-wave tanks.

Vapor Pressure Knowledge about a substance's vapor pressure is of great importance when determining its suitability for LIF measurements in the gaseous phase. The higher a substance's vapor pressure the more molecules can be introduced into the measurement system in a short amount of time. This study relies on literature data for the determination of the vapor pressure. A common way to calculate the vapor pressure is the Antoine equation which allows the evaluation of the relation between vapor pressure and temperature. The Antoine equation uses a set of fitted parameters derived from vapor pressure measurements. A single parameter set is sufficient for the small temperature ranges of interests in wind-wave tanks experiments, which at most use a range of 10°C and 40°C.

For historic reasons, the Antoine equation and its parameters are often presented in the following form:

$$\log_{10} P_{\text{vap}} = A - \frac{B}{C - T[^\circ\text{C}]} \quad (7.1)$$

where p is the vapor pressure in millimeter of mercury, T is the temperature in degrees Celsius and A , B and C are the fitted parameters. In this study the Antoine equation was used with mbar as unit of pressure and the natural logarithm. The parameters found in older chemical literature have to be changed as follows:

$$\begin{aligned} A_{\text{conv}} &= \ln(10) \left(A + \log_{10} \frac{1013.25}{760} \right) \\ B_{\text{conv}} &= \ln(10)B \\ C_{\text{conv}} &= C \end{aligned} \quad (7.2)$$

(1013.25/760) is the conversion factor between mmHg and mbar. The final form of the Antoine equation where P_{vap} is given in mbar as used within this work is:

$$\ln P_{\text{vap}} = A_{\text{conv}} - \frac{B_{\text{conv}}}{C_{\text{conv}} - T[^\circ\text{C}]} \quad (7.3)$$

Once a substance's vapor pressure is known, the number of molecules in air saturated with the substance can be calculated. The molar volume of an ideal gas is

$$\frac{V}{n} = \frac{RT}{P_A} \quad (7.4)$$

where V is the volume of the gas, n the number of moles, R the universal gas law constant (8.3145 m³ Pa/(mol K)), T the temperature and P_A the ambient pressure. At a temperature of 25°C and a pressure of 1.013 bar the molar volume of an ideal gas is 24466 cm³/mol. Assuming the mixture of gases behaves like an ideal gas the ratio of the vapor pressure P_{vap} and the ambient pressure P_A is equal to the ratio of the molecule density of the tracer ρ_{tracer} and the air tracer mixture ρ_{total} :

$$\frac{P_{\text{vap}}}{P_A} = \frac{\rho_{\text{tracer}}}{\rho_{\text{total}}} \quad (7.5)$$

With the molecular density $\rho_{\text{total}} = 6 \times 10^{23} / 24466 \text{ cm}^3$ the molecular density of the tracer in air becomes:

$$\rho_{\text{tracer}} = \frac{P_{\text{vap}}}{P_A} \frac{6 \times 10^{23}}{24466 \text{ cm}^3} \quad (7.6)$$

7.2 Test Conditions for the Tracer Study

To ensure easy comparison of the measurements they shared a set of common conditions.

Camera Setup and Setting Prior to the tracer measurements, the camera was focused on the intersection of water surface and laser sheet. The magnification was determined using a checkerboard target. The vertical resolution was $70 \mu\text{m}$ per pixel. The camera setup was not changed between the measurements to get comparable results. Only slight readjustments were done if necessary to ensure a sharp image. Unless otherwise noted, the camera was always set to a binning of 2×2 resulting in a horizontal resolution of $140 \mu\text{m}$ per pixel and operated at a gain of 50. The image acquisition and laser pulse were synchronized by a waveform generator (see section 6.2.4). The exposure time of 8 ms was chosen to minimize camera artifacts. But the laser pulse with a width of 6 ns and the fluorescence signal with typical life-times of 10 ns or less give rise to a signal duration of approximately 16 ns within the camera's exposure time. The system operates at the maximum frequency allowed by the CRF 266 laser system, which is 20 Hz.

Wind speed All measurements were performed setting the wind generating fan to a frequency of 13.7 Hz, corresponding to an average wind speed of ca. 3.3 m/s at a height of 4 cm above the water surface. After each measurement the wind profile was obtained using the Pitot-tube setup and the friction velocity u_* was acquired from these measurements (see section 7.3.4).

Water All measurements were conducted using purified water (see appendix A.2.1). The water in the tank was changed between measurements to guarantee uncontaminated measurements.

Laser System The CRF 266 laser system was used with a Q-switch delay of 175 ms for all measurements to ensure common parameters. This is the setting of maximum efficiency. With a laser sheet width of 3 cm and a laser sheet depth of 1 mm this results in an average laser irradiance $E_{\text{avg.}}$ of 4.46×10^{18} photons/cm² s (5.11) and a peak irradiance E_{peak} of 3.72×10^{25} photons/cm² s (5.12).

Laser Excitation Limit The fluorescence excitation limit can be calculated if the fluorescence life-time of a tracer is known. The excitation limit of a specific tracer can be calculated using equation (5.6). If the irradiance E of the laser is much lower than the maximum irradiance E_{max} ($E \ll E_{\text{max}}$) the excitation is called weak ensuring operation in the linear fluorescence regime. As can be seen in the individual data sections, this always holds true for the average laser irradiance $E_{\text{avg.}}$ but only occasionally for the peak irradiance E_{peak} . This renders measurements in an optical thin medium crucial to ensure a linear relation between concentration and fluorescence signal (see section 5.3.2).

Saturation Limit The saturation limit is the maximum tracer molecule density within the wind-wave tank before the air has to be considered an optically thick medium. As has been derived in section 5.3.2, the optical thickness is the length x after which the intensity of the incoming laser beam is reduced to $1/e$. For this study, the maximum concentration provided in the individual tracer sections of chapter 8 correspond to an optical thickness of 50 cm. During a measurement the tracer is injected and a maximum concentration is reached within seconds. At this maximum concentration the excitation intensity in the imaged region is down to 90% of its original intensity. This does not cause problems for the bulk fluorescence, as this is gathered over an area of 1 cm. Even at maximum concentration that would correspond to a variation of only 2.5% in excitation intensity. To study the profiles it is advisable to use either profiles acquired before maximum concentration is reached or profiles acquired after the concentration peak.

Tracer Injection Depending on the maximum concentration usable (see above) the tracers were injected into the wind-wave tank employing either 1 l oder 10 l gas bags. To guarantee a saturated environment within the sample bag the amount of tracer inserted needs to be calculated. The partial pressure of the tracer in comparison to the total pressure states the volumetric percentage the tracer takes up. Taking into consideration the tracer's molar volume and density in liquid state the minimum tracer volume to be inserted into the sample bag can be calculated using equation (7.5):

$$V_{\text{tracer}} = \frac{P_A}{RT} \times \frac{V_{\text{bag}} P_{\text{vap}}}{P_A} \times \frac{M}{\rho} \quad (7.7)$$

where V_{tracer} is the volume of the tracer to be inserted into the sample bag, V_{bag} is the volume of the sample bag, P_{vap} is the vapor pressure of the tracer and M and ρ are the tracer's molar mass and density, respectively. Taking acetone as an example with a vapor pressure of 308.04 mbar, a molar mass of 58.08 g/mol and a density of 0.79 g/cm³ at least 9.138 ml of acetone must be inserted into a 10 l sample bag to ensure a saturated environment.

As most tracers' rate of evaporation is unknown, it is important to prepare the sample bag with the tracer two or three hours before the measurement. Spreading the tracer across the inner surface of the bag allows faster evaporation by increasing the liquid surface. A study by the manufacturer SKC Inc. shows that most volatile organic compounds can be stored in the bags for 24 h without losses above 5% [11].

7.3 Data Acquisition and Processing

A Heurisko Developer workspace controlling both the camera and the spectrometer was created. It allows for the simultaneous recording of fluorescence image sequences and spectral data. The latter is acquired with an integration time of 13 ms and internally averaged over 10 individual measurements. 50 images each containing the fluorescence signal of a single laser pulse are taken by the camera during the same time period corresponding to a single spectral measurement. The camera's exposure time was set to 8 ms. The electron multiplier was set to a gain of 50 and the camera was used with a 2×2 binning.

On the computer which controls the wind-wave tank instrumentation (see appendix A) a second Heurisko workspace monitors the temperature in air and water during the measurement. The two different measurement systems are not directly linked but can be synchronized via time stamps in the collected data. As the wind-wave tank system is used for data that is not time critical this does not create any problems. At the end of an experiment the wind-wave tank system records a wind-speed profile using the Pitot-tube of the cover plate (see section 6.2.1). This profile is employed to get the characteristic value u_* , the friction velocity.

7.3.1 Spectrometer Data

The spectral information acquired by the Maya 2000 Pro spectrometer was used to determine the tracer concentrations in the wind-wave tank within the well mixed upper bulk of the air. Position and setup of the spectrometer are shown in figure 6.17. To obtain the tracer concentration at a given time the absorbance needs to be known. In the current experimental procedure it can be assumed that there is only one absorbing species in the UV regime during the measurement that changes its concentration, the tracer itself. To compute the absorbance A out of spectral data three measurements

are needed: One measurement of the spectrometers dark response, that is without any illumination, I_{dark} , one reference spectrum acquired without any absorbing substances but with illumination I_0 and the current spectral response I that is used to calculate the absorbance (see chapter 4):

$$A(\lambda) = -\log_{10} \left(\frac{I(\lambda) - I_{\text{dark}}(\lambda)}{I_0(\lambda) - I_{\text{dark}}(\lambda)} \right) \quad (7.8)$$

With the Lambert-Beer Law the tracer concentration c can be computed if the tracer's decadic molar absorption coefficient at a wavelength λ within the observed spectrum $\epsilon(\lambda)$ and the length of absorption d is known.

$$c = \frac{A(\lambda)}{\epsilon(\lambda) d} \quad (7.9)$$

The distance d in this setup is the gap between the two reflective prisms and equal to 157.8 mm. These calculation must be done for every individual channel of the spectrometer which was realized with the help of a Heurisko program.

7.3.2 Signal Strength Evaluation

The idea and derivation of the signal rating SR is shown in 5.4. To evaluate the fluorescence signal, three different signal ratings were calculated for each tracer substance, the maximum signal rating SR_{max} , the expected signal rating SR_{ex} and the measured signal rating SR_{me}

Maximum Signal Rating SR_{max} was calculated using the maximum possible tracer concentration for an optical thin medium and at a measurement distance of 5 cm. If the exponent in equation (5.14) is 0.01 or below, the decrease of the laser irradiance is 1% or less and (5.15) gives:

$$\begin{aligned} 0.01 &= \sigma_{266} \rho_{\text{max}} \cdot 5 \text{ cm} \\ \rho_{\text{max}} &= \frac{0.01}{\sigma_{\lambda} \cdot 5 \text{ cm}} \end{aligned} \quad (7.10)$$

σ_{266} is the absorption cross section at 266 nm, the excitation energy of the laser system. Using equation (5.21), SR_{max} can be calculated by:

$$SR_{\text{max}} = \eta_{\text{eff}} \sigma_{266} \rho_{\text{max}} \quad (7.11)$$

This figure gives an estimate of the maximum possible signal rating using a laser with a wavelength of 266 nm. While the above equations can be used to calculate the maximum SR for any wavelength, the availability of only a few distinct laser output wavelengths in the UV region renders such calculations pointless. SR_{\max} could be reached in the wind-wave tank experiments if the tracer injection can be further optimized allowing for any amount of saturated air and vapor mixture to be inserted into the wind-wave tank. The current setup is restricted to the use of 1 l and 10 l gas bags.

Expected Signal Rating SR_{ex} was calculated using the actual tracer concentration ρ_{exp} inserted into the wind-wave tank. The first two factors of equation (7.7) give the number of moles of tracer in the gas bag. Using the Avogadro constant $N_A = 6 \times 10^{23}$ and the air volume of the wind-wave tank (220 l) the maximum concentration during an experiment is

$$\rho_{\text{exp}} = \frac{P_A}{RT} \times \frac{V_{\text{bag}} P_{\text{vap}}}{P_A} \times \frac{N_A}{2201} \quad (7.12)$$

and SR_{ex} becomes

$$SR_{\text{ex}} = \eta_{\text{eff}} \sigma_{266} \rho_{\text{exp}} \quad (7.13)$$

This calculated signal rating is the expected value at the maximum concentration during the experiment.

Measured Signal Rating Using equation (5.28), the maximum gray value obtained in the bulk during the measurement and the calibration of the camera sensor, the actual measured signal rating is calculated. Calibration curves providing gray value as a function of the number of photons were available from a camera calibration measurement conducted by AEON Verlag & Studio. For the gain settings (5, 50) used in this study they are printed in appendix B.2.

The transmission characteristics should be taken into account. Without knowing the actual fluorescence spectra this is not possible at the moment. This results in this number always being lower than the expected signal. It can still be used to compare the tracer substances among each other and to get an insight into the transmission characteristics that depend on the wavelength of the fluorescence light.

7.3.3 Concentration Profiles

While the calculation and evaluation of the signal strength proved to be a straightforward solvable problem the concentration profiles provided a bigger challenge. The acquired data is a series of PLIF images, two dimensional fluorescence images, where the only information of interest to this study is the brightness gradient between bulk and water surface.

Obtaining Profile Data As detailed in section 6.13 the CRF 200 laser systems beam had to be widened to prevent water evaporation in the laser focus. The option of widening the beam instead of lowering the intensity was considered preferable since it would preserve more of the already weak fluorescence signal. The underlying idea of the signal processing is to treat the fluorescence information spread along the sheet as a row of individual intensity profiles that can be added to get a better signal. The data acquisition is limited not only by the low light intensity of the fluorescence signal but also by the maximum pulse frequency of the laser of 20 Hz. Even at a low wind speed of 3.3 m/s in 5 cm height which translates to a wind speed of 2.2 m/s close to the water surface the air moves 11 cm between individual measurements. Considering the laser sheet width is 2.5 cm it is impossible get continuous time-resolved measurements of transfer events as has been done for water sided measurements by Herzog [28] and Warken [74]. Therefore adding up the data horizontally does not lower the amount of useful information gathered.

Prior to any other processing of the image sequences a dark image is subtracted. This image is acquired at the beginning of each measurement with switched off laser and provides a way to correct for the background illumination and sensor noise. Before the resulting image (figure 7.1.A) can be added up horizontally the shape of the water surface has to be accounted for. This is achieved by shifting the position of the water surface in each image column to the bottom of the image. Because of the trapezoid shape of the laser sheet this cannot be done without further adjustments to the image.

Before shifting the columns the image is distorted by using a linear transformation in such a way that the laser sheet appears to be of rectangular shape. This transformation preserves the gray value of a pixel. If a row of 50 pixel is projected to a row of 100 pixel this row will have a total gray value that is twice the original value but the average gray value of each pixel in the new row will be the same as the average value of a pixel in the original. The transformation was achieved using the built-in 'TransformPerspectiveByPoints' operator in Heurisko 6.4.0. The operator needs two points on each edge of the trapezoid created by the laser sheet to run. These are entered manually. As the laser sheet and camera are fixed during a measurement this is only done once, the algorithm works automatically from there on. For more details on perspective transformation see Jähne [36, chap. 10]. The result of this implementation is shown in figure 7.1.B.

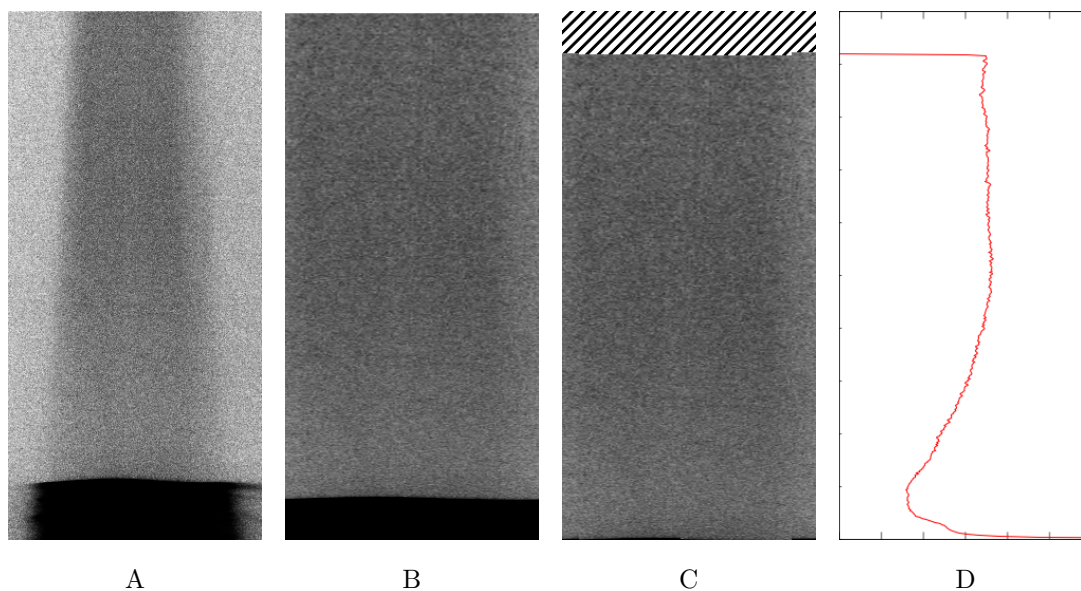


Figure 7.1: Processing of the image data

A The original data as acquired by the frame grabber. This is a negative image where dark areas have high light intensity.

B The original image is transformed in such a way that the laser sheet is rectangle in form and stretched over the image area.

C Using the strongest slope in each image column the water surface is detected and corrected for. The data is shifted to have the detected water surface coincide with the lower image border. The rows of the surface corrected image are averaged into a single value.

D After all 50 images composing a single image sequence are processed in this manner they are added up and averaged into a single profile corresponding to a single spectrometer measurement.

The next step is to correct for the shape of the water surface. Experiments with a highly soluble tracer make finding the water surface comparatively simple. The tracer concentration in the water body is much higher than in the air, the water tends to be brightly illuminated. To find the surface in a single pixel column the local derivative is calculated for each pixel. Again a built in operator of Heurisko 6.4.0 is used to accomplish this (the operator is called D1_3). In this case the location of the maximum of the derivative is the location of the water surface as this is the area of highest intensity change. Once the position of the water surface is known the position of the pixel is shifted to have the surface coincide with the bottom of the image. In doing so, the top pixel of the image are left empty as seen in figure 7.1.C.

In the final step all profiles of a single image are added up and averaged to a single profile (figure 7.1.D). A conservative estimate gives 100 pixel rows at the narrowest part of the laser sheet resulting an a signal-to-noise ratio that is $\sqrt{100} = 10$ times higher than the original. For a usual set of measurements there are 50 images in a

sequence associated with a single absorption spectrum. The profiles of these 50 images are added up and averaged to result in a single final profile with a signal-to-noise ratio of $\sqrt{100} \times \sqrt{50} \approx 70$ times higher than in the original single image. The Sensicam UV when used at a gain of 50 has a signal-to-noise ratio of 2 for very weak signals (gray value of 70 after the dark noise is subtracted).

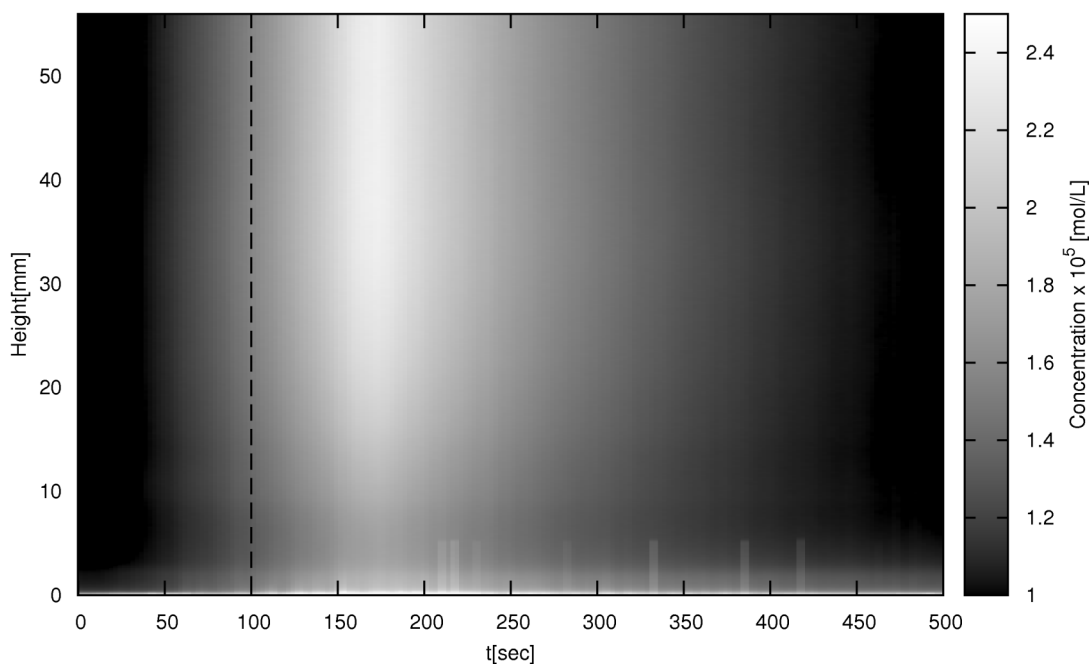


Figure 7.2: Fully processed fluorescence data from an acetone measurement. The water surface is at 0 mm, concentration profiles run from top to bottom and individual measurements are plotted next to each other against the time. The dashed line at $t=100$ s marks the position of the data shown in figure 7.1.

Evaluating the Concentration Profiles With the profile data available as gray value the last step is to calculate actual tracer gas concentrations. Both the fluorescence signal measured by the camera and the absorption measured with the spectrometer are ideally linear in their response to the tracer concentration. The fluorescence signal would be non-linearly related to the tracer gas concentration if the concentration is too high creating an optical thick medium or if the laser excitation is too high exceeding the excitation saturation threshold as explained in chapter 5. Careful dosage of the tracer injection circumvents this problem. The spectrometer response gets less reliable the longer a measurements runs, as tracer gas condenses on the surface of the reflection prisms leading to similar problems which occurred during the preliminary measurements in the reference cuvette.

To convert the gray value in an actual concentration a single pair of measurements consisting of the concentration in the bulk obtained by the spectrometer and average gray value in the top 10 mm of a profile would be enough. To ensure a good calibration the ratio of the gray value to the absorption is determined first for each profile to check for condensation on the reflection prisms. If tracer molecules condense on the prisms the tracer gas concentration is overestimated due to the addition of absorber on the surfaces. The ratio drifts away from being constant. The calibration is done using a range of measurements where the gray value to absorbance ratio is constant. These calculations are realized using a Heurisko workspace.

Once the calibration of gray value to tracer concentration is done it can be used to determine the transfer profiles. Figure 7.2 shows fully calibrated and processed data from a single measurement of acetone.

The calibrated concentration profiles were evaluated with two goals: To measure the air-sided transfer velocity k_a and to assess the distribution of the transfer resistances between the air and water phase. The air-sided transfer velocity k_a was obtained by fitting a line to the linear part of the profile and by fitting a constant function to the bulk concentration. The intersection of these two lines gives the thickness of the air-sided boundary layer (see chapter 2). The quotient of the air-sided boundary layer thickness \bar{z} and the molecular diffusion constant D of the tracer substance in air is the air-sided transfer resistance R_a . The reciprocal of the transfer resistance is the transfer velocity k_a .

$$\frac{\bar{z}}{D} = R_a = \frac{1}{k_a} \quad (7.14)$$

To get the concentration ratio between the bulk and the surface, the profile data had to be extrapolated. While the profile concentration can be directly measured, the concentration at the water surface is concealed by measuring artifacts which will be discussed later. To estimate the surface concentration the linear part of the profile is extended to the surface. By calculating the quotient of the bulk concentration and the surface concentration, a tracer can be categorized as being air-sided controlled, water-sided controlled or both (see 2.3.4).

7.3.4 Pitot-Tube Data

After each concentration profile measurement the Pitot-tube controlled by the wind-wave tank computer is used to record a wind profile. Due to limitations of the setup (see appendix A) wind speed measurements are only possible starting at 1 mm height above the wave crest. The friction velocity u_* and the roughness parameter z_0 essential for comparison with other measurements are extracted from these wind speed profiles

by fitting the form of a logarithmic wind profile to the data. Equation (2.23) was fitted to the logarithmic portion of the velocity profiles acquired with the pitot-tube. Figure 7.3 shows an exemplary fit of one such measurement. The fit routine employed is a least squares fit implemented in the Gnuplot 4.4 software.

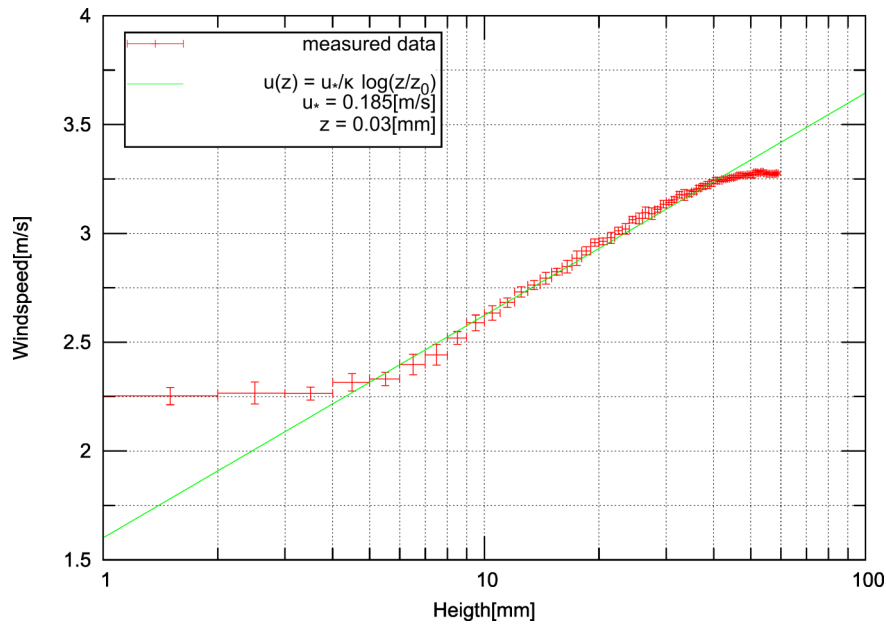


Figure 7.3: A wind profile measured at a motor frequency of 13.7 Hz just after a transfer measurement using acetone as tracer. The green line shows the fitted function of the wind profile.

7.3.5 Box Model

To determine the total transfer velocity from the acquired data sets, a box model was used to characterize the process. The model is shown in figure 7.4. It describes the processes after the gas bag has been emptied into the wind-wave tank. The amount of tracer in the air volume $V_a c_a$ is reduced by two processes: a) Driven by the concentration difference $c_a - c_w/\alpha$ the tracer can be transported across the air water interface of area A into the water with the transfer velocity k_{total} and b) the tracer is flushed out of the air volume with a leakage rate of \dot{V}_a by the wind-wave tank's exhaust system.

It is assumed that the water concentration can be neglected as most tracers used are of high solubility α . This results in the following differential equation:

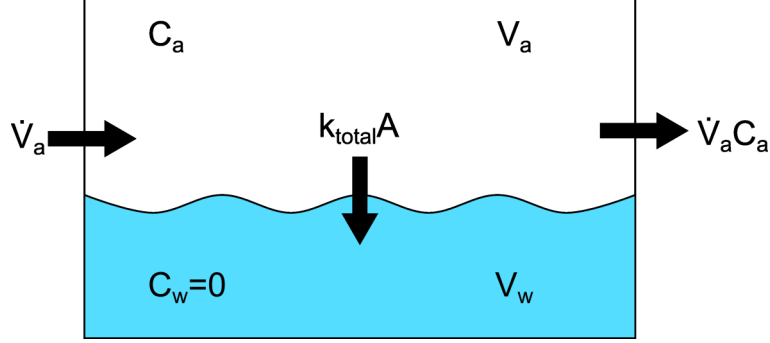


Figure 7.4: Box model describing the transfer processes during the experiment. The concentration in the air c_a is reduced by transfer across the water surface A with a transfer velocity k_{total} and by the leakage caused by the exhaust system of the wind-wave tank $\dot{V}_a c_a$. The concentration in the water c_w is assumed to be 0.

$$\begin{aligned} V_a \dot{c}_a &= -A k_{total} \left(c_a - \frac{c_w}{\alpha} \right) - \dot{V}_a c_a \\ V_a \dot{c}_a &= -A k_{total} c_a - \dot{V}_a c_a \end{aligned} \quad (7.15)$$

Solving equation (7.15) for \dot{c}_a the equation can be easily integrated, assuming a constant leakage rate \dot{V}_a :

$$\begin{aligned} \dot{c}_a &= -\frac{A k_{total} c_a + \dot{V}_a c_a}{V_a} \\ \dot{c}_a &= -c_a \left(\frac{A k_{total} + \dot{V}_a}{V_a} \right) \\ c_a(t) &= c_a(0) e^{-\frac{A k_{total} + \dot{V}_a}{V_a} t} + \text{const.} \end{aligned} \quad (7.16)$$

By fitting equation (7.16) to the decrease of the fluorescence signal in the bulk of the gaseous phase the transfer velocity k_{total} can be acquired as a fit parameter. The same can be done for the absorption measured by the spectroscopic setup. In the case of a flawless measurement the transfer velocity determined by the fluorescence evaluation should be the same as the transfer velocity resulting from the spectrometer data evaluation. If the values deviate strongly from each other, at least one of the measurement systems does not provide a signal proportional to the current concentration. For the evaluation of the data presented here a least-squares fit routine implemented into the Gnuplot 4.4 plotting program was used.

Part III

Measurements and Results

8 Tracer Characterization

To measure air-sided concentration profiles at the water surface, suitable tracer substances are needed. As mentioned in chapter 5, any substance whose concentration in air can be directly measured using a LIF setup is called a tracer within the scope of this work. No experiments attempting to visualize the air-sided concentration profiles at the air-water interface have been conducted before.

This chapter presents extensive data for ten different species of fluorescence tracers. The presented information is the result of both an extensive literature research and as well as measurements conducted and evaluated using the scheme presented in chapter 7. These measurements were only possible by relying on a wealth of knowledge available from fluorescence experiments originating in the fields of combustion diagnostics, air-flow visualization and liquid scintillators. Some of the more promising but rejected tracers encountered during the literature research are presented at the end of this chapter, including reasons why they could not be measured at this point.

8.1 Acetone

Acetone (IUPAC: Propanone) is the simplest ketone. Two carbon atoms are bound to a carbonyl group, one carbon atom double-bonded to an oxygen atom. Its molecular formula is C_3H_6O . Figure 8.1 shows its structural formula. It is a relatively light molecule whose spectrum is dominated by the carbonyl group.

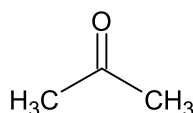


Figure 8.1: Acetone structural formula. A carbonyl group is bound to two carbon atoms. It is the source of acetone absorption in the 266 nm region.

8.1.1 Physical Properties

At normal conditions, Acetone is a highly flammable transparent liquid. Its melting point is $-95^{\circ}C$, its boiling point is $56^{\circ}C$ and its auto-ignition temperature is $465^{\circ}C$. A

mixture of 2.6 % to 12.8 % acetone vapor and air is flammable. Acetone has a molecular weight of 58.08 g/mol and a density of 0.79 g/cm³ at normal conditions.

The Acetone vapor pressure was determined for a great temperature range by Ambrose et al. [3]. Using these data, the vapor pressure between -10 °C and 70 °C can be calculated with high precision using the fitted Antoine equation [44]. This is a greater range than what is of interest for gas exchange experiments at the air-water interface where temperatures below 10 °C or above 40 °C are rarely considered. At normal temperature (25 °C), acetone has a vapor pressure of 309 mBar. Acetone is highly soluble in water. Its solubility α , expressed by Henry's Law, is 732 [6]. Being a rather lightweight molecule, Acetone's diffusion coefficient in air is 0.11 cm²/s.

8.1.2 Optical Properties

Acetone vapor fluorescence has been studied since the beginning of the 20th century and is rather well understood today. The first published measurements can be found in Damon [13]. It was quickly discovered that the strong green emission of acetone vapor was actually the emission of diacetyl. For a long time, studies focused on diacetyl as a tracer for gaseous flow visualization due to its absorption in the visible range of the electromagnetic spectrum. Lozano et al. [44] showed that using acetone vapor fluorescence is generally advantageous for flow imaging experiments if lasers of appropriate wavelengths are available. The absorption and fluorescence spectra of acetone are shown in appendix B.3.1.

Absorption The absorbance of acetone in the UV spectrum is dominated by the carbonyl group. The absorption spectrum has its maximum at 275 nm with an absorption cross section σ of 4.7×10^{-20} cm². At the excitation wavelength of 266 nm, the absorption cross section is 4.4×10^{-20} cm² [44].

It is important to note that acetone excited by high energy radiation can dissociate and produce free acetyl radicals which can recombine to form diacetyl. At lower excitation wavelengths, this is not a problem as the process becomes less probable with decreasing wavelength. In addition, diacetyl absorbance and fluorescence quantum efficiency is very low at wavelengths below 300 nm [44].

Luminescence Acetone has a very low fluorescence quantum yield of just 0.0020, but this is partially balanced by the high vapor pressure. The fluorescence emission of acetone occurs over a wide range of wavelengths from 350 nm to 550 nm with a peak at 435 nm. The fluorescence life-time of acetone is 1.7 ns when excited with a 280 nm light source [8]. For excitation with a 266 nm laser, this gives a good upper estimate as the fluorescence life-time is reduced at shorter excitation wavelengths.

8.1.3 Safety and Health Considerations

Acetone is considered mildly toxic. Exposure to acetone vapor over prolonged time can cause irritation of the eyes, mucus membranes, and upper respiratory tract. It can also cause headaches, nausea, and dizziness. While harmful if swallowed, acetone is not considered a carcinogen. Acetone's odor threshold is 2 ppm, while harmful effects begin at 1000 ppm with the irritation of the eyes. At concentrations of 9200 ppm, Acetone causes irritation of the throat. As mentioned above, acetone of concentrations between 2.6% and 12.8% in air is highly flammable. While it is highly unlikely to reach these conditions in the laboratory due to exhaust systems, this has to be taken into consideration for experiments in the closed system of a wind-wave tank. The amount of air saturated with acetone vapor should not exceed 2.6% of the facilities air volume.

8.1.4 Measurement Parameters

Laser Excitation Limit Using the fluorescence life-time of acetone of 1.7 ns, the excitation limit of acetone was determined to be 1.34×10^{28} photons/cm² s. This is well above the estimated photon density of the laser sheet of 3.72×10^{25} photons/cm² s. The excitation of acetone by the CRF 266 laser system can be considered weak, simplifying the data interpretation as discussed in chapter 5.

Concentration Limit With an absorption cross section $\sigma_{266 \text{ nm}}$ of 4.4×10^{-20} cm² at 266 nm, acetone absorbance is rather weak resulting in a relatively high concentration limit before the air vapor mixture has to be considered optically thick. The maximum concentration of acetone vapor for the use in LIF experiments in an optically thin medium is 7.86×10^{-04} mol/l. This translates to a vapor concentration of 6.31%, which cannot be used as it is above the limit for an explosive mixture of 2.6%.

Tracer Injection Using equation 7.7, the amount of liquid acetone to be inserted into the gas bag was determined. At a laboratory temperature of 23.3 °C, the acetone vapor pressure is 309 mbar. A molecular mass of 58.08 g/mol and a density of 0.79 g/cm³ translate to 0.86 ml of liquid acetone for one liter of air to be saturated. With a maximum acetone concentration of 7.86×10^{-04} mol/l, a maximum of 13.9l of air saturated with acetone vapor can be inserted into the wind-wave channel without risking LIF operation in an optical thick medium. Thus the 10l tedlar bags were used for acetone measurements. Before the measurement, 8.57 ml of liquid acetone were injected into the bag. After a period of 2 hours, the air in the bag was assumed to be saturated with acetone vapor. The flow controller, used to inject the saturated air into the wind-wave tank, allows for a maximum air flow of 4l/min. 10l of tracer saturated air were injected into the wind wave channel over a period of 150 s.

8.1.5 Signal Strength

The

The relatively low fluorescence yield and absorption cross section of acetone is balanced by its high vapor pressure resulting in a comparatively good signal.

Acetone			
ρ_{\max} :	$4.73 \times 10^{22} \text{ 1/m}^3$	Fluor. Yield Φ_f :	0.0020
ρ_{exp} :	$3.18 \times 10^{22} \text{ 1/m}^3$	SR_{\max} :	$4.45 \times 10^{-04} \text{ 1/m}$
$\text{Air}_{\text{sat.}}/\text{Air}_{\text{pure}}$:	6.31 %	SR_{ex} :	$2.80 \times 10^{-04} \text{ 1/m}$
Sat. Excitation:	$1.34 \times 10^{28} \text{ N}_{\text{ph}}/\text{cm}^2 \text{ s}$	SR_{me} :	$4.09 \times 10^{-05} \text{ 1/m}$

Table 8.1: Evaluation of acetone as a fluorescence tracer in wind-wave tank experiments.

The measured signal rating, SR_{measure} , is 14 % of the theoretically expected signal, SR_{expect} . Considering the fact that the expected signal does not take photon loss at the wind wave tank windows, the camera objective lens and the sensor efficiency into account, this result is quiet satisfactory.

Comparing the expected signal rating with the maximum signal rating, SR_{\max} , possible with the CRF 266 laser system if ideal tracer concentrations can be achieved shows that the system operates in a very efficient region already. The signal could be enhanced by mere 33% by optimizing the tracer injection. Potential risk due to flammable vapor concentrations should be kept in mind.

8.1.6 Boundary Layer Visualization

Figure 8.2 shows the course of the conducted transfer measurements. At $t=0 \text{ s}$, 10l saturated air-vapor mixture were injected into the wind wave tank for a duration of 150s. Afterwards, the concentration decreases due to acetone accumulation in the water and the forced leakage caused by the air flushing system of the tank, which was not yet controllable at that moment. Fitting a simple box model to the exponential decreases of the two data sets results in the transfer velocities $k_{a,\text{bulk}}$ and $k_{a,\text{spec}}$ shown in table 8.2 for the LIF and spectroscopic data, respectively. As expected, the data of the measurements using the absorption spectrometer results in a lower transfer velocity as acetone vapor condenses at the reflective prisms of the setup, thus overestimating the residual concentration.

Figure 8.3 shows the concentration profile at $t=172.5 \text{ s}$, just 22.5s after the volume of the tracer bag has been emptied into the wind-wave tank. The general shape of the profile is as expected, showing a constant intensity at the upper end, the bulk, and a linear decrease near the water surface. Immediately above the water surface, the

Acetone			
$u_*: 0.18 \text{ m/s}$			
c_{bulk} :	$4.08 \times 10^{-04} \text{ mol/l}$	Boundary layer:	$20.7 \pm 0.6 \text{ mm}$
c_{surf} :	$1.97 \times 10^{-04} \text{ mol/l}$	Diffusion:	$0.11 \text{ cm}^2/\text{s}$
$c_{\text{surf}}/c_{\text{bulk}}$:	0.48	$k_{\text{a, profile}}$:	$182 \pm 5.2 \text{ cm/h}$
Solubility α :	732	$k_{\text{total, bulk}}$:	$708 \pm 1.9 \text{ cm/h}$
Calibration:	$6.95 \times 10^{-07} \text{ mol/l [DN]}$	$k_{\text{total, spec}}$:	$426 \pm 1.9 \text{ cm/h}$

Table 8.2: Results of acetone mass transfer measurements. The spectrograph data shows the expected lower transfer velocity. The result of the profile measurement is of the same order of magnitude as the other measurements. Taking the uncertainty of the diffusion constant into account this can be considered satisfactory.

gray value, which is proportional to the tracer concentration, increases rapidly. With a solubility α of 732, acetone accumulates rapidly in the water body. As mentioned before, according to Henry's Law the water concentration at the surface is equal to the air concentration at the surface times α resulting in a fluorescence signal in the water of α times the strength of the air-side.

While an illumination sheet width of 1 mm and a camera angle of 5° would result in an overlap in the camera image of only $87 \mu\text{m}$, i.e. half a pixel, of water-sided and air-sided fluorescence signal, several factors increase the effect: The refraction of both the laser sheet and the fluorescence light generated in the water near the water surface and the movement of the water surface that acts like a tilted mirror or lens cause some of the water-sided fluorescence light to show up on the sensor system at much larger heights. The much higher signal strength in the water compared to air causes even weaker refracted light, i.e. secondary sources, to contaminate the recorded image in some regions.

While the previously mentioned effects are very hard to quantify, they are easily seen in the data. Up to a height of about 6 mm above the water surface, the water signal clearly interferes with the measurement. To compensate for that problem, the linear decrease is fitted only down to a height of 8 mm and the surface concentration in air is estimated by extrapolation.

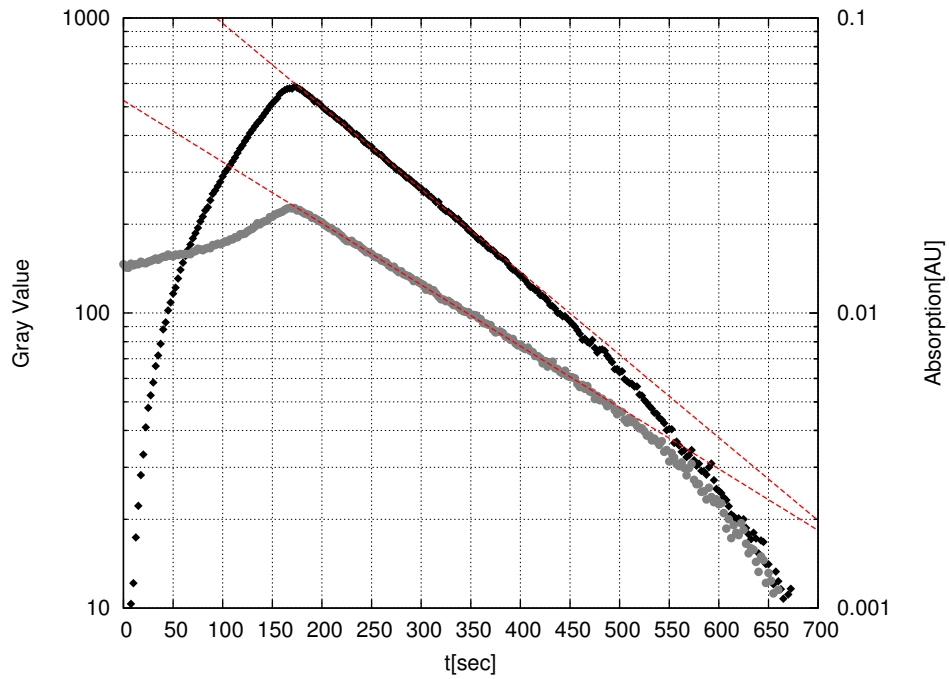


Figure 8.2: Sequential development of the fluorescence signal strength in the bulk (black squares) and the absorption measured by the spectrometer (gray circles) over time.

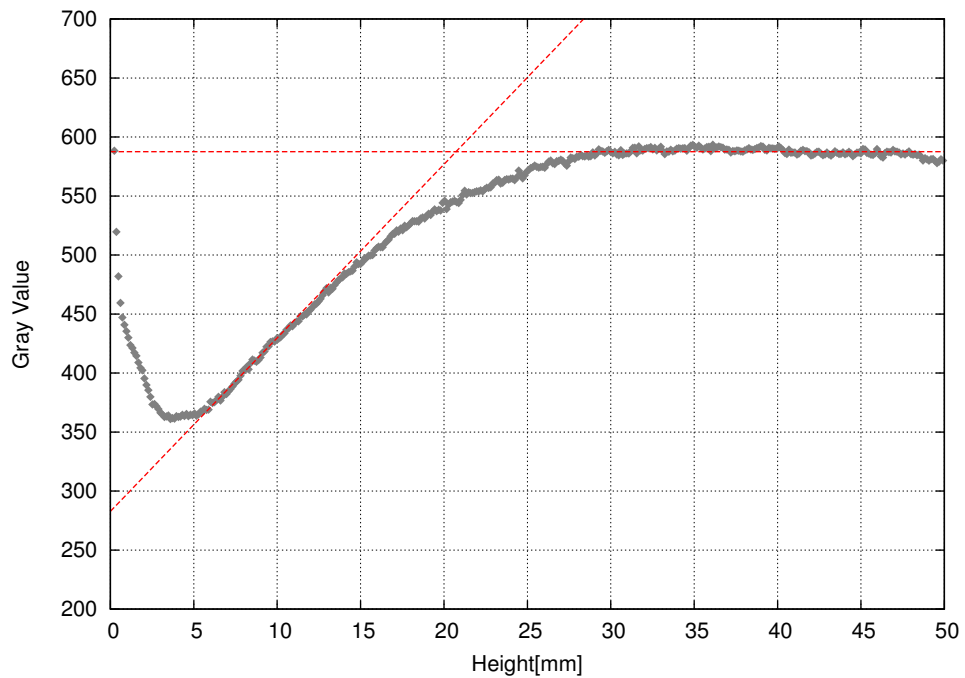


Figure 8.3: Concentration profile with fitted lines to evaluate the constant bulk concentration and the linear regress at the surface. At up to approximately 6 mm height fluorescence generated in the water interferes with the measurement.

8.2 Ethanal

Ethanal (commonly called acetaldehyde) is an aldehyde and as such has a carbonyl group within its structure as have the ketones like acetone (see section 8.1). Its molecular formula is C_2H_4O . The structural formula is shown in figure 8.4. With a structure similar to acetone and an even lower molecular weight and thus higher vapor pressure, ethanal was expected to perform rather well in wind-wave tank experiments. As is the case with many of the substances presented here, ethanal has previously been used in the study of the processes in combustion engines [5].

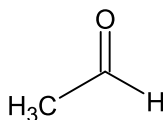


Figure 8.4: The structural formula of ethanal.

8.2.1 Physical Properties

Ethanal is a colorless and highly volatile liquid, its boiling point of $20^{\circ}C$ is the lowest of the substances in this study, causing it to boil at typical laboratory temperature while its melting point is $-123^{\circ}C$. Ethanal vapor can create an explosive mixture with air. A volumetric ratio of 4.1% to 55% ethanal vapor and air is highly combustible.

With a molecular weight of only 44.05 g/mol , its vapor pressure at room temperature 1206 mBar [9] is expectedly high. It can be calculated in a temperature range of $0.15^{\circ}C$ to $104.25^{\circ}C$ by a fitted Antoine equation [43]. To calculate the amount of liquid to be inserted into the gas bag, the density of 0.788 g/cm^3 is of importance, too. The air water partition coefficient α of ethanal is approximately half that of acetone with a value of $\alpha = 342$ [63] and its diffusion coefficient is $0.15\text{ cm}^2/\text{s}$ [78].

8.2.2 Optical Properties

As mentioned above, ethanal has previously been used in the field of combustion studies as a fluorescence tracer molecule, thus detailed information about its optical properties is available. A first comprehensive study of ethanal and other simple aldehydes was performed by Hansen and Lee [25]. The absorption and fluorescence spectra of ethanal are shown in appendix B.3.2.

Absorption The absorption spectrum of ethanal in the UV region is, as is the case for acetone, caused by the carbonyl group. The maximum absorption cross section σ is found $4.60 \times 10^{-20} \text{ cm}^2$ at a wavelength of 290 nm. At the excitation wavelength of 266 nm, the absorption cross section of ethanal is significantly lower with a value of 3.65×10^{-20} [44].

Luminescence The fluorescence quantum yield η of ethanal is very low for an excitation light source of 266 nm wavelength. Hansen and Lee [25] report a quantum yield of 0.0015. The fluorescence spectrum is strongly red-shifted to between 350 nm and 500 nm with a peak at 420 nm. The fluorescence life-time of approximately 2.5 ns allows for a very high maximum excitation irradiance.

8.2.3 Safety and Health Considerations

Ethanal is considered irritating to the eyes and the respiratory system. Concentrations of 50 ppm cause an irritation of the eyes after an exposure of 15 min while concentrations of 200 ppm can cause irritation of the nose and throat. There is some evidence for carcinogenic effects, but since ethanal occurs naturally in many food products and as an effect of alcohol consumption, this is difficult to prove.

The high flammability of the vapor is the by far greater risk when handling ethanal in a wind-wave tank experiment. As mentioned above, a volumetric ratio of 4.1% to 55% ethanal vapor and air forms an explosive mixture. Care has to be taken not to reach this ratio during experiments.

8.2.4 Measurement Parameters

Laser Excitation Limit With a fluorescence life-time of 2.5 ns and an absorption cross section σ of $4.60 \times 10^{-20} \text{ cm}^2$, the excitation limit for ethanal was calculated to be $1.10 \times 10^{28} \text{ photons/cm}^2 \text{ s}$, very close to that of acetone. The peak irradiance of the CRF 266 laser system is $3.72 \times 10^{25} \text{ photons/cm}^2 \text{ s}$, three orders of magnitude below the limit.

Concentration Limit Using the equations given in 5.3.2, ethanals absorption cross section σ of $4.60 \times 10^{-20} \text{ cm}^2$ translates to a maximum concentration of $9.49 \times 10^{-4} \text{ mol/l}$ or 1.95% before the tracer air mixture has to be considered optically thick. This result lies well below the low limit for an explosive concentration of 4.1%.

Tracer Injection The amount of liquid ethanal to be inserted into the gas bag was determined using equation 7.7. At the laboratory temperature during the experiment of 22.2 C° , the ethanal vapor pressure was 1206 mbar translating to 2.4 ml of liquid ethanal to be inserted per liter of gas bag volume. Considering the maximum concentration of 9.49×10^{-04} mol/l, a maximum of 4.3l of air saturated with ethanal vapor can be inserted into the wind-wave tank before an optically thick medium is created. A 10l tedlar bag was used for the experiment, filled with only 10 ml of liquid ethanal. It should be mentioned, though, that due to ethanal's low boiling point, the actual inserted amount of tracer molecules might be less as the substance begins to boil in the syringe before injection.

The flow controller used to inject the saturated air into the wind-wave tank allows for a maximum air flow of 4l/min. 10l of tracer saturated air were injected into the wind wave channel over a period of 150 s.

8.2.5 Signal Strength

Table 8.3 shows the results of the ethanal vapor fluorescence measurements which is in stark contrast to both the results of the acetone measurements and the expectations. Despite the higher vapor pressure and a similar absorption cross section, ethanals measured signal is only half as strong as that of acetone. Comparing the measured

Ethanal			
ρ_{\max} :	5.71×10^{22} 1/m ³	Fluor. Yield Φ_f :	0.0015
ρ_{exp} :	4.67×10^{22} 1/m ³	SR_{\max} :	3.94×10^{-04} 1/m
$\text{Air}_{\text{sat.}}/\text{Air}_{\text{pure}}$:	1.95 %	SR_{ex} :	2.55×10^{-04} 1/m
Sat. Excitation:	1.10×10^{28} N _{ph} /cm ² s	SR_{me} :	1.56×10^{-05} 1/m

Table 8.3: Evaluation of ethanal as a fluorescence tracer in wind-wave tank experiments.

signal SR_{me} to the calculated expected signal SR_{ex} shows a difference of a factor 50. With a fluorescence spectrum in between 350 nm and 500 nm, the losses due to transmission and sensor efficiency should be relatively low. With an extremely low fluorescence life-time, quenching by oxygen is highly unlikely and should not give rise to this difference. Two other possible explanations might be an actual fluorescence quantum yield that is even lower than 0.0015, reported by Hansen and Lee [25], or inconsistencies at the stage of tracer injection. Given the handling problems caused by the low boiling point, the latter seems the more plausible reason.

8.2.6 Boundary Layer Visualization

Despite the low signal, the measurements conducted with ethanal could be analyzed with regard to the mass transfer across the air-water interface. The course of the measurements is shown in figure 8.5.

Ethanal			
$u_*: 0.18 \text{ m/s}$			
c_{bulk} :	$1.91 \times 10^{-03} \text{ mol/l}$	Boundary layer:	$7.7 \pm 0.4 \text{ mm}$
c_{surf} :	$1.62 \times 10^{-03} \text{ mol/l}$	Diffusion:	$0.15 \text{ cm}^2/\text{s}$
$c_{\text{surf}}/c_{\text{bulk}}$:	0.85	$k_{\text{a, profile}}$:	$678 \pm 39.7 \text{ cm/h}$
Solubility α :	342	$k_{\text{total, bulk}}$:	$245 \pm 1.6 \text{ cm/h}$
Calibration:	$7.42 \times 10^{-06} \text{ mol/l [DN]}$	$k_{\text{total, spec}}$:	$236 \pm 0.9 \text{ cm/h}$

Table 8.4: Results of ethanal mass transfer measurements. The data calculated from the fluorescence measurements should be considered with caution, due to the very low signal.

A gas bag filled with 10l of a non-saturated mixture of ethanal vapor and air (see above) was emptied into the wind-wave tank over the course of 150 s. The decrease of the measured absorbance and the fluorescence signal was used to calculate the transfer velocity. During the experiment, the air in the laboratory had a temperature of ca. 23°C and condensation of ethanal vapor on the reflective prisms of the spectrometric setup was unlikely. The fact that the transfer velocities calculated from the respective measurement methods are close to each other underlines that assumption.

The measured profile (8.6) indicates that results from the LIF measurement are to be taken with caution. The profile shows the typical rise in intensity near the water due to a water concentration higher than the concentration in air by the factor α , but the shape of the profile above 5 mm might point to the camera sensor and laser sheet not being properly aligned during the measurement.

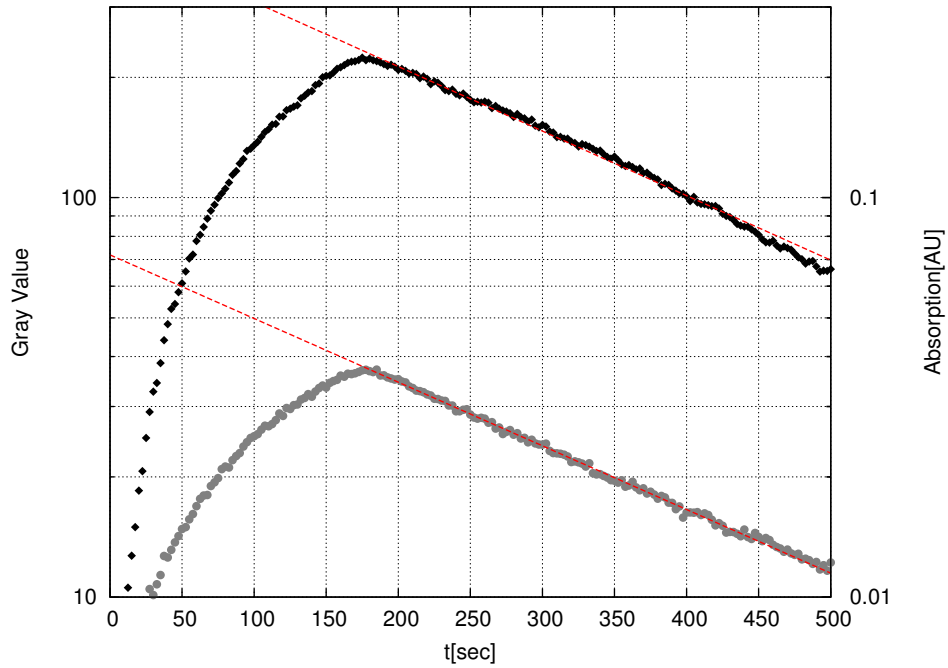


Figure 8.5: Sequential development of the fluorescence signal strength in the bulk (black squares) and the absorption measured by the spectrometer (gray circles) over time

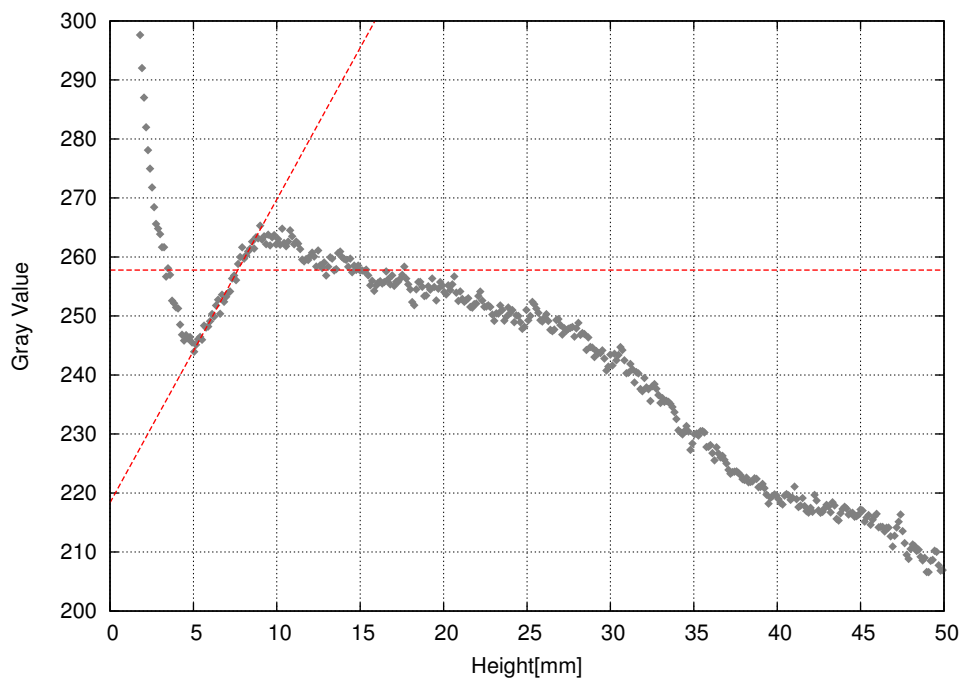


Figure 8.6: Concentration profile with fitted straight lines to evaluate the constant bulk concentration and the linear profile at the surface. The bulk concentration was estimated by fitting a constant profile into the area in between 10 mm and 20 mm above the water surface.

8.3 Fluorobenzene

Fluorobenzene is a halogenated aromatic compound consisting of a phenyl ring (C_6H_5) with an attached fluorine atom. Its molecular formula is C_6H_5F . The structural formula is shown in figure 8.7. Fluorobenzene's fluorescence characteristics have been studied in detail especially to obtain better insights into the characteristics of the phenyl group but also because of its use in liquid scintillators in nuclear physics [7].

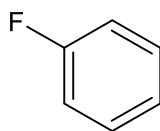


Figure 8.7: The structural formula of fluorobenzene. A single fluorine atom is bound to a phenyl ring.

8.3.1 Physical Properties

Fluorobenzene is a colorless liquid and easily flammable. Its boiling point is $85^\circ C$ and its melting point is $-45^\circ C$. Fluorobenzene has a molecular weight of 96.10 g/mol and a density of 1.02 g/cm^3 . Its vapor pressure at room temperature is 102 mBar [61]. The fitted antoine parameters allow for a calculation of the vapor pressure in between $-18^\circ C$ and $83^\circ C$, a more than sufficient range for experiments at a wind-wave tank.

Being a nearly non-polar substance, fluorobenzene is barely soluble in water. Its air-water partition coefficient $\alpha = 3.9$ [45] puts it firmly into the region of water-side controlled substances.

8.3.2 Optical Properties

In the past, fluorobenzene's fluorescence characteristics have been studied especially for its use in scintillators. Recently, its use in spray diagnostics has been further investigated [18].

Absorption Fluorobenzene has a local absorption maximum at the excitation wavelength 266 nm with an absorption cross section σ of $4.93 \times 10^{-18} \text{ cm}^2$ [7] which is two orders of magnitude above the absorption of acetone.

Luminescence The fluorescence quantum yield η of fluorobenzene is 0.13, again two orders of magnitude higher than that of acetone, rendering it an ideal tracer in terms of signal strength. The redshift of the fluorescence spectrum is not very pronounced. With fluorescence between 265 nm and 340 nm (with a peak at 275 nm), the use of UV optics is necessary when studying fluorobenzene [7]. The fluorescence life-time of fluorobenzene is 8 ns.

8.3.3 Safety and Health Considerations

The inhalation of fluorobenzene can cause irritation of the respiratory system and symptoms of drunkenness. Prolonged exposure might also cause kidney and liver damage. No data suggesting fluorobenzene to be carcinogen is available.

8.3.4 Measurement Parameters

Laser Excitation Limit With a fluorescence life-time of 8 ns and an absorption cross section σ of $4.93 \times 10^{-18} \text{ cm}^2$, the excitation limit for fluorobenzene was calculated to be $2.53 \times 10^{25} \text{ photons/cm}^2 \text{ s}$. The peak irradiance of the CRF 266 laser system is $3.72 \times 10^{25} \text{ photons/cm}^2 \text{ s}$, above this limit. When working with this tracer it is important to ensure measurements in an optically thin medium.

Concentration Limit Fluorobenzenes absorption cross section σ of $4.93 \times 10^{-18} \text{ cm}^2$ results in a maximum concentration of $7.01 \times 10^{-06} \text{ mol/l}$ or 0.17%, before the tracer air mixture has to be considered optically thick.

Tracer Injection Due to the high fluorescence quantum yield and absorption cross section, fluorobenzene was injected using a 1 l tedlar bag. The amount of liquid fluorobenzene to be inserted into the gas bag was determined using equation 7.7. At the laboratory temperature during the experiment of 23.0 C° , its vapor pressure was 102 mbar translating to 0.33 ml of liquid fluorobenzene to be inserted into the gas bag.

Considering the maximum concentration of $7.01 \times 10^{-06} \text{ mol/l}$, a maximum of 0.4 l of air saturated with ethanal vapor can be inserted into the wind-wave tank before an optically thick medium is created. The 1 l gas bag was filled with only 0.1 ml of liquid fluorobenzene to compensate for that problem.

The flow controller used to inject the saturated air into the wind-wave tank allows for a maximum air flow of 4 l/min. The content of the gas bag was emptied into the wind-wave tank in a period of 15 s.

8.3.5 Signal Strength

Table 8.5 shows the results of the fluorobenzene vapor fluorescence measurements. The

Fluorobenzene			
ρ_{\max} :	$4.22 \times 10^{20} \text{ 1/m}^3$	Fluor. Yield Φ_f :	0.13
ρ_{exp} :	$2.91 \times 10^{20} \text{ 1/m}^3$	SR_{\max} :	$2.71 \times 10^{-02} \text{ 1/m}$
$\text{Air}_{\text{sat.}}/\text{Air}_{\text{pure}}$:	0.17 %	SR_{ex} :	$1.86 \times 10^{-02} \text{ 1/m}$
Sat. Excitation:	$2.53 \times 10^{25} \text{ N}_{\text{ph}}/\text{cm}^2 \text{ s}$	SR_{me} :	$1.24 \times 10^{-04} \text{ 1/m}$

Table 8.5: Evaluation of fluorobenzene as a fluorescence tracer in wind-wave tank experiments.

measured signal SR_{me} is two orders of magnitude below the calculated expected signal SR_{ex} . A possible reason for this deviation is the fact that fluorobenzene fluorescence is located in the deep UV range, where the transmission of the involved optics, despite all of them being UV optics, is lower than in the visible range of the spectrum. Especially the Borofloat window of the wind-wave tank has a very low transmission of only 10% at a wavelength of 275 nm, the peak of fluorobenzene fluorescence.

8.3.6 Boundary Layer Visualization

Figure 8.8 shows the course of the fluorobenzene measurement. The decrease of the measured absorbance and the fluorescence signal was used to calculate the transfer velocity by fitting an exponential decay curve to the data. Due to the very low concentration of inserted fluorobenzene, no significant condensation effects were expected at the reflective prisms of the spectrometric setup.

Fluorobenzene			
$u_*: 0.16 \text{ m/s}$			
c_{bulk} :	$5.42 \times 10^{-06} \text{ mol/l}$	Boundary layer:	$28.7 \pm 0.2 \text{ mm}$
c_{surf} :	$2.74 \times 10^{-06} \text{ mol/l}$	Diffusion:	$0.10 \text{ cm}^2/\text{s}$
$c_{\text{surf}}/c_{\text{bulk}}$:	0.51	$k_{\text{a, profile}}$:	$122 \pm 1.1 \text{ cm/h}$
Solubility α :	3.9	$k_{\text{total, bulk}}$:	$24 \pm 0.0 \text{ cm/h}$
Calibration:	$3.06 \times 10^{-09} \text{ mol/l [DN]}$	$k_{\text{total, spec}}$:	$102 \pm 0.1 \text{ cm/h}$

Table 8.6: Results of fluorobenzene mass transfer measurements.

Looking at the results in table 8.6, the transfer velocity determined using the bulk fluorescence data is significantly lower than that of the spectroscopic data. So far, no explanation for this behavior has been found.

The measured profile (8.9) is surprising as the low solubility suggests a constant concentration profile on the air-side. The very low solubility of fluorobenzene should also lessen the effect of water-side fluorescence, but the effect does not seem weaker than with acetone.

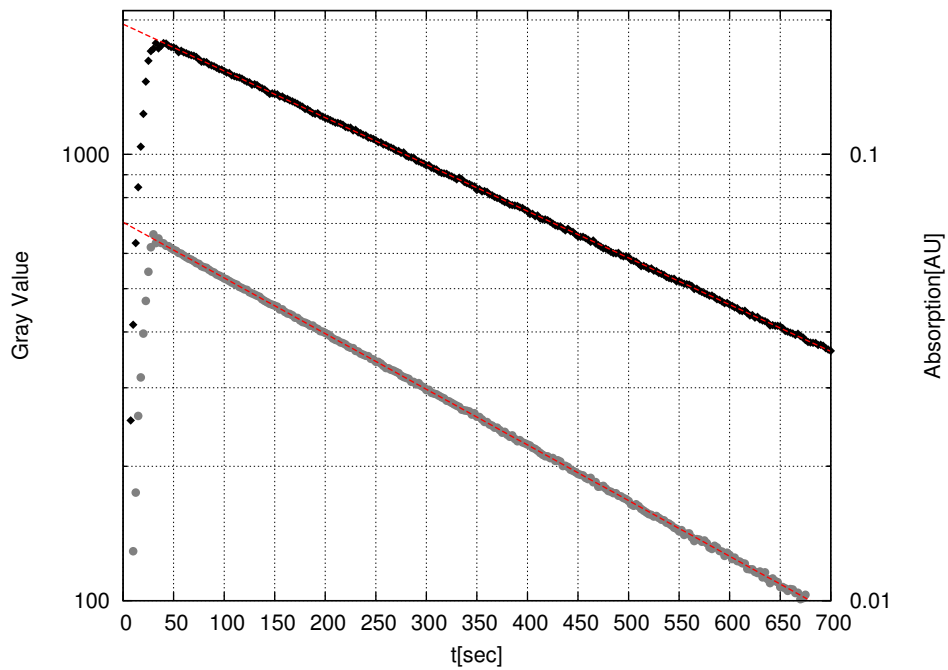


Figure 8.8: Sequential development of the fluorescence signal strength in the bulk (black squares) and the absorption measured by the spectrometer (gray circles) over time

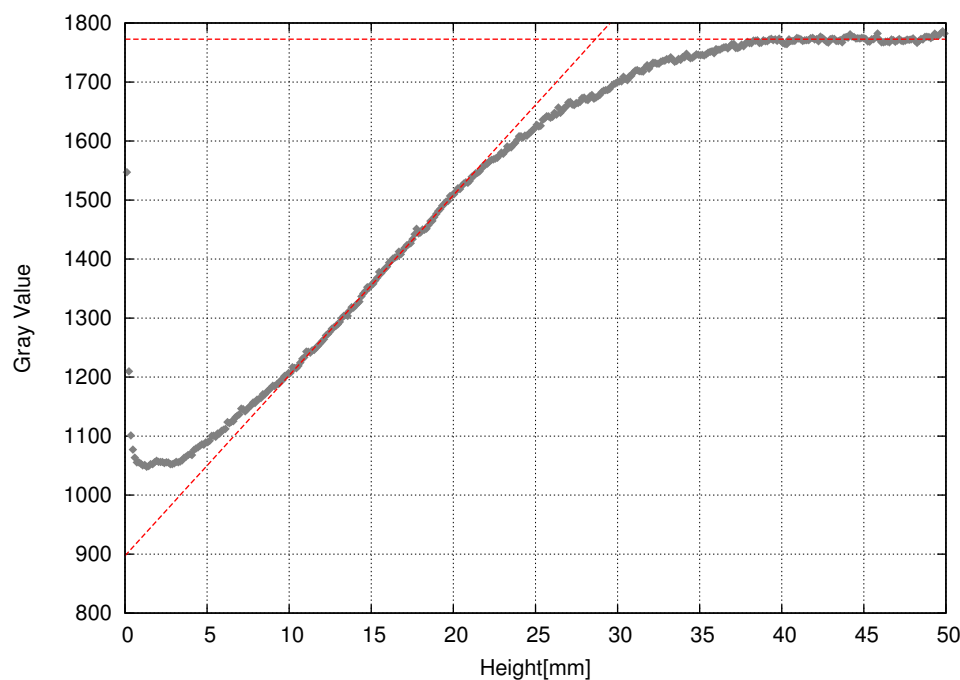


Figure 8.9: Concentration profile with fitted straight lines to evaluate the constant bulk concentration and the linear profile at the surface.

8.4 1,4-Difluorobenzene

1,4-Difluorobenzene (also called p-Difluorobenzene) consists of two fluorine atoms bound on opposite sides of a phenyl ring. Its molecular formula is $C_6H_4F_2$, the structural formula is shown in figure 8.10. Although 1,4-difluorobenzene is a highly efficient fluorescence tracer, no previous flow measurement studies using the substance have been reported.

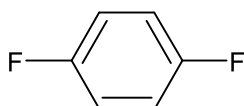


Figure 8.10: 1,4-Difluorobenzene structural formula.

8.4.1 Physical Properties

1,4-Difluorobenzene is a transparent, flammable liquid. Its melting point is $-13\text{ }^\circ\text{C}$, the highest of the three difluorobenzene isomers due to its high symmetry. Its boiling point is $87\text{ }^\circ\text{C}$. 1,4-difluorobenzene has a molecular weight of 114.10 g/mol and a density of

1.17 g/cm³ at normal conditions. Vapor pressure data for 1,4-difluorobenzene was found in Osborn and Scott [53]. The data is available only for a temperature of 25°C, all calculations were done assuming this temperature. At 25 °C, 1,4-difluorobenzene has a vapor pressure of 9.6 mBar. With a solubility $\alpha = 3.2$ [77], 1,4-difluorobenzene is the tracer with the lowest solubility in this study. Its diffusion coefficient is 0.06 cm²/s [78].

8.4.2 Optical Properties

1,4-Difluorobenzene vapor fluorescence has not been studied before. Available measurements of its fluorescence quantum yield and absorption spectra are above all concerned with its chemical properties. It has been used in absorption spectroscopy measurements at the Aeolotron wind-wave tank in Heidelberg, though [23]. The possibility to compare results with those measurements was one of the decisive reasons to choose the tracer, together with its extraordinary high efficiency as a fluorescent substance.

Absorption The absorption spectrum of 1,4-difluorobenzene has a maximum at 271 nm, with an absorption cross section σ of 3.94×10^{-17} cm². At the excitation wavelength of 266 nm, the absorption cross section is 1.28×10^{-17} cm² [69]. The absorption spectrum is strongly jagged, with extreme peaks, rendering simple absorption spectroscopy, as applied here, difficult. As mentioned in chapter 4 the spectrum of the lamp and the transmission of the used fibers can change. For tracers with pronounced peaks, one such peak might drift into or out of the observed wavelength section, thus modifying the result.

Luminescence As mentioned before, 1,4-difluorobenzene is an efficient volatile tracer. Its fluorescence quantum yield is 0.43 [69], the highest of any tracer in this study. Combined with the high absorption cross section (see above), the high efficiency made it necessary to lower the camera gain in measurements. The fluorescence life-time of 1,4-difluorobenzene is 10 ns when excited with a 266 nm light source.

8.4.3 Safety and Health Considerations

1,4-Difluorobenzene may cause irritation to the eyes and respiratory system and its vapor is considered flammable. No information about more precise investigations of the health effects of this substance could be found.

8.4.4 Measurement Parameters

Laser Excitation Limit Using the fluorescence life-time of 1,4-difluorobenzene of 1.7 ns, the excitation limit was determined to be 1.57×10^{25} photons/cm² s. This is below the estimated photon density of the laser sheet of 3.72×10^{25} photons/cm² s.

Concentration Limit Using the equations given in section 5.3.2, the maximum concentration of 1,4-difluorobenzene vapor for the use in LIF experiments in an optically thin medium is 2.71×10^{-06} mol/l. This translates to a vapor concentration of 0.70%.

Tracer Injection Using equation 7.7, the amount of liquid 1,4-difluorobenzene to be inserted into the gas bag was determined. At a temperature of 25 °C, the 1,4-difluorobenzene vapor pressure is 9.6 mbar. A molecular mass of 114.09 g/mol and a density of 1.17 g/cm³ translate to 0.04 ml of liquid 1,4-difluorobenzene for one liter of air to be saturated. With a maximum tracer concentration of 2.71×10^{-06} mol/l, a maximum of 1.5l of saturated air can be inserted into the wind-wave channel without risking LIF operation in an optical thick medium. Thus, the 11 tedlar bags were used for the measurements. The content of the bag was inserted into the wind-wave tank within 15 s.

8.4.5 Signal Strength

The results of the evaluation of the 1,4-difluorobenzene fluorescence signal are shown in table 8.7. As mentioned before, the camera gain had to be lowered to a gain of 5 in order to measure the signal without saturation effects.

1,4-Difluorobenzene			
ρ_{\max} :	1.63×10^{20} 1/m ³	Fluor. Yield Φ_f :	0.43
ρ_{exp} :	1.06×10^{20} 1/m ³	SR_{\max} :	2.76×10^{-01} 1/m
$\text{Air}_{\text{sat.}}/\text{Air}_{\text{pure}}$:	0.70 %	SR_{ex} :	5.81×10^{-02} 1/m
Sat. Excitation:	1.57×10^{25} N _{ph} /cm ² s	SR_{me} :	9.17×10^{-05} 1/m

Table 8.7: Evaluation of 1,4-difluorobenzene as a fluorescence tracer in wind-wave tank experiments.

The measured and expected signal rating are between one and two orders of magnitude higher than of any other tracer substance studied. The measured SR_{measure} is only 1.3% of the theoretically expected signal SR_{expect} . As previously discussed in the case of fluorobenzene, for tracers with a fluorescence spectrum in the UV range there are significant losses due to the transmission at the wind-wave tank windows.

8.4.6 Boundary Layer Visualization

1,4-Difluorobenzene			
$u_*: 0.12 \text{ m/s}$			
c_{bulk} :	$5.64 \times 10^{-06} \text{ mol/l}$	Boundary layer:	$28.9 \pm 0.2 \text{ mm}$
c_{surf} :	$2.54 \times 10^{-06} \text{ mol/l}$	Diffusion:	$0.06 \text{ cm}^2/\text{s}$
$c_{\text{surf}}/c_{\text{bulk}}$:	0.45	$k_{\text{a, profile}}$:	$72 \pm 0.4 \text{ cm/h}$
Solubility α :	3.2	$k_{\text{total, bulk}}$:	$85 \pm 0.1 \text{ cm/h}$
Calibration:	$5.51 \times 10^{-09} \text{ mol/l [DN]}$	$k_{\text{total, spec}}$:	$106 \pm 0.1 \text{ cm/h}$

Table 8.8: Results of 1,4-difluorobenzene mass transfer measurements.

Figure 8.11 shows the course of the conducted transfer measurements. At $t=0 \text{ s}$, saturated 1l saturated air vapor mixture were injected into the wind wave tank over a duration of 15s. Afterwards, the concentration decreases as 1,4-difluorobenzene accumulates in the water and is flushed out of the system via the exhaust air. Fitting a simple box model to the exponential decreases of the two data sets results in the transfer velocities $k_{\text{a,bulk}}$ and $k_{\text{a,spec}}$, shown in table 8.2 for the LIF and spectroscopic data, respectively. The transfer velocity calculated from the spectroscopic data is higher than the one calculated from the bulk fluorescence.

Figure 8.12 shows the concentration profile at $t=27.5 \text{ s}$. The general shape of the profile is as expected, showing a constant intensity at the upper end, the bulk, and a linear decrease near the water surface. Immediately above the water surface, the gray value increases rapidly. With a solubility of $\alpha = 3.2$, an increase of up to three times the estimated value at the surface would be expected. While not shown in the plot, the highest gray value registered at the water surface is 1542 [DN]. α times the estimated surface gray value of 460 [DN] would result in a gray value of 1472 [DN], consistent with the assumption of the measured linear profile to be part of the linear decrease.

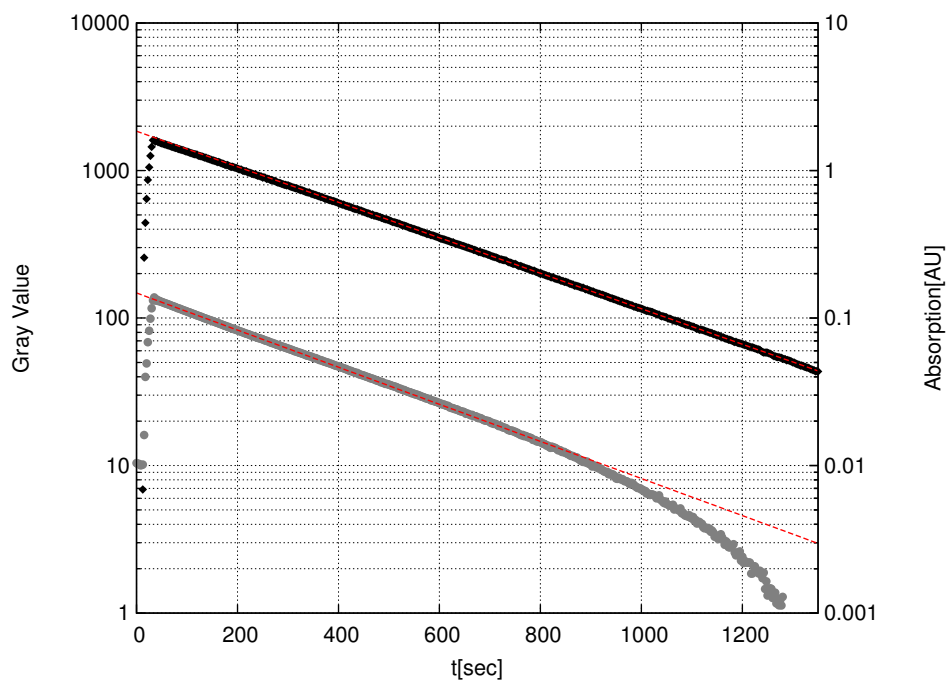


Figure 8.11: Sequential development of the fluorescence signal strength in the bulk (black squares) and the absorption measured by the spectrometer (gray circles) over time.

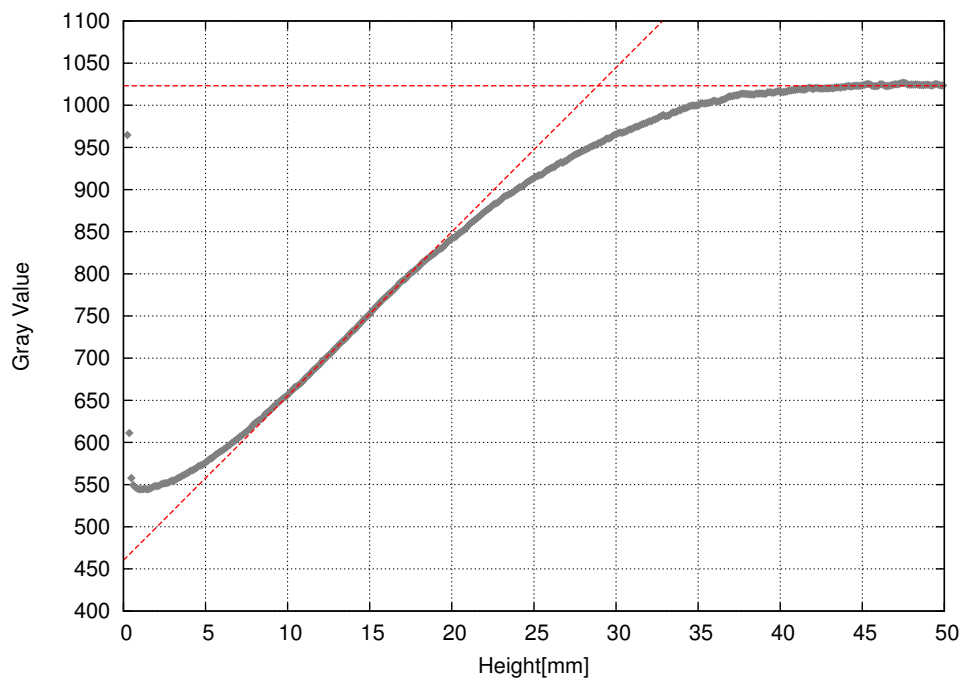


Figure 8.12: Concentration profile with fitted lines to evaluate the constant bulk concentration and the linear profile at the surface. Up to approximately 6 mm height, fluorescence generated in the water interferes with the measurement.

8.5 Anisole

Anisole (IUPAC name: methoxybenzene) is an aromatic compound, consisting of a phenyl ring structure (C_6H_5) with an attached methoxy group ($O-CH_3$). Its molecular formula is C_7H_8O , the structural formula is shown in figure 8.13. Anisole was chosen for this study because it showed well measurable fluorescence in the preliminary setup and it has been used in other gas exchange experiments at the Heidelberg Aeolotron wind-wave tank, making comparisons with the results of established measurements possible.

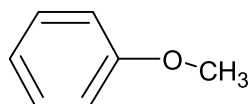


Figure 8.13: The structural formula of anisole.

8.5.1 Physical Properties

Anisole is a colorless, flammable liquid with a strong odor reminiscent of anise seed. It is commonly used in artificial fragrances. At a temperature of $52^{\circ}C$, anisole vapor can create an explosive mixture with air, while at lower temperatures there is no such risk. Its boiling point is $155^{\circ}C$ and its melting point is $-37^{\circ}C$.

Anisole has a molecular weight of 108.14 g/mol and a density of 0.788 g/cm^3 . Its vapor pressure at laboratory temperature $22.3^{\circ}C$ is 4.7 mBar . At a temperature of $25^{\circ}C$, its vapor pressure is 3.9 mBar [4]. The air water partition coefficient α of anisole is $\alpha = 5.9$ [43] and its diffusion coefficient is $0.07\text{ cm}^2/\text{s}$.

8.5.2 Optical Properties

No flow visualization experiments could be found during the research for this study. Anisole has previously been used as substance in absorption spectroscopy transfer measurements [68]

Absorption The absorption spectrum of anisole in the UV region reaches from 250 nm to 285 nm with an absorption maximum σ of $7.38 \times 10^{-18}\text{ cm}^2$ at a wavelength of 271 nm . As with other molecules with an aromatic ring structure, the spectrum has several distinct peaks [2].

Luminescence Anisole's fluorescence spectrum stretches from 280 nm to 350 nm with a maximum fluorescence at 289 nm. The fluorescence quantum yield η of anisole is reported to be 0.29[2]. The slight overlap between absorption and fluorescence spectrum can cause self-excitation and the low redshift makes the use of UV optics necessary for the detection. The fluorescence life-time of anisole is 8.3 ns.

8.5.3 Safety and Health Considerations

Anisole is generally considered only mildly toxic. Its vapor can cause a sore throat and is irritating to the eyes and skin. At a temperature of 52°C, anisole partial pressure reaches a level where the air vapor mixture becomes a flammable gas.

8.5.4 Measurement Parameters

Laser Excitation Limit With a fluorescence life-time of 8.3 ns and an absorption cross section σ of $7.38 \times 10^{-18} \text{ cm}^2$, the excitation limit for anisole was calculated to be $1.63 \times 10^{25} \text{ photons/cm}^2 \text{ s}$. The peak irradiance of the CRF 266 laser system is $3.72 \times 10^{25} \text{ photons/cm}^2 \text{ s}$, above this limit. Using the CRF 266 laser system at full output power, the excitation cannot be considered weak.

Concentration Limit Using the equations given in 5.3.2, anisole's absorption cross section σ of $7.38 \times 10^{-18} \text{ cm}^2$ translates to a maximum concentration of $4.69 \times 10^{-6} \text{ mol/l}$ or 2.46% before the tracer air mixture has to be considered optically thick.

Tracer Injection The amount of liquid anisole to be inserted into the gas bag was determined using equation 7.7. At the laboratory temperature during the experiment of 22.3°C, the anisole vapor pressure was 4.7 mbar translating to 0.02 ml of liquid anisole to be inserted per liter of gas bag volume. Considering the maximum concentration of $4.69 \times 10^{-6} \text{ mol/l}$, a maximum of 5.4 l of air saturated with anisole vapor can be inserted into the wind-wave tank before an optically thick medium is created. As the preliminary measurement provided a qualitative impression of anisole's strong fluorescence signal, a 1 l gas bag was considered sufficient for the measurements in the wind-wave tank.

The flow controller used to inject the saturated air into the wind-wave tank allows for a maximum air flow of 4 l/min. 1 l of tracer saturated air were injected into the wind wave channel over a period of 15 s.

8.5.5 Signal Strength

Table 8.3 shows the results of the anisole vapor fluorescence measurements. Anisole proves to be a well detectable tracer substance.

Anisole			
ρ_{\max} :	$2.82 \times 10^{20} \text{ 1/m}^3$	Fluor. Yield Φ_f :	0.29
ρ_{exp} :	$4.33 \times 10^{19} \text{ 1/m}^3$	SR_{\max} :	$6.04 \times 10^{-02} \text{ 1/m}$
$\text{Air}_{\text{sat.}}/\text{Air}_{\text{pure}}$:	2.46 %	SR_{ex} :	$9.27 \times 10^{-03} \text{ 1/m}$
Sat. Excitation:	$1.63 \times 10^{25} \text{ N}_{\text{ph}}/\text{cm}^2 \text{ s}$	SR_{me} :	$5.07 \times 10^{-05} \text{ 1/m}$

Table 8.9: Evaluation of anisole as a fluorescence tracer in wind-wave tank experiments.

Comparing the measured signal SR_{me} to the calculated expected signal SR_{ex} shows a loss of nearly two orders of magnitude. With anisole's fluorescence spectrum being in the same range as that of fluorobenzene and 1,4-difluorobenzene the similarity in results does not surprise. The assumption that this is caused by the transmission characteristics of the optical path between fluorescent light sheet and camera sensor seems plausible. It remains important to note, though, that the measured fluorescence is still above that of acetone despite the fact that five times the amount of anisole could be inserted into the wind-wave tank before problems due to optical thickness arise.

8.5.6 Boundary Layer Visualization

The course of the mass transfer measurements of anisole is shown in figure 8.14.

Anisole			
$u_*: 0.17 \text{ m/s}$			
c_{bulk} :	$1.94 \times 10^{-06} \text{ mol/l}$	Boundary layer:	$26.8 \pm 0.3 \text{ mm}$
c_{surf} :	$8.14 \times 10^{-07} \text{ mol/l}$	Diffusion:	$0.07 \text{ cm}^2/\text{s}$
$c_{\text{surf}}/c_{\text{bulk}}$:	0.42	$k_{a, \text{profile}}$:	$98 \pm 1.1 \text{ cm/h}$
Solubility α :	5.9	$k_{\text{total, bulk}}$:	$103 \pm 0.6 \text{ cm/h}$
Calibration:	$3.04 \times 10^{-09} \text{ mol/l [DN]}$	$k_{\text{total, spec}}$:	$448 \pm 1.9 \text{ cm/h}$

Table 8.10: Results of anisole mass transfer measurements.

A gas bag filled with 1 l a saturated mixture of anisole vapor and air was emptied into the wind-wave tank over the course of 15 s. The decrease of the measured absorbance and the fluorescence signal was used to calculate the transfer velocity. Due to the low anisole concentration in the experiment, condensation effects on the spectroscopic

measurements are unlikely. A comparison of the results in table 8.10 shows that the transfer velocity measured via the spectrometer is actually higher than that measured via the bulk fluorescence.

A look at the measured profile (8.15) reveals a result typical for this study. The profile shows the rise in intensity near the water surface up to a height of 10 mm. A linear rise in between 10 mm and 20 mm above the surface and a constant concentration in the bulk.

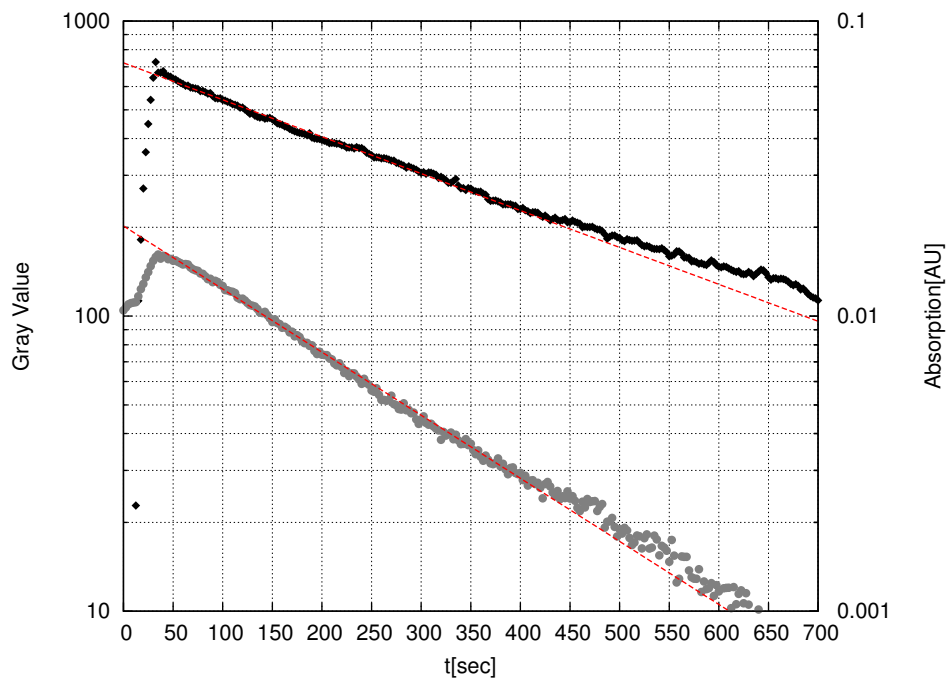


Figure 8.14: Sequential development of the fluorescence signal strength in the bulk (black squares) and the absorption measured by the spectrometer (gray circles) over time

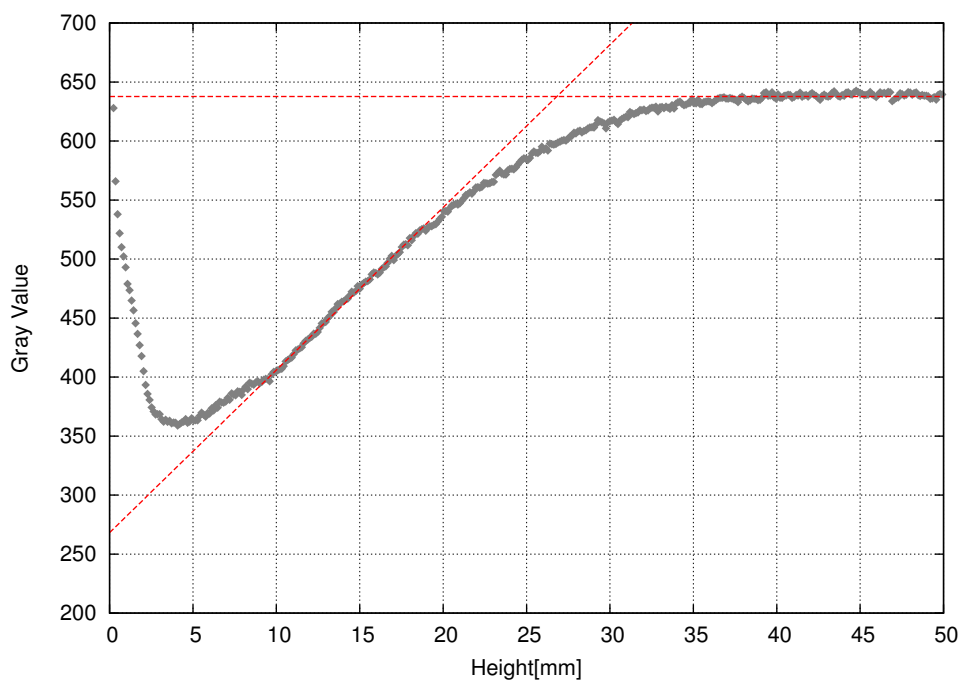


Figure 8.15: Concentration profile with fitted straight lines to evaluate the constant bulk concentration and the linear profile at the surface.

8.6 4-Fluoroanisole

4-Fluoroanisole (IUPAC: 1-fluoro-4-methoxybenzene), another halogenated aromatic compound, was chosen for this study because it combines the characteristics of anisole and fluorobenzene, two substances that had proven to be efficient fluorescent tracers. 4-Fluoroanisole consists of a phenyl ring (C_6H_5) with an attached fluorine atom ($-F$) and a methoxy group ($O-CH_3$). Its molecular formula is C_7H_7FO . The structural formula is shown in figure 8.16.

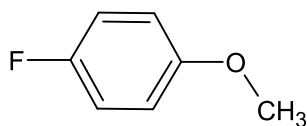


Figure 8.16: The structural formula of 4-fluoroanisole. A fluorine atom and a methoxy group are bound to a phenyl ring.

8.6.1 Physical Properties

4-Fluoroanisole is a colorless, flammable liquid. Its boiling point is 158° C and its melting point is -45° C. 4-Fluoroanisole has a molecular weight of 96.10 g/mol and a density of 1.11 g/cm³. Being a synthetic compound not occurring in nature, only sparse data is available about 4-fluoroanisole. No information about its vapor pressure or solubility was available. The substance was nevertheless measured encouraged by the good results obtained with the similar molecules anisole and fluorobenzene.

8.6.2 Optical Properties

No previous use of 4-fluoroanisole in LIF measurements has been reported. The data available has been taken from a study concerned with the reaction rates of the ground electronic state [2].

Absorption 4-fluoroanisole has an absorption maximum at a wavelength 281 nm with an absorption cross section σ of 1.11×10^{-17} cm²[2], higher than the absorption of both anisole and fluorobenzene, but lower than that of 1,4-difluorobenzene. No absorption spectra were available, but using the spectral information gathered during the experiments, the absorption cross section at the excitation wavelength of 266 nm has been estimated to be 9.25×10^{-18} cm².

Luminescence The fluorescence quantum yield η of 4-fluoroanisole is 0.18, i.e. higher than that of fluorobenzene but lower than that of anisole. The fluorescence spectrum of 4-fluoroanisole is not known and could not be measured in this study. It can be assumed to be similar to that of anisole and fluorobenzene, with a weaker redshift and a slight overlap of absorption and fluorescent spectrum. The fluorescence life-time of 4-fluoroanisole's excited singlet state is 3.86 ns [2].

8.6.3 Safety and Health Considerations

Safety and health information of 4-fluoroanisole is sparse. It is known to be a flammable liquid. Contact with skin or eyes can cause irritation. No other data is available at present.

8.6.4 Measurement Parameters

Laser Excitation Limit With a fluorescence life-time of 3.86 ns and an absorption cross section σ of $9.25 \times 10^{-18} \text{ cm}^2$, the excitation limit for 4-fluoroanisole was calculated to be $2.80 \times 10^{25} \text{ photons/cm}^2 \text{ s}$. The peak irradiance of the CRF 266 laser system is $3.72 \times 10^{25} \text{ photons/cm}^2 \text{ s}$.

Concentration Limit Using the equations given in section 5.3.2, the maximum concentration of 4-fluoroanisole vapor for the use in LIF experiments in an optically thin medium is $3.74 \times 10^{-06} \text{ mol/l}$. Without available information about the vapor pressure, it is not possible to calculate the actual amount of vapor this corresponds to.

Tracer Injection Due to the high fluorescence quantum yield and absorption cross section, 4-fluoroanisole was injected using a 1 l tedlar bag. 0.1 ml of 4-fluoroanisole were injected into the bag before the measurement started. The flow controller used to inject the saturated air into the wind-wave tank allows for a maximum air flow of 4 l/min. The content of the gas bag was emptied into the wind-wave tank in a period of 15 s.

8.6.5 Signal Strength

Table 8.11 shows the results of the 4-fluoroanisole vapor fluorescence measurements. Due to the missing vapor pressure data, no expected signal could be calculated. The

4-Fluoroanisole			
ρ_{max} :	$2.25 \times 10^{20} \text{ 1/m}^3$	Fluor. Yield Φ_f :	0.18
ρ_{exp} :	n.a.	SR_{max} :	$4.49 \times 10^{-02} \text{ 1/m}$
$\text{Air}_{\text{sat.}}/\text{Air}_{\text{pure}}$:	n.a.	SR_{ex} :	n.a.
Sat. Excitation:	$2.80 \times 10^{25} \text{ N}_{\text{ph}}/\text{cm}^2 \text{ s}$	SR_{me} :	$1.10 \times 10^{-04} \text{ 1/m}$

Table 8.11: Evaluation of 4-fluoroanisole as a fluorescence tracer in wind-wave tank experiments.

measured signal SR_{me} is about two times as strong as that of anisole and about 90% as strong as that of fluorobenzene.

8.6.6 Boundary Layer Visualization

Figure 8.17 shows the course of the 4-fluoroanisole measurement. The content of a 1 l gas bag filled with saturated mixture of 4-fluoroanisole vapor and air was emptied into the wind wave tank over a period of 15 s. The decrease of the measured absorbance and the

fluorescence signal was used to calculate the transfer velocity by fitting an exponential decay curve to the data. As with the other substances based on an aromatic ring, the spectral data decrease much faster than the bulk fluorescence signal indicating a possible systematic error introduced by the simple single line spectroscopic measurement.

4-Fluoroanisole			
$u_*: 0.12 \text{ m/s}$			
$c_{\text{bulk}}:$	$1.11 \times 10^{-07} \text{ mol/l}$	Boundary layer:	$28.9 \pm 0.3 \text{ mm}$
$c_{\text{surf}}:$	$4.94 \times 10^{-08} \text{ mol/l}$	Diffusion:	n.a.
$c_{\text{surf}}/c_{\text{bulk}}:$	0.44	$k_{a, \text{ profile}}:$	n.a.
Solubility $\alpha:$	n.a.	$k_{\text{total, bulk}}:$	$156 \pm 0.5 \text{ cm/h}$
Calibration:	$7.20 \times 10^{-11} \text{ mol/l [DN]}$	$k_{\text{total, spec}}:$	$386 \pm 3.7 \text{ cm/h}$

Table 8.12: Results of 4-fluoroanisole mass transfer measurements.

A profile could be measured without any difficulty, given the high signal strength (8.18), but without a diffusion constant, the transfer velocity cannot be calculated from it. The typical rise in gray value near the water surface can also be seen in this measurement.

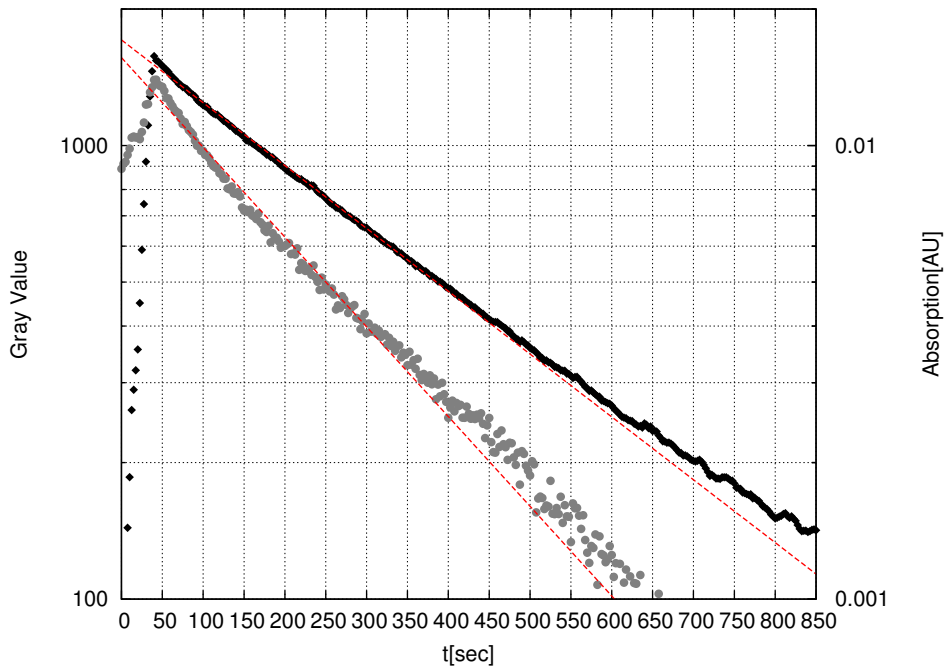


Figure 8.17: Sequential development of the fluorescence signal strength in the bulk (black squares) and the absorption measured by the spectrometer (gray circles) over time

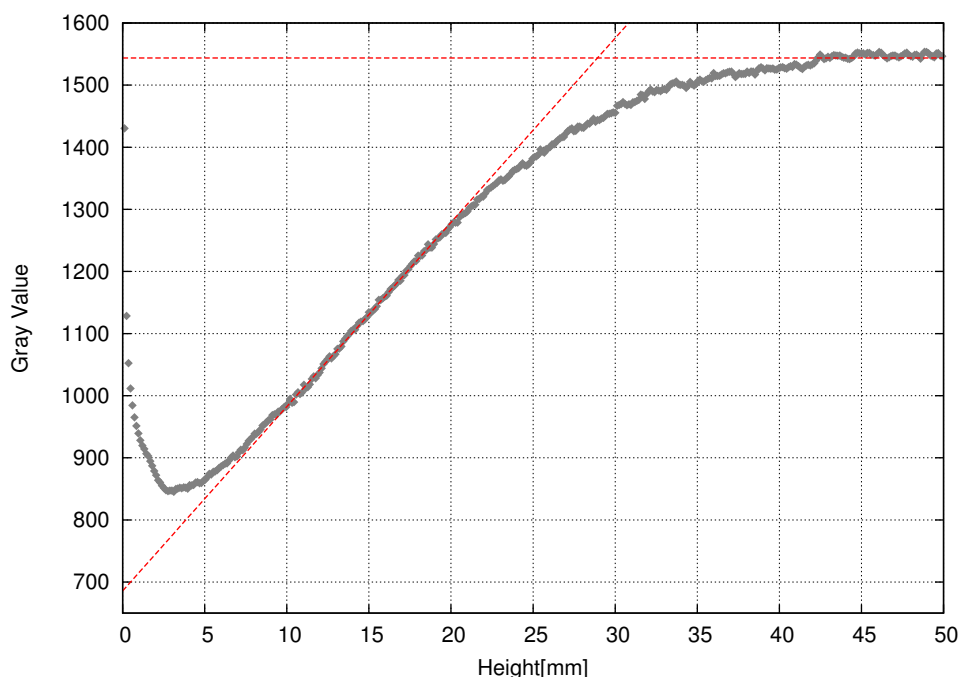


Figure 8.18: Concentration profile with fitted straight lines to evaluate the constant bulk concentration and the linear profile at the surface.

8.7 4-Methylanisole

4-Methylanisole was chosen as a possible fluorescent tracer for the same reason as 4-fluoroanisole. It has a structure similar to that of anisole, which had proven to be an efficient tracer in preliminary measurements. 4-Methylanisole consists of a phenyl ring (C_6H_5) and a methoxy group ($O-CH_3$) and a methyl group (CH_3), bound on opposite sides. Its molecular formula is $C_8H_{10}O$, its structural formula is shown in figure 8.19.

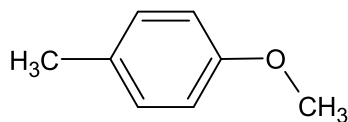


Figure 8.19: 4-Methylanisole structural formula.

8.7.1 Physical Properties

4-Methylanisole is a transparent, slightly yellowish, flammable liquid. Its boiling point is $174^\circ C$ and its melting point is $-50^\circ C$. It has a molecular weight of 122.17 g/mol and

a density of 0.96 g/cm^3 . No vapor pressure or solubility data for this compound were available, creating the same difficulties discussed for 4-fluoroanisole before.

8.7.2 Optical Properties

No previous studies using 4-methylanisole in LIF measurements have been found. The data available have been taken from a study concerned with the reaction rates of the ground electronic state [2].

Absorption 4-methylanisole has an absorption maximum at a wavelength of 279 nm with an absorption cross section σ of $1.11 \times 10^{-17} \text{ cm}^2$ [2]. This is slightly higher than the absorption of anisole. No absorption spectra were available, but using the spectral information gathered during the experiments, the absorption cross section at the excitation wavelength of 266 nm has been estimated to be $6.51 \times 10^{-18} \text{ cm}^2$.

Luminescence The reported fluorescence quantum yield η of 4-methylanisole is 0.33. The second highest fluorescence quantum yield in this study. The fluorescence spectrum of 4-methylanisole is not known and could not be measured in this study. It can be assumed to be similar to that of anisole and fluorobenzene, with a relatively minor redshift and a slight overlap of the absorption and fluorescence spectrum. The fluorescence life-time of 4-fluoroanisole's excited singlet state is 7.48 ns [2].

8.7.3 Safety and Health Considerations

4-Methylanisole is a flammable liquid. Inhalation can cause irritation of the respiratory system and contact with skin or eyes can cause irritation. No other data is available at present.

8.7.4 Measurement Parameters

Laser Excitation Limit With a fluorescence life-time of 7.48 ns and an absorption cross section σ of $9.25 \times 10^{-18} \text{ cm}^2$, the excitation limit for 4-methylanisole was calculated to be $2.05 \times 10^{25} \text{ photons/cm}^2 \text{ s}$. The peak irradiance of the CRF 266 laser system is $3.72 \times 10^{25} \text{ photons/cm}^2 \text{ s}$.

Concentration Limit Using the equations given in section 5.3.2, the maximum concentration of 4-methylanisole vapor for the use in LIF experiments in an optically thin medium is $5.32 \times 10^{-6} \text{ mol/l}$. Without available information about the vapor pressure, it is not possible to calculate the actual amount of vapor this corresponds to.

Tracer Injection Due to the high fluorescence quantum yield and absorption cross section, 4-methylanisole was injected using a 1 l tedlar bag. 0.1 ml of 4-methylanisole were injected into the bag before the measurement started. The flow controller used to inject the saturated air into the wind-wave tank allows for a maximum air flow of 4 l/min. The content of the gas bag was emptied into the wind-wave tank in a period of 15 s.

8.7.5 Signal Strength

Table 8.13 shows the results of the 4-methylanisole vapor fluorescence measurements.

4-Methylanisole			
ρ_{\max} :	$3.20 \times 10^{20} \text{ 1/m}^3$	Fluor. Yield Φ_f :	0.33
ρ_{exp} :	n.a.	SR_{\max} :	$8.77 \times 10^{-02} \text{ 1/m}$
$\text{Air}_{\text{sat.}}/\text{Air}_{\text{pure}}$:	n.a.	SR_{ex} :	n.a.
Sat. Excitation:	$2.05 \times 10^{25} \text{ N}_{\text{ph}}/\text{cm}^2 \text{ s}$	SR_{me} :	$1.24 \times 10^{-05} \text{ 1/m}$

Table 8.13: Evaluation of 4-methylanisole as a fluorescence tracer in wind-wave tank experiments.

These results are rather surprising. The maximum signal SR_{\max} , calculated from available information about 4-methylanisole fluorescent quantum yield and absorption characteristics, is the second highest of any tracer studied. The measurement results differ dramatically. The measured signal strength SR_{\max} is undercut only by that of ethanal and 2-methylphenol. No vapor pressure data was available, making it impossible to calculate an expected signal SR_{ex} .

A possible explanation for this result could be a lower redshift in the fluorescence spectrum than for any other organic compound, resulting in a very strong absorption along the optical path between laser sheet and camera as can be seen in figure 6.4.

8.7.6 Boundary Layer Visualization

Figure 8.20 shows the course of the 4-methylanisole measurement. The content of a 1 l gas bag filled with saturated mixture of 4-methylanisole vapor and air was emptied into the wind wave tank over a period of 15 s. The decrease of the measured absorbance and the fluorescence signal was used to calculate the transfer velocity by fitting an exponential decay curve to the data. In contrast to most other aromatic substances used, there is no large difference in the decrease of the concentration as measured via the bulk fluorescence and the spectrometer.

4-Methylanisole			
$u_*: 0.12 \text{ m/s}$			
$c_{\text{bulk}}:$	$2.23 \times 10^{-06} \text{ mol/l}$	Boundary layer:	$26.1 \pm 0.9 \text{ mm}$
$c_{\text{surf}}:$	$1.56 \times 10^{-06} \text{ mol/l}$	Diffusion:	n.a.
$c_{\text{surf}}/c_{\text{bulk}}:$	0.70	$k_{a, \text{ profile}}:$	n.a.
Solubility $\alpha:$	n.a.	$k_{\text{total, bulk}}:$	$340 \pm 3.3 \text{ cm/h}$
Calibration:	$1.37 \times 10^{-08} \text{ mol/l [DN]}$	$k_{\text{total, spec}}:$	$324 \pm 2.0 \text{ cm/h}$

Table 8.14: Results of 4-methylanisole mass transfer measurements.

Due to the low signal strength, the profile of 4-methylanisole (8.21) appears to be noisy. As in previous measurements, a rise in signal intensity near the water surface could be observed that render all information up to 10 mm above the water surface unusable. Due to the lack of information about the diffusion constant of 4-methylanisole, no transfer velocity could be obtained from the measurement.

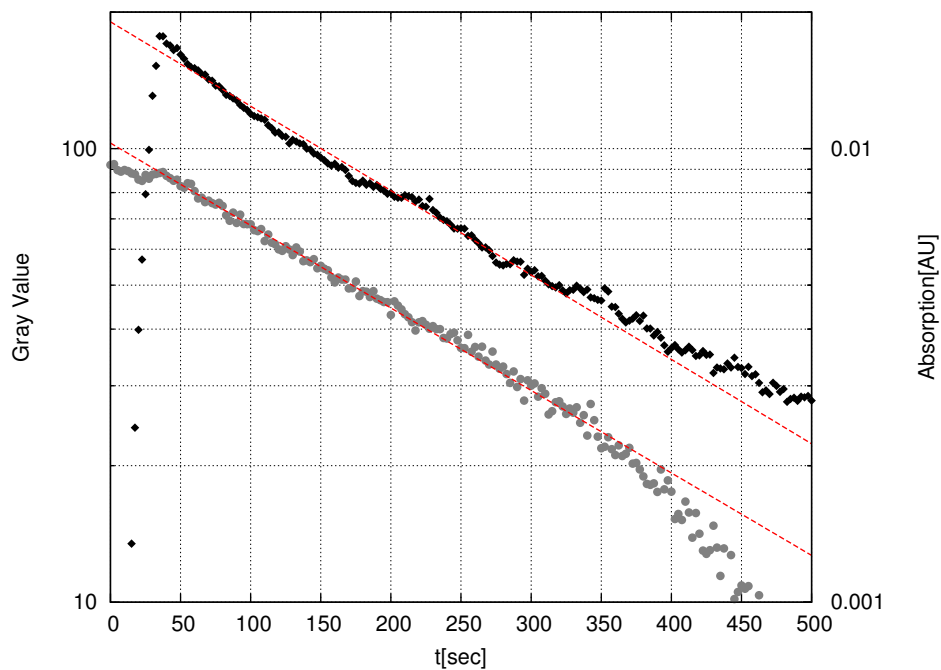


Figure 8.20: Sequential development of the fluorescence signal strength in the bulk (black squares) and the absorption measured by the spectrometer (gray circles) over time

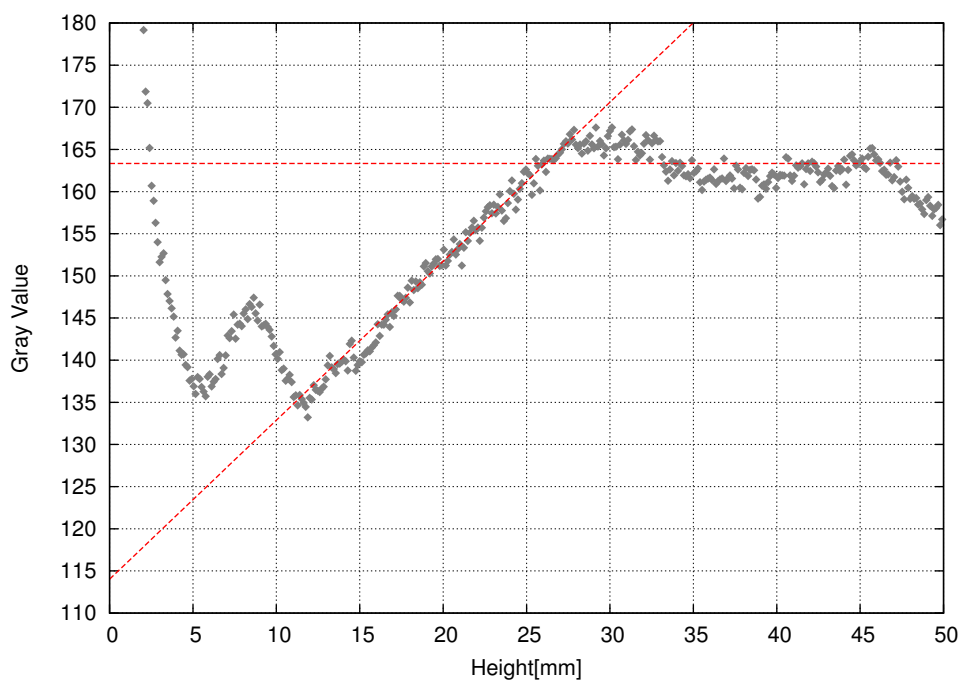


Figure 8.21: Concentration profile with fitted straight lines to evaluate the constant bulk concentration and the linear profile at the surface.

8.8 2,4-Difluoroanisole

2,4-Difluoroanisole (IUPAC: 2,4-Difluor-1-methoxybenzene) is another halogenated aromatic compound studied. Similar to fluoroanisole, it is composed of a phenyl ring (C_6H_5) attached to a methoxy group ($O-CH_3$) and two fluorine atoms. Its molecular formula is $C_7H_6F_2O$, the structural formula is shown in figure 8.22. Only the most basic information are available about this synthetic molecule. It was chosen for this study due to the extraordinary performance of 1,4-difluorobenzene as a fluorescent tracer, which has a similar structure.

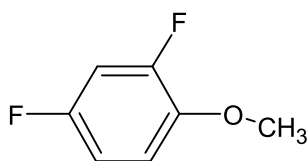


Figure 8.22: The structural formula of 2,4-difluoroanisole.

8.8.1 Physical Properties

2,4-Difluoroanisole is a flammable, transparent liquid. Its boiling point is 155.8° C. Information on the melting point is not available. 2,4-Difluoroanisole has a molecular weight of 144.11 g/mol and a density of 1.182 g/cm³.

Neither 2,4-difluoroanisole's vapor pressure nor the air-water partitioning coefficient nor its diffusion constant in air are available.

8.8.2 Optical Properties

No information about 2,4-difluoroanisole absorption or luminescence is available at present.

8.8.3 Safety and Health Considerations

2,4-Difluoroanisole is irritating to the eyes, respiratory system and skin. It is considered harmful if swallowed. It is flammable in its liquid state.

8.8.4 Measurement Parameters

Laser Excitation Limit and Concentration Limit Without any information about the absorption cross section, vapor pressure and fluorescence life-time, no excitation and concentration limits could be calculated.

Tracer Injection 2,4-Difluoroanisole was injected using a 1 l tedlar bag. 0.1 ml of the substance were injected into the bag before the measurement started. The flow controller used to inject the saturated air into the wind-wave tank allows for a maximum air flow of 4 l/min. The content of the gas bag was emptied into the wind-wave tank in a period of 15 s.

8.8.5 Signal Strength

The measured signal SR_{me} for 2,4-difluoroanisole was 5.34×10^{-05} 1/m. No other data could be derived from the measurements in terms of signal strength due to the lack of information on optical and physical properties. The measured signal strength is about the same as that of anisole, putting 1,4-difluoroanisole into the category of well detectable tracers.

8.8.6 Boundary Layer Visualization

The course of the mass transfer measurements of 2,4-difluoroanisole is shown in figure 8.23.

2,4-Difluoroanisole			
$u_*: 0.12 \text{ m/s}$			
c_{bulk} :	n.a.	Boundary layer:	$28.5 \pm 0.3 \text{ mm}$
c_{surf} :	n.a.	Diffusion:	n.a.
$c_{\text{surf}}/c_{\text{bulk}}$:	0.54	$k_{\text{a, profile}}$:	n.a.
Solubility α :	n.a.	$k_{\text{total, bulk}}$:	$214 \pm 0.5 \text{ cm/h}$
Calibration:	n.a.	$k_{\text{total, spec}}$:	$243 \pm 1.8 \text{ cm/h}$

Table 8.15: Results of 2,4-difluoroanisole mass transfer measurements.

A gas bag filled with 1 l saturated mixture of anisole vapor and air was emptied into the wind-wave tank over the course of 15 s. The decrease of the measured absorbance and the fluorescence signal was used to calculate the transfer velocity. Without information on 2,4-difluoroanisole's solubility or diffusion constant, a complete evaluation of its mass transfer properties was not possible.

A look at the measured profile (8.24) reveals a result typical for this study. The profile shows the rise in intensity near the water surface up to a height of 10 mm. A linear rise in between 10 mm and 20 mm above the surface and a constant concentration in the bulk.

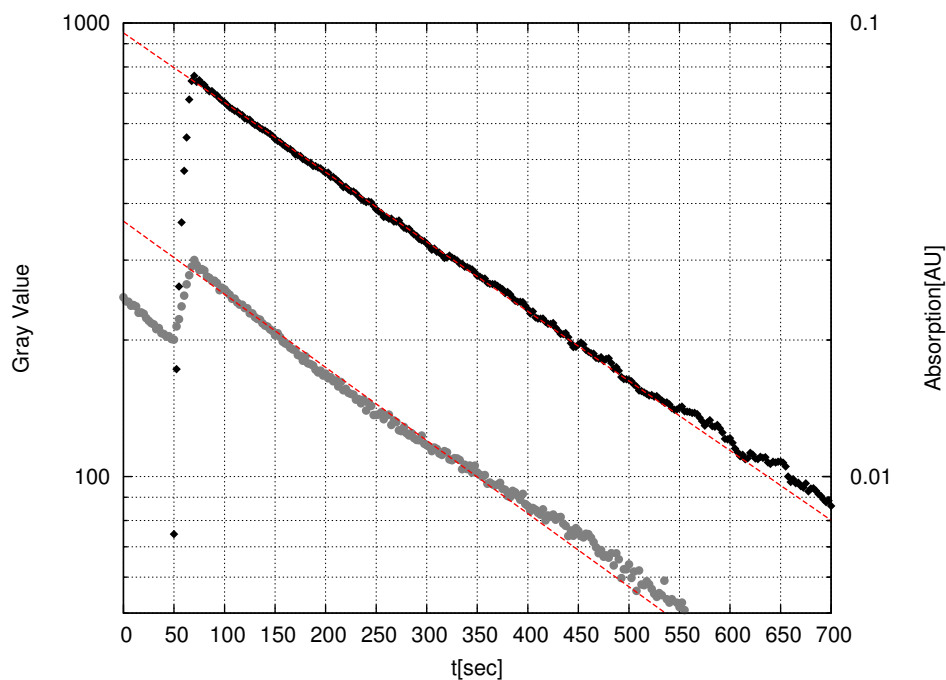


Figure 8.23: Sequential development of the fluorescence signal strength in the bulk (black squares) and the absorption measured by the spectrometer (gray circles) over time

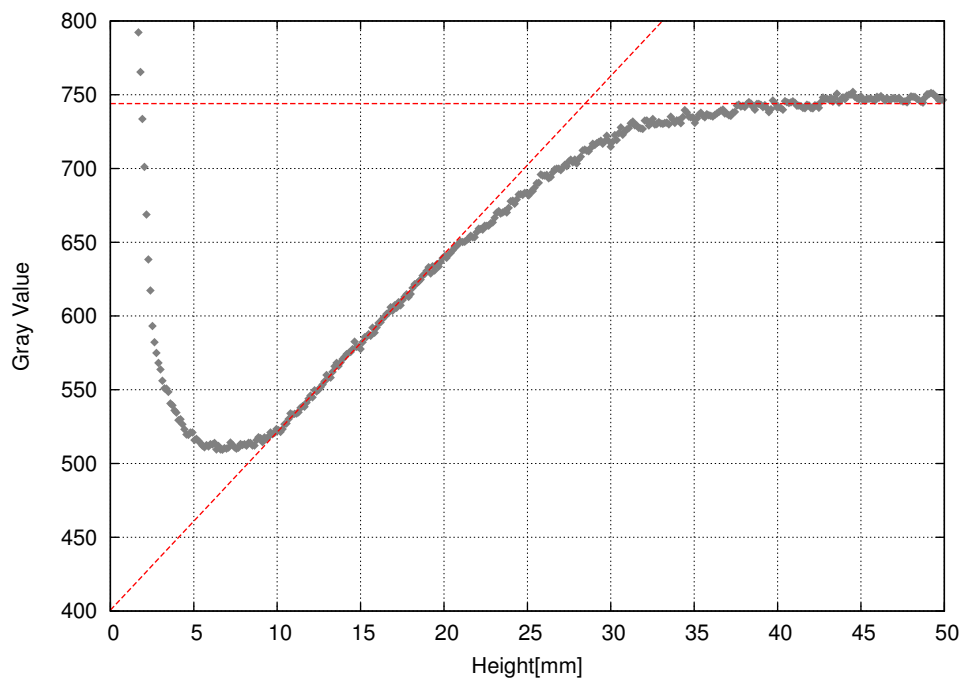


Figure 8.24: Concentration profile with fitted straight lines to evaluate the constant bulk concentration and the linear profile at the surface.

8.9 2-Fluorophenol

Phenols are compounds consisting of an aromatic ring and one or more hydroxyl groups. The simplest molecule in this group, phenol, was not used due to safety considerations. 2-fluorophenol is a halogenated aromatic compound, a single fluorine atom is bound to the phenol structure. Its molecular formula is C_6H_5FO and the structural formula is shown in figure 8.25.

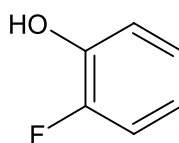


Figure 8.25: The structural formula of 2-fluorophenol.

8.9.1 Physical Properties

2-Fluorophenol is a colorless liquid. Its boiling point is $150^{\circ}C$ and its melting point is $16.1^{\circ}C$. 2-Fluorophenol has a molecular weight of 112.1 g/mol and a density of 1.217 g/cm^3 . Its vapor pressure at $25^{\circ}C$ temperature is 3.813 mBar [43].

The high solubility of phenols is the reason why these substances are of interest for this study. 2-Fluorophenol has an air-water partition coefficient $\alpha = 1819$ [54] higher than that of any non-phenol substance used in this study.

8.9.2 Optical Properties

No previous studies of 2-fluorophenol fluorescence in flow visualization experiments have been found.

Absorption While no 2-fluorophenol absorption spectra were available, Dearden [15] provide a study of the absorption bands of various phenols, among them 2-fluorophenol. It has a maximum absorption cross section σ of $6.12 \times 10^{-18}\text{ cm}^2$ [15] at a wavelength of 266 nm , i.e. the second highest absorption cross section of any tracer in the study.

Luminescence The fluorescence quantum yield of 2-fluorophenol was not known. The very similar phenol is known to have a fluorescence quantum yield of 0.08 which was used for all estimations below. The same assumption was made for the fluorescence life-time, which is assumed to be similar to that of phenol (2.1 ns).

8.9.3 Safety and Health Considerations

No specific information of the health risks posed by 2-fluorophenol was available, the manufacturer classifies the substance as harmful to humans.

8.9.4 Measurement Parameters

Laser Excitation Limit With a supposed fluorescence life-time of 2.1 ns and an absorption cross section σ of $6.12 \times 10^{-18} \text{ cm}^2$, the excitation limit for 2-fluorophenol was calculated to be $7.78 \times 10^{25} \text{ photons/cm}^2 \text{ s}$. The peak irradiance of the CRF 266 laser system is $3.72 \times 10^{25} \text{ photons/cm}^2 \text{ s}$.

Concentration Limit 2-Fluorophenol's absorption cross section σ of $6.12 \times 10^{-18} \text{ cm}^2$ results in a maximum concentration of $5.66 \times 10^{-6} \text{ mol/l}$ or 3.68% before the tracer air mixture has to be considered optically thick.

Tracer Injection 2-Fluorophenol was injected into the wind-wave tank using a 1 l tedlar bag. The amount of liquid 2-fluorophenol to be inserted into the gas bag was determined using equation 7.7. 0.01 ml of liquid tracer was inserted into the gas bag before the experiment. The flow controller used to inject the saturated air into the wind-wave tank allows for a maximum air flow of 41/min. The content of the gas bag was emptied into the wind-wave tank in a period of 15 s.

8.9.5 Signal Strength

Table 8.16 shows the results of the 2-fluorophenol vapor fluorescence measurements. The

2-Fluorophenol			
ρ_{max} :	$3.41 \times 10^{20} \text{ 1/m}^3$	Fluor. Yield Φ_f :	0.08
ρ_{exp} :	$4.21 \times 10^{19} \text{ 1/m}^3$	SR_{max} :	$1.67 \times 10^{-02} \text{ 1/m}$
$\text{Air}_{\text{sat.}}/\text{Air}_{\text{pure}}$:	3.68 %	SR_{ex} :	$2.06 \times 10^{-03} \text{ 1/m}$
Sat. Excitation:	$7.78 \times 10^{25} \text{ N}_{\text{ph}}/\text{cm}^2 \text{ s}$	SR_{me} :	$3.46 \times 10^{-05} \text{ 1/m}$

Table 8.16: Evaluation of 2-fluorophenol as a fluorescence tracer in wind-wave tank experiments.

measured signal SR_{me} is 15 times lower than the calculated expected signal SR_{ex} . This is a familiar phenomenon for aromatic substances, whose fluorescence is only slightly redshifted and usually deep in the UV region where the transmission characteristics of the used optics are not optimal. In addition, the actual quantum yield of 2-fluorophenol

is not known and might be below that of phenol. The measured signal strength is in the same region as that of acetone, i.e. high enough to be of use.

8.9.6 Boundary Layer Visualization

Figure 8.26 shows the course of the 2-fluorophenol measurement. The content of a 1 l gas bag filled with a saturated mixture of 2-fluorophenol and air was emptied into the wind wave tank over a period of 15 s. The decrease of the measured absorbance and the fluorescence signal was used to calculate the transfer velocity by fitting an exponential decay curve to the data. Due to the very low concentration of injected 2-fluorophenol, no condensation effects were expected at the reflective prisms of the spectrometric setup.

2-Fluorophenol			
$u_*: 0.17 \text{ m/s}$			
c_{bulk} :	$1.78 \times 10^{-06} \text{ mol/l}$	Boundary layer:	$27.8 \pm 0.4 \text{ mm}$
c_{surf} :	$8.31 \times 10^{-07} \text{ mol/l}$	Diffusion:	n.a.
$c_{\text{surf}}/c_{\text{bulk}}$:	0.47	$k_{\text{a, profile}}$:	n.a.
Solubility α :	1819	$k_{\text{total, bulk}}$:	$908 \pm 6.3 \text{ cm/h}$
Calibration:	$3.93 \times 10^{-09} \text{ mol/l [DN]}$	$k_{\text{total, spec}}$:	$573 \pm 6.7 \text{ cm/h}$

Table 8.17: Results of 2-fluorophenol mass transfer measurements.

Looking at the results in table 8.17, the transfer velocity determined using the bulk fluorescence data is significantly higher than that derived from spectroscopic data. This could be caused by a shift in the spectrum of the spectrometer light source, shifting an absorption peak into the observed wavelength region. The measured profile is shown in (8.27). The water-sided fluorescence is not more distinctive than with other tracers despite the high solubility of 2-fluorophenol.

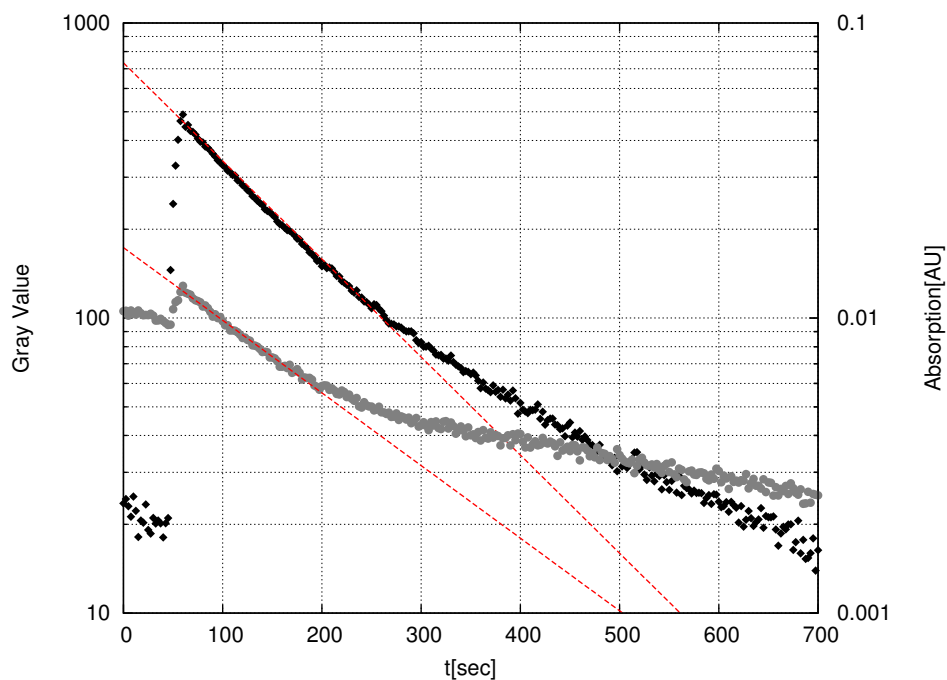


Figure 8.26: Sequential development of the fluorescence signal strength in the bulk (black squares) and the absorption measured by the spectrometer (gray circles) over time

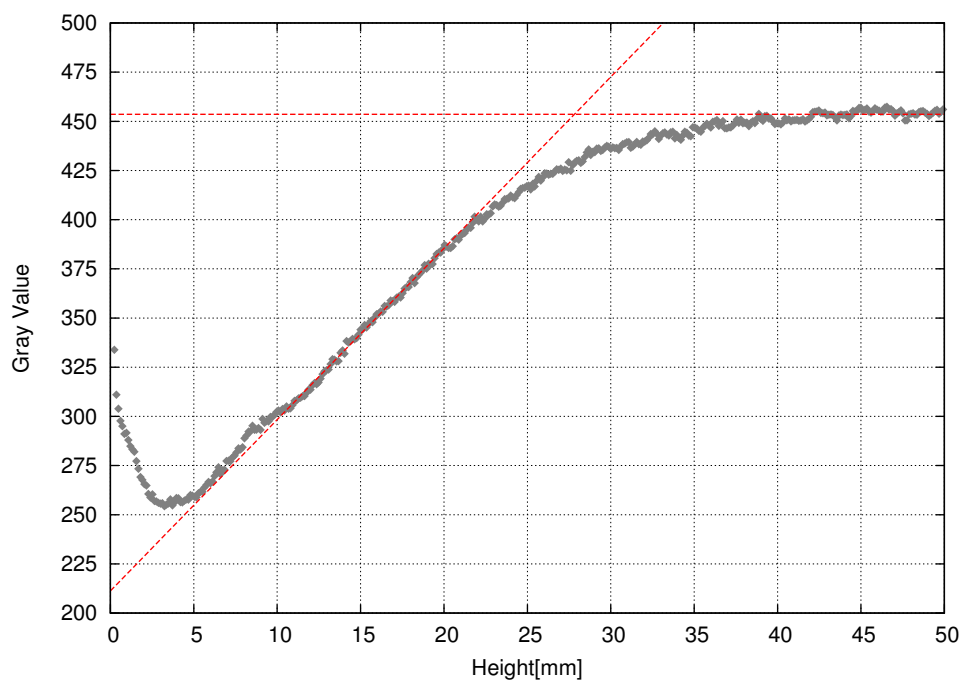


Figure 8.27: Concentration profile with fitted straight lines to evaluate the constant bulk concentration and the linear profile at the surface.

8.10 2-Methoxyphenol

2-Methoxyphenol (commonly called Guaiacol) is composed of an aromatic ring structure with an added hydroxyl group, as is typical for phenols. In addition, it features a methoxy group. Its molecular formula is $C_7H_8O_2$ and the structural formula is shown in figure 8.28. It is a naturally occurring compound with a distinct smoky smell.

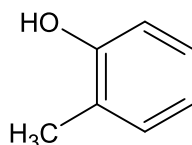


Figure 8.28: The structural formula of 2-Methoxyphenol.

8.10.1 Physical Properties

2-Methoxyphenol is a colorless oily substance which darkens when exposed to light. Its boiling point is 205°C and its melting point is 28°C . 2-Methoxyphenol has a molecular weight of 124.13 g/mol and a density of 1.13 g/cm^3 . Its vapor pressure at room temperature of 0.18 mBar [32] is very low.

Again, the high solubility of phenols motivates the interest for this study. 2-Methoxyphenol has an air-water partition coefficient of $\alpha = 21950$ [63]. That is an order of magnitude higher than that of any other studied molecule.

8.10.2 Optical Properties

No previous studies of 2-methoxyphenol fluorescence in flow visualization experiments have been found.

Absorption As with 2-fluorophenol, no absorption spectra of 2-methoxyphenol were available, but it was listed in Dearden [15] with its absorption bands. It has a maximum absorption cross section σ of $9.75 \times 10^{-18}\text{ cm}^2$ at a wavelength of 273.5 nm and an absorption cross section σ of $5.35 \times 10^{-18}\text{ cm}^2$ at a wavelength of 266 nm .

Luminescence The fluorescence quantum yield of 2-methoxyphenol was not known but assumed to be in the same region as that of phenol. Phenol has a fluorescence quantum yield of 0.08 . This was used as an estimate for the calculations below. The same assumption was made for the fluorescence life-time, which is assumed to be similar to that of phenol (2.1 ns).

8.10.3 Safety and Health Considerations

Exposure to 2-Methoxyphenol in high doses can cause burns on the skin and severe irritation of the eyes.

8.10.4 Measurement Parameters

Laser Excitation Limit With a supposed fluorescence life-time of 2.1 ns and an absorption cross section σ of $9.75 \times 10^{-18} \text{ cm}^2$, the excitation limit for 2-methoxyphenol was calculated to be $8.90 \times 10^{25} \text{ photons/cm}^2 \text{ s}$. The peak irradiance of the CRF 266 laser system is $3.72 \times 10^{25} \text{ photons/cm}^2 \text{ s}$.

Concentration Limit 2-Methoxyphenol's absorption cross section σ of $9.75 \times 10^{-18} \text{ cm}^2$ results in a maximum concentration of $6.46 \times 10^{-06} \text{ mol/l}$ or 88.23% before the tracer air mixture has to be considered optically thick.

Tracer Injection 2-Methoxyphenol was injected into the wind-wave tank using a 25 l tedlar bag. 0.015 ml were injected into the gas bag 3 hours before the experiment started. The flow controller used to inject the saturated air into the wind-wave tank allows for a maximum air flow of 20 l/min.

8.10.5 Signal Strength

Table 8.18 shows the results of the 2-methoxyphenol vapor fluorescence measurements. The measured signal SR_{me} is about two orders of magnitude below the expected signal

2-Methoxyphenol			
ρ_{max} :	$3.89 \times 10^{20} \text{ 1/m}^3$	Fluor. Yield Φ_f :	0.08
ρ_{exp} :	$3.66 \times 10^{19} \text{ 1/m}^3$	SR_{max} :	$3.04 \times 10^{-02} \text{ 1/m}$
$\text{Air}_{\text{sat.}}/\text{Air}_{\text{pure}}$:	88.23 %	SR_{ex} :	$1.57 \times 10^{-03} \text{ 1/m}$
Sat. Excitation:	$8.90 \times 10^{25} \text{ N}_{\text{ph}}/\text{cm}^2 \text{ s}$	SR_{me} :	$4.14 \times 10^{-05} \text{ 1/m}$

Table 8.18: Evaluation of 2-methoxyphenol as a fluorescence tracer in wind-wave tank experiments.

SR_{ex} , i.e. a typical result for a tracer whose fluorescence is in the UV region. Due to the very high solubility the signal evaluation was greatly hindered by the strong fluorescence signal originating in the water.

8.10.6 Boundary Layer Visualization

Figure 8.29 shows the course of the 2-methoxyphenol measurement. The content of a 25 l gas bag filled with a saturated mixture of 2-methoxyphenol and air was emptied into the wind wave tank over a period of 75 s. The decrease of the measured absorbance and the fluorescence signal was used to calculate the transfer velocity by fitting an exponential decay curve to the data. Due to the high solubility the analysis of the 2-methoxyphenol fluorescence proved difficult. The algorithm used to find the water surface did not always work correctly resulting in a less stable signal than that of other tracers with comparable characteristics. In addition the fluorescence data shows a not explainable rise at 200 s after the begin of the measurement. It seems likely that the spectrometric setup did not work as intended.

2-Methoxyphenol			
$u_*: 0.17 \text{ m/s}$			
c_{bulk} :	$1.27 \times 10^{-06} \text{ mol/l}$	Boundary layer:	$32.0 \pm 0.8 \text{ mm}$
c_{surf} :	$9.34 \times 10^{-07} \text{ mol/l}$	Diffusion:	n.a.
$c_{\text{surf}}/c_{\text{bulk}}$:	0.74	$k_{a, \text{ profile}}$:	n.a.
Solubility α :	21950	$k_{\text{total, bulk}}$:	$42 \pm 0.8 \text{ cm/h}$
Calibration:	$2.20 \times 10^{-09} \text{ mol/l [DN]}$	$k_{\text{total, spec}}$:	$533 \pm 27.4 \text{ cm/h}$

Table 8.19: Results of 2-methoxyphenol mass transfer measurements.

Looking at the results in table 8.19, the transfer velocity determined from the bulk fluorescence data is significantly lower than that of the spectroscopic data. Given the unexplainable rise of the absorbance after 200 s, it seems likely that the spectrometric measurement of 2-methoxyphenol failed. The measured profile is shown in (8.30). With a solubility α of 21950 the effects of water sided fluorescence are far more pronounced in the 2-methoxyphenol measurement than for any other tracer in this study. The measured boundary layer is also about 5 mm thicker than that of the other tracers. No diffusion coefficient and thus Schmidt Number for 2-methoxyphenol was found in the literature, but it seems unlikely that it differs so strongly from that of the other studied tracers to give rise to that significant change in boundary layer thickness.

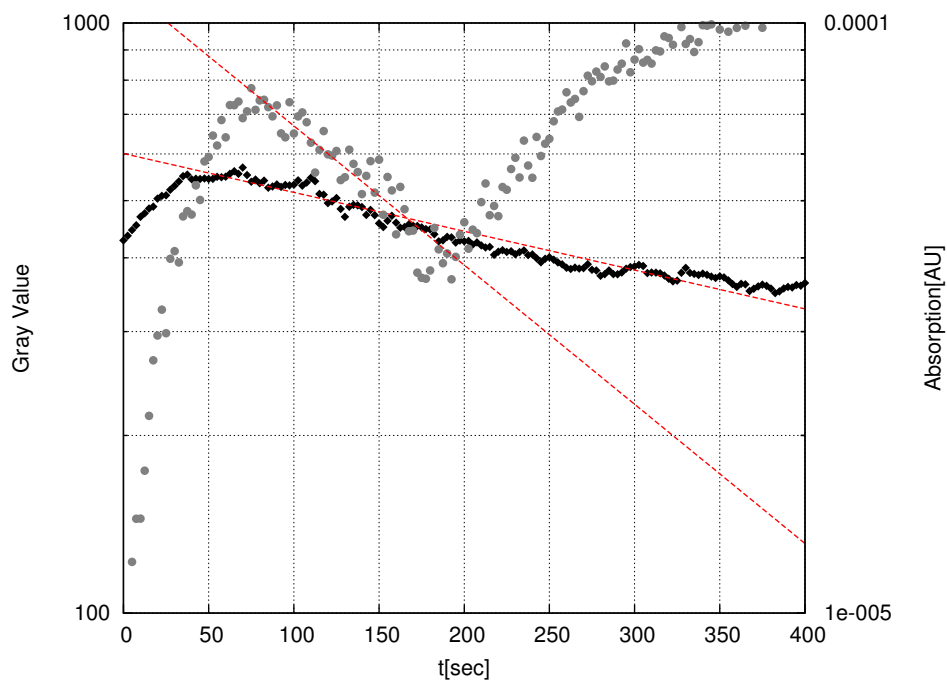


Figure 8.29: Sequential development of the fluorescence signal strength in the bulk (black squares) and the absorption measured by the spectrometer (gray circles) over time

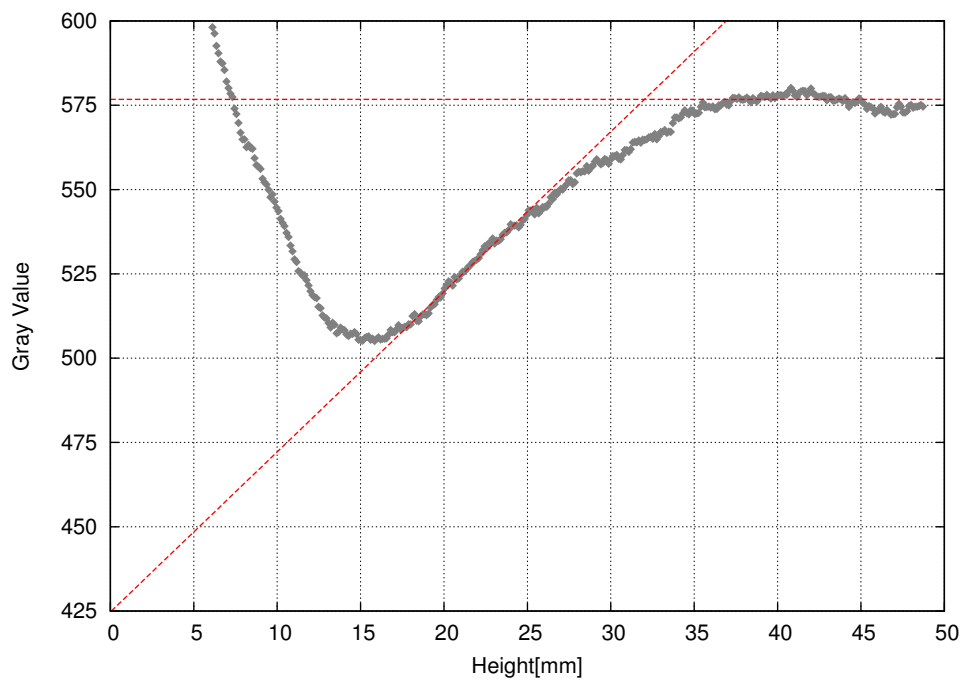


Figure 8.30: Concentration profile with fitted straight lines to evaluate the constant bulk concentration and the linear profile at the surface.

8.11 Other Tracers

The following section covers several tracers that have not been measured in the current setup. The following substances might be interesting for future measurements or were rejected because measurements in the preliminary setup (see 6.1) showed significant problems rendering them unsuitable for application in a wind-wave tank.

8.11.1 Diacetyl

Diacetyl (IUPAC: 2,3-Butanedione, molecular formula: $C_4H_6O_2$) is a commonly used LIF tracer in combustion engine diagnostics. Its fluorescence characteristics are well known and studied [26, 38]. The absorption and fluorescence spectra of diacetyl are shown in appendix B.3.2. With a peak absorption cross section of $8 \times 10^{-20} \text{ cm}^2$ at 417 nm and a fluorescence quantum yield of 0.0025, it is a fluorescence tracer of similar efficiency as acetone if an appropriate laser source is available. With a vapor pressure of 63.32 mbar [47], the expected signal is lower, though. While diacetyl also has a significant absorption cross section in the UV region due to the carbonyl groups, the fluorescence quantum yield for this absorption is close to zero. For a 417 nm laser source with an output power of 1 Watt, the expected fluorescence signal SR_{exp} is $1.7 \times 10^{-4} \text{ 1/m}$, about half as high as that of acetone.

In contrast, the phosphorescence quantum yield η_{ph} of diacetyl is 0.15 with a life-time of 1.6 ms at room temperature [38]. If oxygen quenching can be neglected (i.e. when working in a nitrogen environment) the phosphorescence of diacetyl has a signal rating of $1 \times 10^{-2} \text{ 1/m}$, which is over 30 times the SR_{exp} of acetone or half as high as the SR_{exp} of fluorobenzene.

First qualitative tests were successfully carried out with a blue diode laser¹ with a maximum output power of 600 mW. Despite the lower laser intensity and a laboratory atmosphere containing about 20% oxygen the signal was high enough for detection and visualization of a concentration profile.

8.11.2 2,3-Pentanedione

Another diketone similar the aforementioned diacetyl, 2,3-pentanedione's (molecular formula: $C_5H_8O_2$) fluorescence generating absorption is in the visible light region. Its maximum absorption cross section is $8 \times 10^{-20} \text{ cm}^2$ (nearly the same as acetone) and its fluorescence yield for excitation with a wavelength of 400 nm or higher is 0.0011 [34]. Due to its lower vapor pressure of 26.70 mbar [52], 2,3-pentanedione is less efficient as a fluorescent tracer used in air-sided LIF than diacetyl. SR_{exp} was calculated to be 6×10^{-13} , one order of magnitude below that of diacetyl.

¹Nano-250-445-450, manufactured by RGB-Lasersysteme GmbH, previously used by Herzog et al. [29]

8.11.3 Benzaldehyde

Benzaldehyde (molecular formula C_7H_6O) was tested in the preliminary measurement setup (see 6.1). Despite the high absorption cross section of about $7.7 \times 10^{-20} \text{ cm}^2$ at 266 nm [43], no fluorescence could be observed in the experiment. The substance needs to be mentioned here since it polymerized during the measurements, clogging parts of the setup and causing extensive rebuilding work. Using this substance in wind-wave tank experiments is not encouraged.

8.11.4 Indolizine

Indolizine is an indole isomer and was specifically chosen at the beginning of this study because of its exceptionally high fluorescence quantum yield. Lerner et al. [42] reports a quantum yield η of 0.84 and an absorption cross section of $38 \times 10^{-20} \text{ cm}^2$. Indolizine is in its solid state at room temperature and has a very low vapor pressure. In the preliminary setup, no fluorescence could be observed. In addition, it contaminated the entire system leaving green stains on all synthetic and metallic surfaces. This was a solvable problem in the preliminary setup, but using indolizine in a wind-wave tank would inevitably result in permanent contamination.

8.11.5 Sulfur dioxide

Sulfur dioxide (SO_2) is another fluorescent tracer used in combustion engine diagnostics. Sick [62] reports successful fluorescence measurements using a 266 nm of similar dimensions as the one used in this study. Sulfur dioxide forms sulfuric acid (H_2SO_3) when in contact with water. The amount of SO_2 the water will accommodate and thus the solubility α is enhanced by this reaction which in turn depends on the ph-value of the water (see Degreif [16] for details on chemically enhanced gas exchange). Using SO_2 as a tracer substance would allow for solubility depended measurements using a single tracer substance considerably simplifying comparisons.

Sulfur dioxide fluorescence could be observed in the preliminary setup, but so far no measurements in a wind-wave tank were conducted. The tank is equipped with a stirring tank that can be used to prepare water of defined acidity and the system is highly corrosion resistant (see detailed description in appendix A). All prerequisites are met to measure SO_2 gas transfer.

9 Summary of Results

The results of the previous chapter are collected here, to allow for an comparative discussion. The various tested substances are evaluated in terms of their viability as fluorescent tracers for LIF experiments in general and with respect to their usefulness for gas exchange measurements.

9.1 Air-sided LIF

The results of the fluorescence measurements are gathered in table 9.1. In general, every tracer substance with a measured signal rating SR_{me} of $10^{-4} 1/m$ reached sufficient image quality to gather profile data. This data was averaged over 50 individual measurements however. For individual measurements that result is equivalent to a gray value of approximately 400 [DN] (for a camera gain setting of 50). With a dark noise of approximately 190 [DN] individual profile measurements are no option using the current laser and camera combination for most tracer substances. Of all substances used with a camera gain of 50, only fluorobenzene and 4-fluoroanisole utilize a significant fraction of the Sensicam's dynamic range for their sir-side signal. 1,4-Difluorobenzene was used

Tracer	SR_{max} $1/m$	SR_{ex} $1/m$	SR_{me} $1/m$	$\frac{SR_{me}}{SR_{ex}}$	max. [DN]
Acetone	4.45×10^{-04}	2.80×10^{-04}	4.09×10^{-05}	0.1463	587
Ethanal	3.94×10^{-04}	2.55×10^{-04}	1.56×10^{-05}	0.0612	224
Fluorobenzene	2.71×10^{-02}	1.86×10^{-02}	1.24×10^{-04}	0.0066	1775
1,4-Difluorobenzene	2.76×10^{-01}	5.81×10^{-02}	9.17×10^{-05}	0.0016	1314
Anisole	6.04×10^{-02}	9.27×10^{-03}	5.07×10^{-05}	0.0055	726
4-fluoro-Anisole	4.49×10^{-02}	n.a.	1.10×10^{-04}	n.a.	1575
4-methyl-Anisole	8.77×10^{-02}	n.a.	1.24×10^{-05}	n.a.	177
2,4-difluoro-Anisole	n.a.	n.a.	5.34×10^{-05}	n.a.	765
2-fluoro-Phenol	1.67×10^{-02}	2.06×10^{-03}	3.46×10^{-05}	0.0168	495
2-methoxy-Phenol	3.04×10^{-02}	1.57×10^{-03}	4.14×10^{-05}	0.0264	593

Table 9.1: Summary of the tracer suitability measurements.

with a gain of 5 and the acquired maximum gray value is still among the highest of the examined tracer substances. By tweaking the measurement parameters individual profile measurements should be possible using 1,4-difluorobenzene with the current combination of laser and camera.

When comparing the measured signal rating SR_{me} to the theoretically possible signal ratings for the conducted experiments SR_{ex} and for optimal experiments SR_{max} it becomes obvious that there is a significant room for improvement in the current setup.

The difference between SR_{max} and SR_{ex} is based on the tracer injection. By optimizing the injection to guarantee a tracer concentration near the limit imposed by optical thickness these two become identical. For most tracers an improvement of the injection can improve the signal by a factor of 2. As of this writing this has already been done. The flow controller used for the presented measurements has been replaced with a more precise instrument allowing for measurements closer to the concentration limit.

Comparing SR_{me} to SR_{ex} though, shows a significant difference. The measured signal for most tracers is about two orders of magnitude below the expected signal. The reason for this difference are the combined transmission characteristics of the optics used for the signal measurements that have been shown in figure 6.4. Signals below a wavelength of 280 nm are reduced to 1% of their original strength. This is mainly caused by the transmission characteristics of the Borofloat glass used for the wind-wave tank. The fluorescence of the ketones acetone and ethanal, with a maximum in the region of 300 nm, is not as significantly hindered as that of the aromatic substances, that have a fluorescence closer to the excitation wavelength of 266 nm.

In contrast to classic applications of PLIF in the gaseous phase, the measurement at the air-water interface limits the energy of the used laser system. With a peak energy of approx. 8 MW the current system is powerful enough to vaporize water when focused. To assure unimpeded measurements of the concentration profile the laser is widened into a sheet. With an average energy of 1 W at 20 pulses per second and a pulse length of 6 ns, there is room for improvement of the laser system. If a continuous wave (cw) laser system of similar or higher output power can be found, the beam would not have to be widened as the peak energy of a cw-laser is the average energy. The problem of water evaporation would vanish. Currently, such systems are still in development. Another option would be pulsed systems utilizing higher frequencies or longer pulse length, resulting in a reduced peak power.

9.1.1 Resolution

Examining the acquired profiles in chapter 8, a measurement problem becomes apparent. Close to the water surface the recorded fluorescence signal rises although the concentration should lower itself until a minimum at the water surface is reached. When

discussing the resolution of a PLIF setup in section 5.5, the limited depth resolution caused by the laser sheet thickness was already mentioned. A very specific problem was not foreseeable though and will be discussed here in greater detail:

The camera was mounted with an angle of 5° relative to the laser sheet and water surface to avoid obfuscation by water waves. Applying equation 5.29 with a sheet width w of 1 mm and a camera angle of 5° Δm is equal to $87 \mu\text{m}$ for this measurement system. With a vertical resolution of $140 \mu\text{m}$ per pixel, the water-sided fluorescence could at worst influence the signal measured by two pixel if the water surface is seen by both of them and the system should be able to image the concentration profile down to $280 \mu\text{m}$ above the water surface.

Δh , the height that defines the volume the monitored concentration was integrated over, is equal to the height a single pixel is projected to ($140 \mu\text{m}$) plus Δm . For this system the vertical resolution is $227 \mu\text{m}$. The profiles in chapter 8 clearly show that other effects reduce the maximum proximity to the surface to which the concentration profile can be measured.

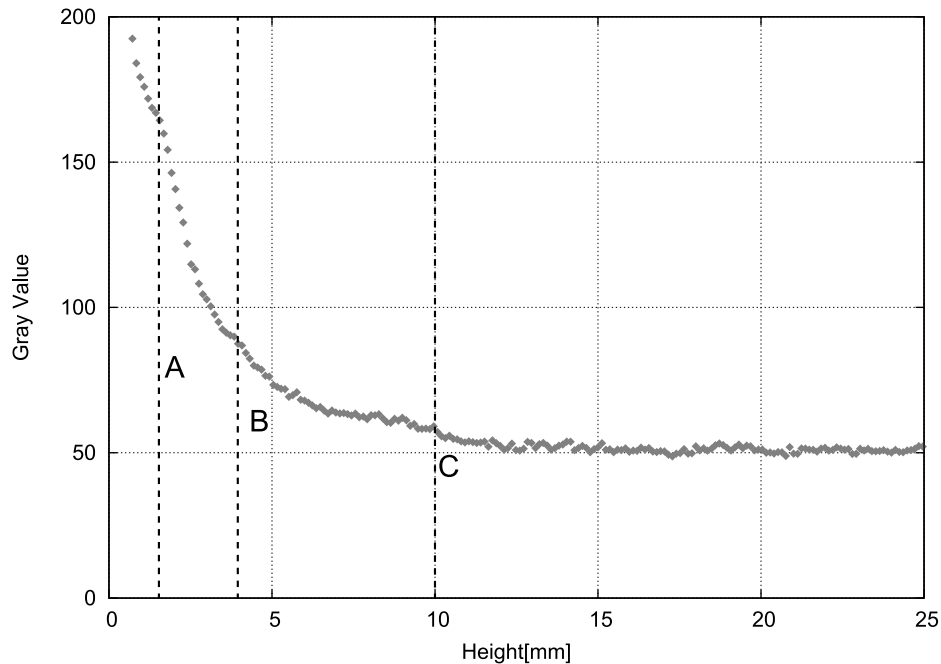


Figure 9.1: Profile acquired after a measurement. No fluorescence tracer was left in the air, the signal increase near the water surface is divided into three distinct sections.

Figure 9.1 shows a profile acquired after a tracer measurement. No fluorescent tracer was left in the air but the camera is still able to monitor a signal increase near the water surface. Assuming the signal results from light originating from the water surface, by solving equation 5.29 for w , it can be used to calculate the origin of the various

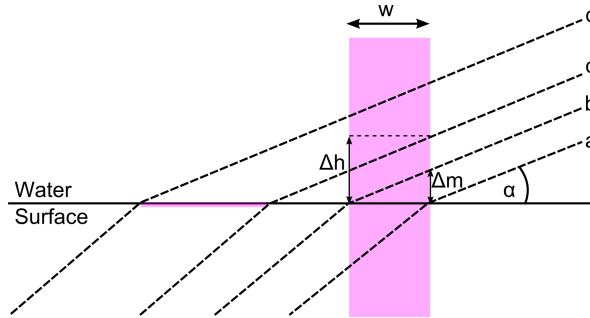


Figure 9.2: Effect of the camera slope α on the vertical resolution of the acquired image. Between c and d an unspecified signal on the water surface corrupts the measurement.

signals overlaid to the actual profiles. Figure 9.2 is an extended version of figure 5.2 illustrating the problem.

$$w = \frac{h}{\tan(5^\circ)} \quad (9.1)$$

The light monitored up to the height A (2 mm) results from an area up to 22.8 mm behind the laser sheet. A possible source for this could be the small fraction of 532 nm light that is not filtered out of the laser beam. As the optical setup is not optimized for this wavelength it results in a wider spot on the water surface.

Signals monitored up to the height B (4 mm) result from an area up to 45 mm behind the laser sheet. This distinctive bump in the intensity profile can be seen in every profile measurement. So far, no explanation has been found.

The height C (10 mm) corresponds to a width of 114 mm, which is half the width of the wind-wave tank. The simplest explanation for this signal would be stray light present that reflects upon the water surface.

All measurements were conducted in the dark with a additional effort taken to isolate the setup from any stray light generated by computer monitors. The only light that cannot be blocked is the intensive water-sided fluorescence light. As the concentration of the tracers in water is higher by the factor α (the solubility) than the surface concentration in air, the water-side fluorescence signal can be one or more orders of magnitude higher than the fluorescence in air. This results in a significant source of stray light within the otherwise darkened setup that is reflected on the glass surfaces of the wind-wave tank interior.

In summary all concentration profiles acquired have a resolution no better than 227 μm and up to a height of 10 mm above the surface the signal is overlaid by stray light that can at this point not be sufficiently defined to be subtracted out of the images.

9.1.2 Water-Sided Fluorescence

For most tracers the intensity of the water-side fluorescence is sufficient to saturate the camera sensor when the camera is used at gain settings where the air-side fluorescence can be monitored. This makes a parallel measurement of the fluorescence on both sides of the interface impossible with the currently employed camera and causes significant difficulties for the measurement on the air-side.

By using a camera with a significantly higher dynamic range than the currently employed Sensicam-UV, the fluorescence at the water surface could be measured together with the air-sided signal with a single acquisition system. If this is done with adequate precision, the solubility α during a dynamic process can be measured directly.

The water-side signal intensity is so strong that it is possible to take a picture using a hand-held camera, as seen in figure 9.3. While this poses a significant problem for the air-sided measurements as explained above it also provides an opportunity for water-sided profile measurements that are substantially easier to prepare and execute than what has previously been done.

Water-side concentration profile measurements so far use a secondary effect to image the concentration. A common technique is the use of a pH-dependent fluorescent tracer that changes its fluorescent quantum yield based on the local pH. This has been done by Münsterer and Jähne [46] who used fluorescein which changes its quantum yield dependent on local pH. A more recent study by Herzog [28] used HPTS as an indicator, gaining a better signal. The observed gas in both cases was HCl. This technique requires a highly corrosion resistant wind-wave tank and a well controlled pH of the water.

Another technique is the study of the fluorescence quenching by oxygen. This has been done by Falkenroth [20], using a Ruthenium complex whose fluorescence is strongly quenched by the presence of oxygen.

The indirect methods have two problems in common: They require a greater amount of preparation than the direct visualization of a tracer substance and they are limited to a single gas whose transport can be monitored. Using the substances presented in this study for water-sided fluorescence measurements could greatly expand the field of traceable substances. The biggest obstacles so far are, the significantly slimmer boundary

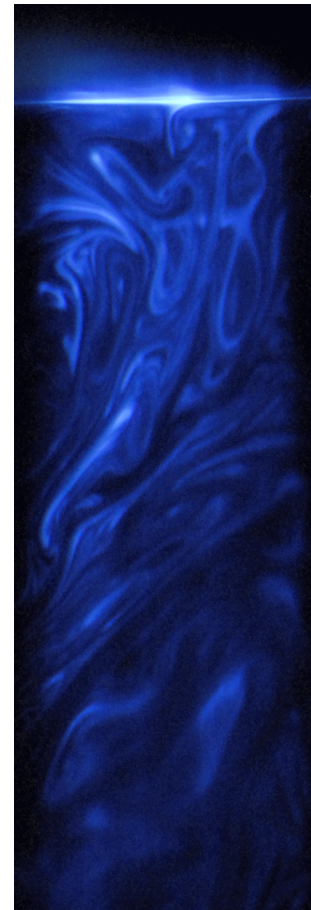


Figure 9.3: Photograph of acetone fluorescence in water.

layer on the water-side requires a resolution of 50 μm or better to gain any usable results. With the current setup that cannot be done. A laser system with a higher focusability and a UV-macro-objective lens would be needed to reach that imaging quality.

9.2 Transfer Measurements

The results of the transfer results are summarized in table 9.2. Despite the fact that the motor frequency and thus the strength of the wind generating fan was held constant the values for u_* differ across the measurements. The wind profiles were measured directly after the concentration profile measurements. The variance in u_* could be an effect of the tracer on the surface tension of the water.

Tracer	Sol. α	D_{air} [cm^2/s]	Sc_{air}	u_* [m/s]	z_* [mm]	$k_{\text{a,th}}$ [cm/h]	$k_{\text{a,me}}$ [cm/h]
Acetone	732	0.11	1.44	0.18	20.7	3368	182
Ethanal	342	0.15	1.05	0.18	7.7	4191	678
Fluorobenzene	3.9	0.10	1.56	0.16	28.7	2906	122
1,4-Difluorobenzene	3.2	0.06	2.62	0.12	28.9	1572	72
Anisole	5.9	0.07	2.08	0.17	26.8	2637	98
4-fluoro-Anisole	n.a.	n.a.	n.a.	0.12	28.9	n.a.	n.a.
4-methyl-Anisole	n.a.	n.a.	n.a.	0.12	26.1	n.a.	n.a.
2,4-difluoro-Anisole	n.a.	n.a.	n.a.	0.12	28.5	n.a.	n.a.
2-fluoro-Phenol	1819	n.a.	n.a.	0.17	27.8	n.a.	n.a.
2-methoxy-Phenol	21950	n.a.	n.a.	0.17	32.0	n.a.	n.a.

Table 9.2: Summary of the mass transfer measurements. For some tracers no diffusion coefficients were available and consequently no transfer velocity could be derived from the profile and from Deacon's parametrization.

Using the appropriate values of u_* a transfer velocity $k_{\text{a,th}}$ was calculated using the formulation of Deacon (equation 2.59). The boundary layer thickness z_* was acquired geometrically from the measured profiles (see section 2.3.1). The measured transfer velocity $k_{\text{a,me}}$ was calculated from the diffusion coefficient D_{air} of the tracer substance in air and z_* using equation (2.51).

According to the calculations done in section 2.3.3 the air-sided boundary layer of substances with an Schmidt number $Sc = 1 - 3$ should be 0.6 - 1.8 mm thick. The measured boundary layer thicknesses shown in table 9.2 range from 20 mm to 32 mm. When comparing the measured profiles to the velocity profiles acquired by the Pitot-tube the source of this deviation becomes visible (see figure 9.4). The shape of concentration

profiles of tracers with $Sc \approx 1$ and velocity profiles should be similar. The concentration gradient at a height of 10 – 20 mm was identified as linear and the analysis was done accordingly. At these heights the velocity profile still shows a logarithmic shape. The actual linear part of the profile is much closer to the surface and a lot steeper, which would result in lower values for z_* . The measured transfer velocity $k_{a,me}$ is 1-2 orders of magnitude below the theoretically expected transfer velocity $k_{a,th}$. As $k_{a,me}$ is proportional to z_* this deviation was expected.

Various problems with the acquisition of profile data close to the air-water interface have been discussed in the previous section. The fact that the profiles show a clearly linear shape though, underlines the conclusion that the source of the imaging artifacts

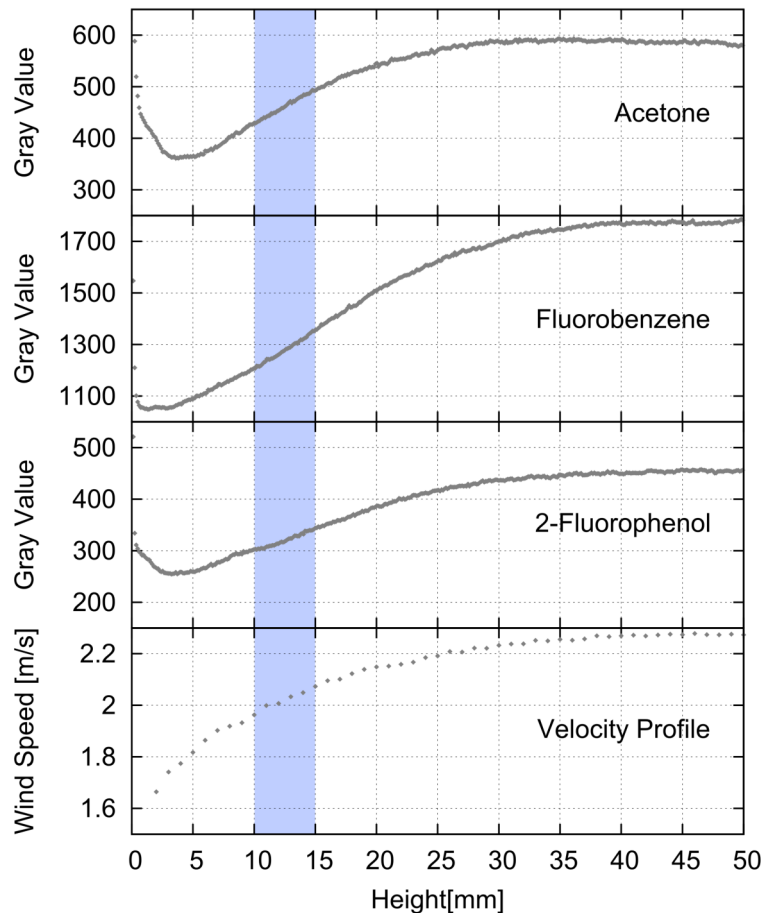


Figure 9.4: The measured concentration profiles of acetone, fluorobenzene and 2-fluorophenole compared to a velocity profile at 13.5 Hz motor frequency. The shaded area marks the range chosen for the linear fit used to obtain the boundary layer thickness. The velocity profile in this area is of logarithmic shape, pointing to an error in the fluorescence data acquired close to the surface.

has to be further investigated and if possible eliminated. As long as there remains doubt if the measured profile at a given height is actually linear or just an overlay of several gradients that happens to be linear the air-sided LIF technique for mass transfer measurements remains problematic.

9.3 Controlling Phase

The data was evaluated with a view towards the controlling phase of the transport (see section 2.3.4). The relevant results are summarized in table 9.3. The surface and bulk concentrations are directly calculated using the calibration factor derived from the spectrometric measurements and the profile data with the surface concentration being extrapolated from the slope of the linear part of the profile. Solubility data is not available for every tracer examined reducing the number of tracers with complete data sets to seven: Acetone, ethanal, 1,4-difluorobenzene, fluorobenzene, anisole and 2-fluoro-phenol and 2-methoxy-phenol. The ratio of the air-sided surface and bulk concentration provides information about the controlling layer if the solubility of a tracer is known. The ratio of the transfer resistances (and consequently velocities) was calculated using equation 2.67.

Tracer	Sol. α	c_a [mol/l]	c_{as} [mol/l]	c_{as}/c_a	R_a/R_w
Acetone	732	4.08×10^{-04}	1.97×10^{-04}	0.48	1.47×10^{-03}
Ethanal	342	1.91×10^{-03}	1.62×10^{-03}	0.85	5.29×10^{-04}
Fluorobenzene	3.9	5.42×10^{-06}	2.74×10^{-06}	0.51	2.50×10^{-01}
1,4-Difluorobenzene	3.2	5.64×10^{-06}	2.54×10^{-06}	0.45	3.82×10^{-01}
Anisole	5.9	1.94×10^{-06}	8.14×10^{-07}	0.42	2.35×10^{-01}
4-fluoro-Anisole	n.a.	1.11×10^{-07}	4.94×10^{-08}	0.44	n.a.
4-methyl-Anisole	n.a.	2.23×10^{-06}	1.56×10^{-06}	0.70	n.a.
2,4-difluoro-Anisole	n.a.	n.a.	n.a.	0.54	n.a.
2-fluoro-Phenol	1819	1.78×10^{-06}	8.31×10^{-07}	0.47	6.31×10^{-04}
2-methoxy-Phenol	21950	1.27×10^{-06}	9.34×10^{-07}	0.74	1.63×10^{-05}

Table 9.3: Air-water transfer partitioning by tracer. The surface concentrations were extrapolated from the linear section of the profiles.

As the correlation of the concentration ratio, resistance ratio and solubility is rather complex, figure 9.5 attempts to show the available data in a clearer fashion. By plotting the measured concentration ratio against the solubility each tracer is mapped onto a region that stands for either the air-sided, water-sided or transition control. The lines of constant resistance ratios are calculated using equation (2.68).

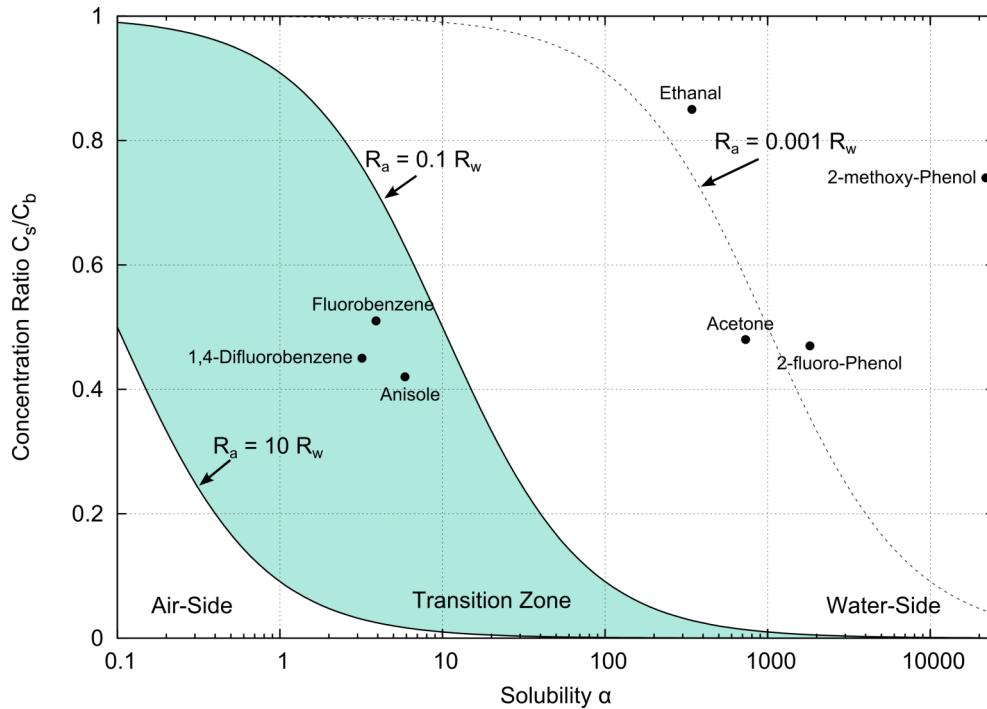


Figure 9.5: Controlling phase diagram plotting the measured concentration ratio against the solubility. The lines of constant transfer resistance ratio were calculated using equation (2.68).

These results are very surprising. Comparing figure 9.5 with figure 2.5, the partition of the tracers in these measurements is actually inverse to what was estimated. Tracers with a high solubility are graded as water-side controlled (acetone, ethanal, 2-fluoro-phenol, 2-methoxy-phenol), while tracers with a low solubility are put into the transient zone.

This is in accordance with the measured data. Even the tracers with lowest solubilities clearly show a concentration decrease towards the surface. For a low solubility tracer to be controlled by the water-side the concentration in air should see no or only a slight decrease. The measurements clearly did not show that. A high solubility tracer can only be considered transient or air-side controlled if the concentration at the water surface is zero or nearly so. The measurements did not provide that either. While the surface concentration might easily be overestimated due to previously discussed measurement problems, the same cannot be said for the decrease in concentration for the low solubility tracers. If the concentration in air would be constant the resulting profiles would show an increase near the surface due to stray light but no previous decrease. An overestimation of the concentration ratio, which is currently highly likely, only puts the tracers closer to the water-side controlled area.

10 Conclusion and Outlook

This study presents the first successful visualization of vertical concentration profiles at the air-side of the moving air-water interface. To achieve this, a planar laser induced fluorescence setup (PLIF) was constructed including a new wind-wave tank, which is optimized for quick visualization experiments. From a set of ten tracer substances several were identified to show sufficient signal strength for experiments in a wind-wave tank.

10.1 Conclusion

In the course of this study several new insights into the application of PLIF at the air-water interface were gained:

Laser System The new setup (see section 6.2) utilizes a pulsed UV-laser operating with a peak power of 8 MW at a pulse length of 6 ns. In contrast to combustion diagnostics and other LIF applications in the gaseous phase where such high energy laser systems are quite common, this causes problems when measuring at the air-water interface. The high peak energy of the laser is sufficient to vaporize the water surface, significantly influencing the measured system. This problem was solved by widening the laser beam into a sheet (creating a PLIF setup) and thus effectively reducing the energy density at the water surface. The loss of signal was compensated by horizontal averaging, to yield vertical concentration profiles (see section 7.3.3).

Water-side Fluorescence The selected tracers in this study exhibit a solubility α greater than 1. The tracer concentration and thus the fluorescence signal dramatically rises at the water surface. This causes the overall measured signal (in air and water) to cover an intensity range that exceeds the dynamic range of the camera (see section 6.2.4).

Resolution The concentration profiles have a vertical resolution of 227 μm . As soon as the tracer substances enter the water body water-side fluorescence is generated by the laser. Reflections of this water-side PLIF sheet at the wind-wave tank glass plates interfere with the measurement of the air-sided concentration profiles near the water surface. Consequently, the current setup does not allow for

measurements of concentration data closer than approximately 10 mm to the surface (see section 9.1.1).

Tracers From the selected tracers, only 1,4-Difluorobenzene has a sufficiently high signal rating to allow for single pulse measurements, i.e. a temporal resolution limited by the camera shutter. The concentration profiles of acetone, fluorobenzene, anisole, 4-fluoroanisole, 2,4-difluoroanisole, 2-fluorophenol and 2-methoxyphenol can be measured by integrating over 50 single pulse measurements (2.5 s). The air-side signal of ethanal and 4-methylanisole was too low for the current setup.

Concentration Profiles Mass transfer velocities were calculated from the acquired vertical concentration profiles by determination of the boundary layer thickness (see 2.3.1). The results show that the maximum proximity to the water surface where undisturbed profiles can be measured needs to be improved to allow for successful local transfer measurements in air. (see 9.2).

Solubility The solubility of the selected tracers covers a range from $\alpha=3$ to $\alpha=22000$. The analysis of the test measurements did not show the expected correlation between α and the partition of the transport resistances with highly soluble tracers being controlled by the air-side and barely soluble substances being water-side controlled (see 9.3).

In summary, PLIF has been proven to be applicable to study air-sided concentration profiles at the air-water interface. A set of eight tracers covering a large range of solubilities was shown to be suitable for PLIF experiments.

10.2 Outlook

With the presented system for air-sided concentration profile measurements a systematic research of the transport properties of the presented tracer substances can be realized. By focusing on tracers that cover a great range of solubilities α (1,4-Difluorobenzene, anisole, acetone and 2-methoxyphenol) further insights into the role of α for the air-water gas exchange can be obtained. Utilizing the high signal rating of 1,4-difluorobenzene for single pulse measurements may help understanding the effect of waves on the air-sided boundary layer.

The source of the reflections interfering with the profile measurements near the water surface needs to be further investigated and suppressed as far as possible. The measured signal can be improved by using a laser with a lower peak power for the fluorescence excitation. (see section 9.1) By utilizing a camera with a significantly higher dynamic range than the currently employed system, the water-side and air-side fluorescence can be measured at once (see section 9.1.2). That will allow for the direct measurement of the solubility α during a dynamic process.

A The Linear Visualization-Test Wind-Wave Tank

During the course of this work a new linear wind-wave tank was built in cooperation with Pius Warken. This section provides a general overview of the new facility as well as an update to description of the tank in Warken [74]. The characterization of the system was completely renewed due to slight improvements to the setup.

A.1 Motivation

The new wind-wave tank was built specifically to allow for fast measurements and easy access. The main task of this facility is a simple setup and evaluation of new measurement techniques, rather than a realistic modeling of the actual circumstances at the ocean surface. The system is relatively compact with a small water volume. It has been constructed in the optics lab which can be totally darkened generating a substantial advantage for fluorescence visualization techniques which often have a low light efficiency. To allow for an easy and quick optical access the visualization-test wind-wave tank is build upon a variable ISEL bar system. This enables a flexible and easy installation of completely new measuring systems. The ISEL bar system can also be expanded to allow for more complex or specialized systems to be installed.

Another item of interest during the construction of the visualization-test wind-wave tank was the handling of chemicals. As the facility should be used for a variety of experiments it was important that it can withstand the aggressive substances needed for some visualization techniques. The small volume of the tank enables not only faster but also more cost-effective experiments. An attached stirred-tank simplifies the usage of chemicals.

These characteristics render this wind-wave tank a valuable addition to the other two tanks (AEOLOTRON, LIZARD[28]) at the HEIDELBERG AEOLOTRON LAB.

A.2 Setup

The whole tank, including instrumentation, has a length of roughly 4 m, a width of ca. 1 m and a height of about 1,5 m. The closed system of the wind-wave-tank contains in the filled state 22l of liquid and an air volume of 220l. A schematic sketch of the setup is shown in figure A.1. Figure A.2 displays the geometry of the water channel. The request of a small water volume is fulfilled by inhibiting water to flow to the volumes in front of and behind the visible deepening in figure A.2. Nevertheless, in the filled state of the facility there is no change of the fetch compared to an uniformly deep geometry. All parts and instruments are installed on a frame of screwed ISEL-PS-40 racks. The benefit of this concept is the flexibility of extensions and mounting opportunities for additional components or measuring equipment. Furthermore, horizontal adjustment can be achieved due to height adjustable pedestals. An additional feature is the stirred tank mounted above the wind-wave tank. It permits filling of the tank with externally prepared chemicals or dissolutions.

The following sections detail the three compartments (water side, air side, stirred tank) and the permanently implemented instruments.

A.2.1 Water System

The water system consists of the actual water tank, a tubing system for filling, draining and circulation of the water and a variety of measuring probes.

The linear tank is made of glass windows and an aluminum base plate (see figure A.2). It is 188.0 cm long, has a constant width of 25.0 cm and a height varying between 22.5 cm and 12.5 cm. The side view of the tank shows its asymmetric shape: The long fetch takes up most of the horizontal dimension of the tank. The short shallow down-wind section contains a wave trap designed from glass tubes that dampen wave reflections at the wind-wave tank's edge.

The deeper middle part of the tank is the measurement section. The tilted windows perpendicular to the wind direction allow the mounting of cameras from below viewing in or against wind direction. This area enables an easy access via an interchangeable cover plate made from PVC. This cover plate can be replaced to satisfy the experiential needs of an individual setup. At the beginning of the channel a second removable cover plate is located which can be removed for better access when cleaning is necessary.

All cover plates are masked with 0.1 mm thick TEFLON foil produced by POLYTETRA to prevent damage to the PVC by chemicals. The flanges connecting the ends of the glass channel to the wind tubing system are covered in the same foil.

The water pipe system is completely made of PP (polypropylen) tubes produced by GEORG FISCHER. Two tube sizes were employed: The bigger tubes primarily used

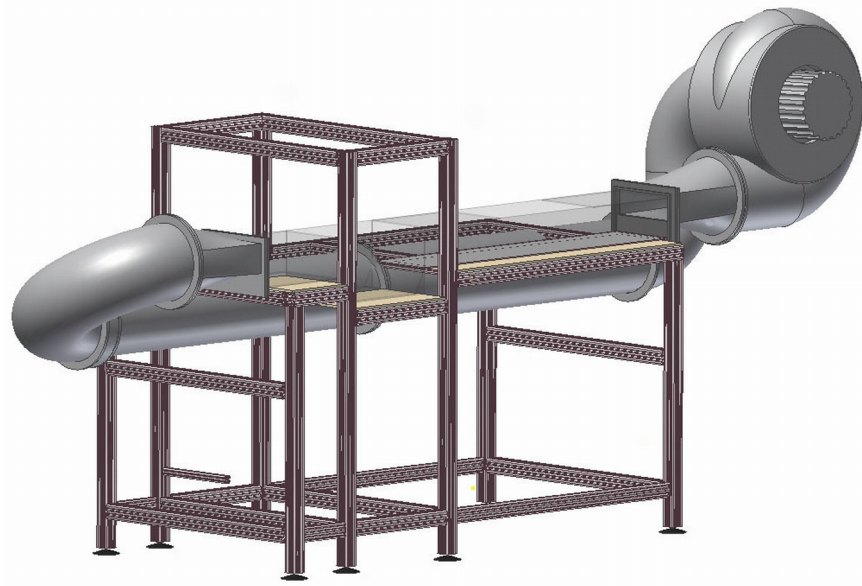


Figure A.1: 3-D graphic of the facility The water channel is mounted upon a ISEL bar system framework for easy access. The facility has a size $4\text{ m} \times 1\text{ m} \times 1.5\text{ m}$.

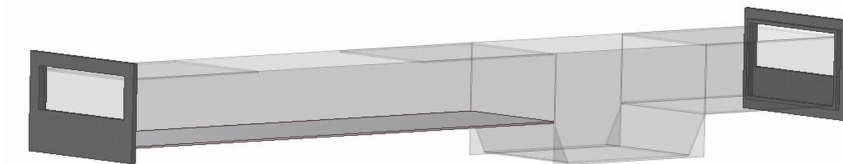


Figure A.2: The water channel The geometry of the water-channel. The recess is at the wind-averted side.

for the drainage system have an external diameter of 32 mm and a wall thickness of 2.9 mm. The thinner circulation system tubes have an external diameter of 20 mm and a wall thickness of 1.9 mm. PP was chosen as material for the tubing systems due to its high chemical resistance and its high workability. Using a heated plate the ends of the tubes can easily be welded together allowing a fully customized setup of the drainage and circulation systems.

The windows of the water channel are made of high-quality borosilicate glass BOROFLOAT 33 manufactured by SCHOTT. It features a high transitivity of more than 90 % for light in the visible spectral region (see figure A.3a) and, in contrast to common glass, has a relatively high transitivity in the UV-region (see figure A.3b). The plates used to build the channel have a thickness of 3.3 mm.

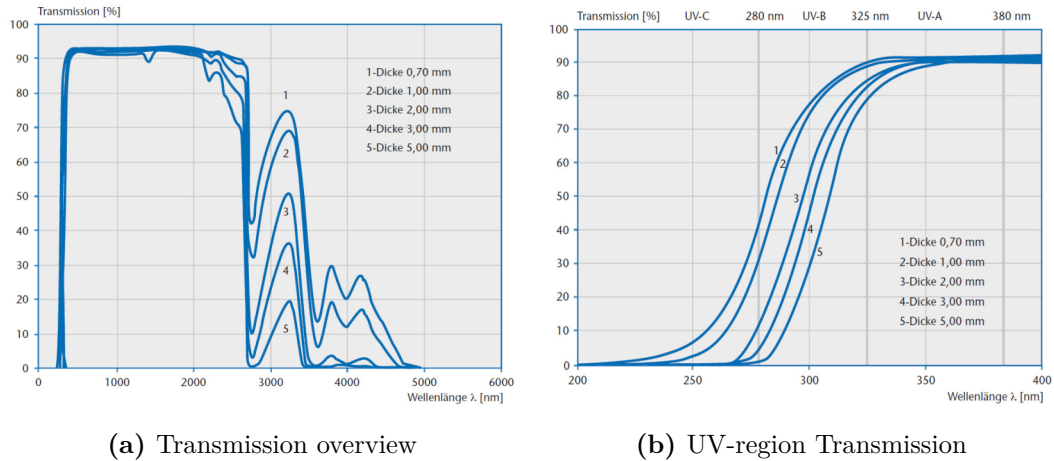


Figure A.3: Optical properties of BOROFLOAT 33; Source: data sheet

The glass plates are glued together using TEROSTAT MS 939 by TEROSON. This substance hardens by incorporation of water, sticks well to glass and is still relatively flexible once set. The last characteristic is of particular importance to compensate for tensions produced by thermal expansion that might otherwise inflict some damage to the glass plates. TEROSTAT MS 939 is surface-active (it can change the surface tension of water), to prevent it having any adverse effects on measurements all splices are masked with TEFLON foil.

The long base plate on the left side of the channel is a 5 mm aluminum plate. While this posed some problems during construction, it allows for an efficient temperature control of the water within the system. This is achieved by using Peltier elements attached to the base plate. With a thermal conductivity of 235 W/m K aluminum is a much better thermal conductor compared to 1.2 W/m K for BOROFLOAT 33. The problem of different thermal expansion coefficients ($23 \cdot 10^{-6}$ 1/K for aluminum and $3.25 \cdot 10^{-6}$ 1/K for BOROFLOAT 33) was compensated for by a 5 mm strong splice filled with TEROSTAT MS 939. The insufficient chemical resistance of the aluminum base plate was solved by coating it with TEFLON foil. This also seals the screw joints connecting the Peltier-fans with the water channel.

Figure A.4 depicts a sketch of the water system setup.

Intake

To fill the wind-wave tank the intake valve needs to be opened before the tap which provides purified water to prevent the water pressure damaging the tubing system. The water enters the tank via the bypass system. The recommended filling level is 3.5 cm, which can be checked at the rulers fixed to the tank. Higher water levels should be used with caution as low wind speeds would suffice to flush water into the air-system and a

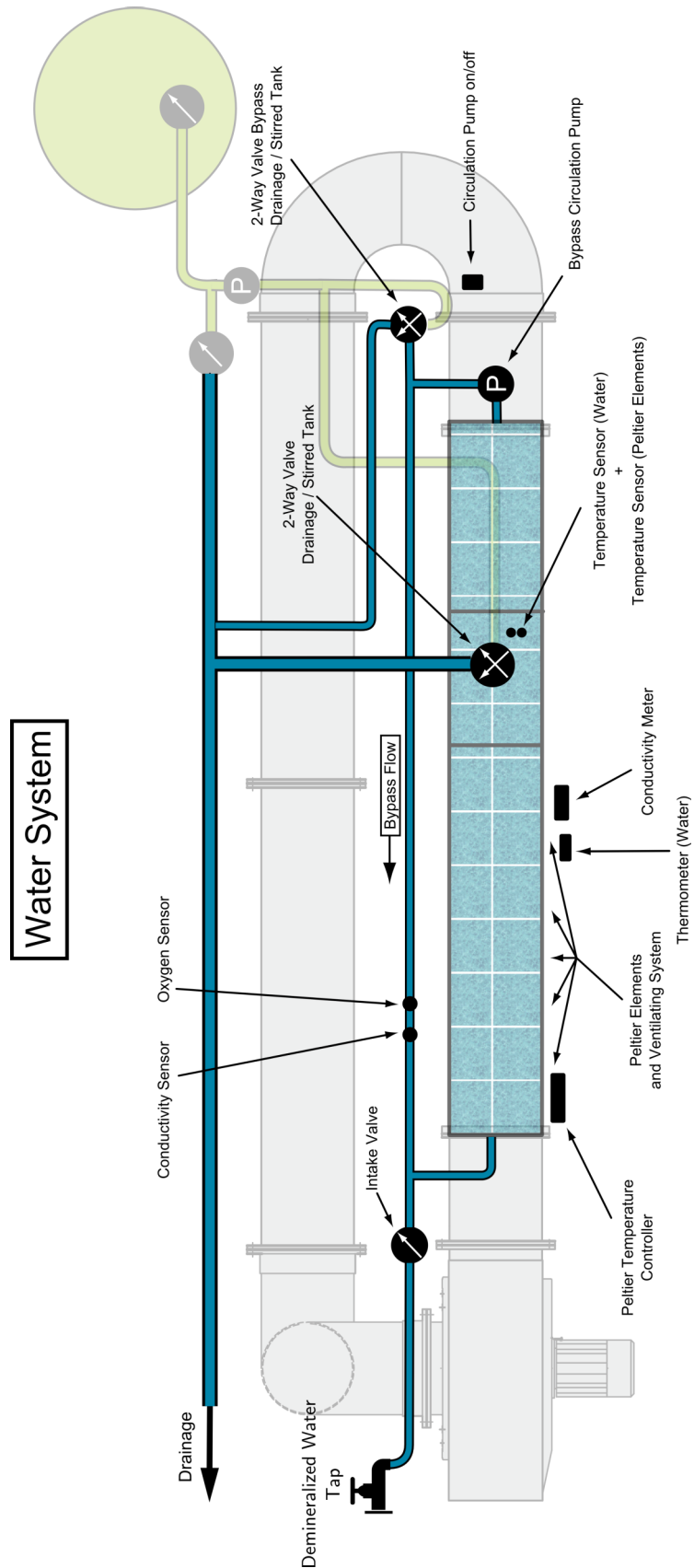


Figure A.4: Schematic setup of the water system

laborious drying of the air tubes would be the consequence. To prevent excess pressure the water tap should be closed before the intake valve after the filling is completed.

Drainage

To remove all water from of the tank two valves have to be opened: The 2-way valve at the bottom of the measurement recess must be switched to enable a water flow towards the drainpipe. To clear the bypass system, the smaller 2-way valve to the right (see figure A.4) must be opened.

Circulation

The water inside the wind-wave tank circulates through the bypass system. The water circuit features a magnetically coupled rotary pump by RS-COMPONENTS with a discharge of 14l/min. It is installed at the lowest point to prevent damage to the pump that could be caused by it running dry. The switch for the pump is located at the right side of the ISEL-bar system the wind-wave tank is mounted on. This setup quickly mixes the water inside the tank and continuously washes water around the sensors inside the bypass tube.

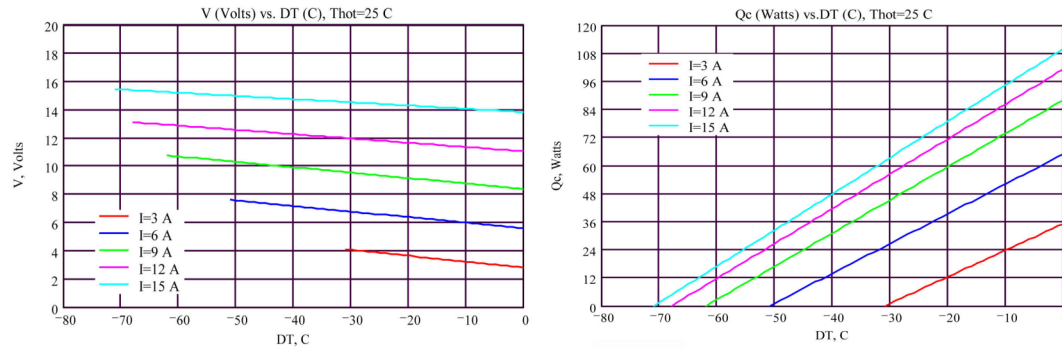
Water-Sided Instrumentation

- **Water Temperature**

The water temperature is continuously monitored using a GREISINGER GMH 3710 precision thermometer. The temperature sensor is a PT100 immersion sensor with an enhanced precision. Its accuracy class is 1/10 DIN B and its measurement precision of $\pm 0.03^\circ\text{C}$ at 0°C . The 3 mm thick sensor is mounted within the deep recess of the channel using a water tight compression fitting. The thermometer, which runs on batteries, is read out by a GREISINGER GRS 3105 interface adapter that transfers the temperature signal to the serial bus allowing the HEURISKO worksheet used for the measurements to monitor and display the temperature continuously.

- **Peltier-Temperature Regulation**

40 QUICK-COOL-Peltier elements (Model: QC-127-2.0-15.0M) are mounted on five fan cooled heat sinks in direct contact to the aluminum base plate of the water channel. 8 peltier elements connected in series form a one set mounted on a single heat sink . The five resulting sets are connected to each other by a parallel circuit which is controlled by a COOLTRONIC-PELTIER-CONTROLLER MODEL TC3215. A 24 V DC power supply provides an electric current of $I = 15\text{ A}$, providing every single Peltier element with 9 W of electric power. According to figure A.5a this is equivalent to a temperature difference between the sides of an element of 10°C , resulting in a cooling capacity of 24 W (see figure A.5b). The



(a) Supply voltage of a Peltier element plotted against the temperature difference for varying various temperature differences and currents
 (b) Thermal output of a Peltier element for against the temperature difference for varying various temperature differences and currents

Figure A.5: $DT = T_{cold} - T_{hot}$: Temperature difference between warm and cold side of a peltier element, Q_c = Cooling Capacity of the cold side, V : DC Supply Voltage, I : Supply Current; Source: data sheet, www.quick-cool.de

contact and transport between the peltier elements, the heat sink and the water channels base plate is optimized using heat conducting foil.

By reversing the polarity of the supply voltage the warm and the cold side of the Peltier element switch allowing the system to both cool and heat the water channel. The Peltier-controller, which is connected to a temperature sensor within the water channel, sets the nominal value of the water temperature. The nominal value can be altered using either the controllers front panel or the serial bus connection.

- **Conductivity**

A GREISINGER GLF 100 RW conductivity meter is employed to measure the conductivity of the liquid in the water channel. The sensor uses a bipolar stainless steel electrode which requires a continuous and bubble free liquid flow to work properly. Therefore it is installed in the bypass. This probe also has an integrated temperature sensor with a precision of ± 0.3 K. The display unit is mounted along the other measuring gauges at the front of the ISEL bar system. This sensor is read out by the same GREISINGER GRS 3105 interface adapter and the same HEURISKO worksheet as the temperature sensor.

- **Oxygenator**

The JOSTRA QUADROX is a medical device made to exchange oxygen and carbon dioxide in human blood. Its function is based on a hydrophilic membrane with a surface of 1.8 m^2 that is permeable for gases but not for liquids. In the wind-wave tank this device is used to filter gases from the water by significantly reducing the pressure on one side of the membrane. Thus the gases are forced to exit the

water due to a strong concentration gradient. The maximum water flow that can pass the oxygenator without risking damage is 7 l/min.

- **Oxygen Sensor**

An optical HAMILTON VISIFERM DO 120 oxygen sensor is integrated into the bypass where it monitors the oxygen concentration of the water in the wind-wave tank. The sensor also measures the water temperature and corrects for the temperature dependence of the oxygen concentration. It has a detection limit of 0.01 % oxygen in water.

A.2.2 Air System

The air-system of the wind-wave tank is a custom made circulatory tube system built by HÜRNER-FUNKEN. Its exact dimensions are shown in figure A.6. The individual segments are connected and sealed by flange connections which can be reopened with relative ease. The tubes consist of chemical and flame resistant PPS. A sketch of the air system is shown in figure A.7.

A radial fan (HFR 250-15 D/R) controlled by a SIEMENS SINAMICS G110 0.75 kW frequency generator blows air through the wind-wave tank to generate waves. In order to decouple the vibrations emerging from the fan it is mounted on a separate ISEL rack. At a water level of 3.5 cm in the shallow parts of the channel the motor frequency should not exceed 30 Hz to avoid water spilling into the air tubes. However, should this happen a 1 kW radiative heater is fitted into the air system allowing for a fast drying process.

The air circulation tubes and the radial fan composing the air system have a diameter of 25 cm. The whole system is linked to the glass channel by custom made transition elements manufactured by BECK-KUNSTSTOFFVERFORMUNG GMBH. These elements reduce the cross section to enhance the wind-speed and are additionally fitted with two rectifier elements: A long, honey comb shaped PP element (5 cm long, 8 mm honey combs) that attenuates turbulent eddies and a perforated PP plate (3 mm holes, 66% solid) that reduces centripetal force effects.

A connection to the exhaust air system of the institute is used to reduce the pressure within the wind-wave tank system. When working with harmful substances this system minimizes the risk of exposure. A valve is fitted into the connection between the radial ventilator and the exhaust system to enable experimenting at ambient pressure and with significantly diminished leakage rate (see section A.4). Three SERTO fittings are connected to the air tubes to allow for the injection of gases.

Air-Side Instrumentation

- **Air Temperature**

The air temperature is continuously monitored using a GREISINGER GMH 3710 precision thermometer. The temperature sensor is a PT100 sensor with an enhanced precision. It has an accuracy class of 1/10 DIN B and a measurement precision of ± 0.03 °C at 0 °C. The 3 mm thick sensor is mounted at the down wind edge of the replaceable cover plate using a compression fitting. The thermometer is read out using a GREISINGER GRS 3105 interface adapter that transfers the temperature signal to a serial bus allowing the HEURISKO worksheet used during the measurements to monitor and display the temperature continuously.

- **Differential Pressure Gauge - Inlet and Tank**

The digital differential pressure gauge GREISINGER GMSD 25 MR measures the pressure difference between two volumes connected to the sensor by hoses. The measurement range is -20 to +25 mbar with a resolution of 0.01 mbar and a relative precision of ± 0.2 %. Two of these sensors are in read out by a GREISINGER GMH3156 pressure meter. One indicates the pressure difference between the air inlet fitting and the ambient pressure. The other sensor is attached to the static pressure hose of the pitot-tube (see section A.3.1) and measures the pressure between the measurement area and the ambient air. The pressure meter is read out using a GREISINGER GRS 3105 interface adapter that transfers the temperature signal to the serial bus allowing the HEURISKO worksheet used during the measurements to monitor and display the pressure continuously.

- **Ambient Pressure**

The ambient pressure is measured by a VAISALA PTB100A analog barometer that is located at the larger linear wind-wave facility in the laboratory. It is read out using a REDLAB MEILHAUS A-D converter with a pressure range of 800 - 1060 mbar and a precision of ± 0.3 mbar.

- **Differential Pressure Gauge SI-Diff-Cap**

A differential pressure transmitter DIFF-CAP produced by SPECIAL INSTRUMENTS is a high precision measurement device for small pressure differences in a range of 0 - 2 mbar. It is used to monitor both the dynamic and static pressure at the Pitot-tube that is employed for wind velocity measurements. It is read out by the same REDLAB MEILHAUS A-D converter as the ambient pressure barometer.

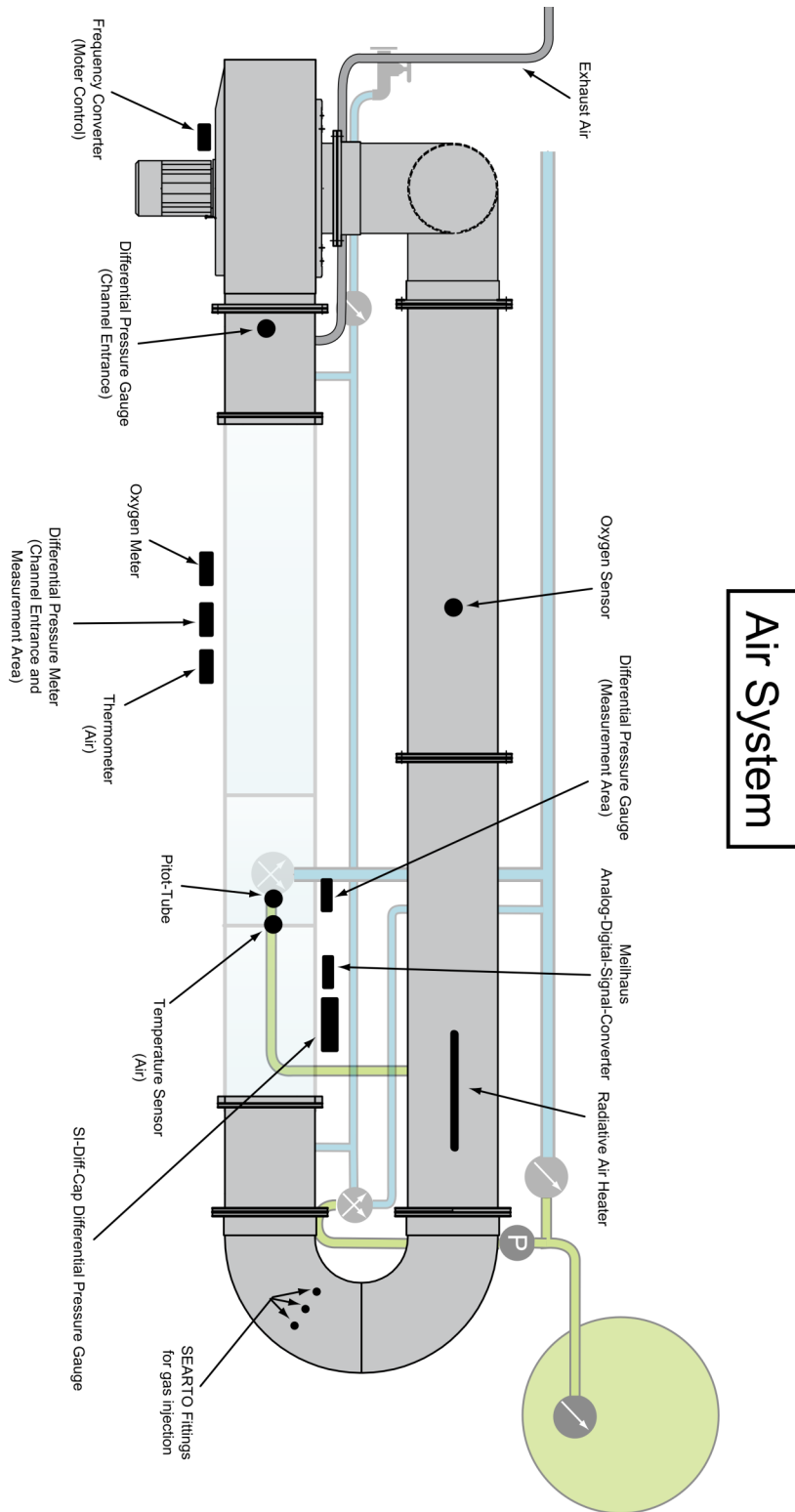


Figure A.7: Schematic setup of the air system

A.2.3 Stirred Tank

The stirred tank is a separable secondary device consisting of a tube system and a tank. Figure A.8 shows its general composition. It is used to pump the entire water of the wind-wave tank into an external reservoir where it can be prepared with chemicals for new measurements. The ARICON FD-A 75 cylindrical tank holds up to 75l of water and is made of chemical resistant polyethylene. A stirrer controlled by a SIEMENS SINAMICS G110 0.75 kW frequency generator is applied to mix the fluid in the tank.

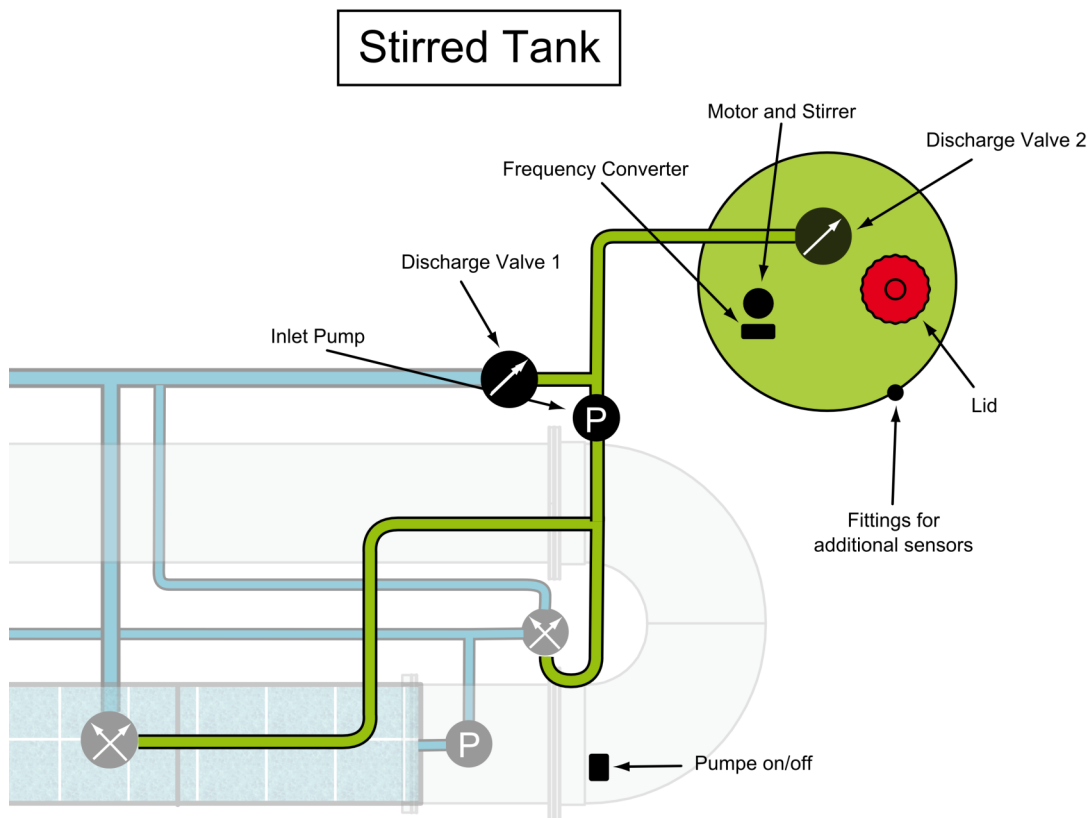


Figure A.8: Schematic setup of the stirred tank system

Filling and Depletion

Just below the tank a PP tubing system ensures a quick drainage of the tank content into the wastewater system of the laboratory. The valve can also be set to either pumping the entire water of the wind-wave tank into the stirred tank or press the water back into the wind-wave tank's water system by hydrostatic pressure.

A.3 Characterization

The following sections provide a characterization of the wind-wave tank in terms of the air-sided flow field and the leakage rate. Both measurements have been redone in comparison to the previously published data in [74].

A.3.1 Wind Profile

To obtain the wind profile of the wind-wave tank a custom cover plate was constructed that allows for the positioning of a Pitot-tube at five different positions perpendicular to the wind direction within the measurement area. A sketch of the setup is shown in figure A.9.

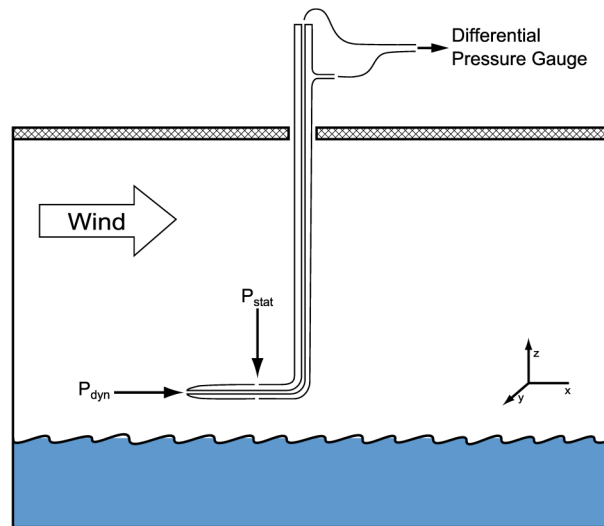


Figure A.9: Setup for wind-profile measurements

Functionality of the Pitot-tube

The Pitot-tube consists of two tubes, one set inside the other. The inner tube is oriented in wind direction, the outer tube has several openings on the side where only static pressure applies. The elliptic outer shape of the tube allows the direction of inflow to vary by about $\pm 15^\circ$ without substantial measurement inaccuracies. A differential pressure gauge compares the pressure of the inner and outer tube (p_{diff}). This pressure difference can be used to calculate the actual wind speed v :

$$v = \sqrt{\frac{2}{\rho_{\text{air}}}} \cdot p_{\text{diff}} \quad (\text{A.1})$$

Where ρ_{air} is the density of air. The latter one is calculated by

$$\rho_{\text{air}} = 1,2931 \cdot \frac{p_{\text{atm}} + p_{\text{stat}}}{p_0} \cdot \frac{T_0}{T_0 + T} \quad (\text{A.2})$$

Here p_{atm} is the ambient pressure, p_{stat} is the static pressure at the measurement area, T is the temperature, $p_0 = 1013 \text{ mbar}$ is the normal pressure and $T_0 = 293 \text{ K}$ the normal temperature.

A.3.2 Experimental Method and Measurements

The height of the Pitot-tube is set by a stepping motor operated by a NANOTEC-CONTROLLER (MODEL: SMCI 32-1). Both the stepping motor controller and the SINAMICS G110 0.75 kW frequency generator that sets the current wind speed are driven by a REDLAB MEILHAUS A-D converter. This setup ensures an automated control of both measurement height and wind speed using a HEURISKO worksheet.

The cover plate permits five different positions for the Pitot-tube. At each of these positions the wind velocity profile is scanned from a height just above the wave crest up to 90 mm above the calm water surface in 1 mm steps for a set of motor frequencies. The worksheet records the air temperature T_{air} , the ambient pressure p_a , the differential pressure between the tank and the laboratory p_b and the differential pressure at the Pitot-tube p_{diff} :

$$p_{\text{atm}} = p_a \quad p_{\text{stat}} = p_a + p_b \quad (\text{A.3})$$

The differential pressure gauge SI DIFF CAP at the Pitot-tube can measure pressure differences of at most 2 mbar. At a motor frequency of 30 Hz this is reached. No measurements for higher frequencies can be conducted.

A.3.3 Wind Profile and Characteristics

The Wind Profile

The wind-wave tank presented here is a linear system, the air flow is in good approximation one-dimensional. Therefore the velocity profile should be linear very close to the surface and logarithmic further up. Near the top of the channel the effects of the ceiling should lead to another logarithmic shape. See chapter 2 for details on the expected shape of the profile.

Results

Figure A.10 shows a 3-dimensional plot of the wind profile for a motor frequency of 13.7 Hz. There is a slight asymmetry between the wind velocities at the edge of the

profile. In addition, the lowest velocities near the surface are actually located in the middle of the channel. If the air flow was perfectly homogeneous one would expect a symmetrical shape that increases towards the middle position. Compared to earlier measurements [74] the installation of an additional flow rectifier improved the overall shape of the profile.

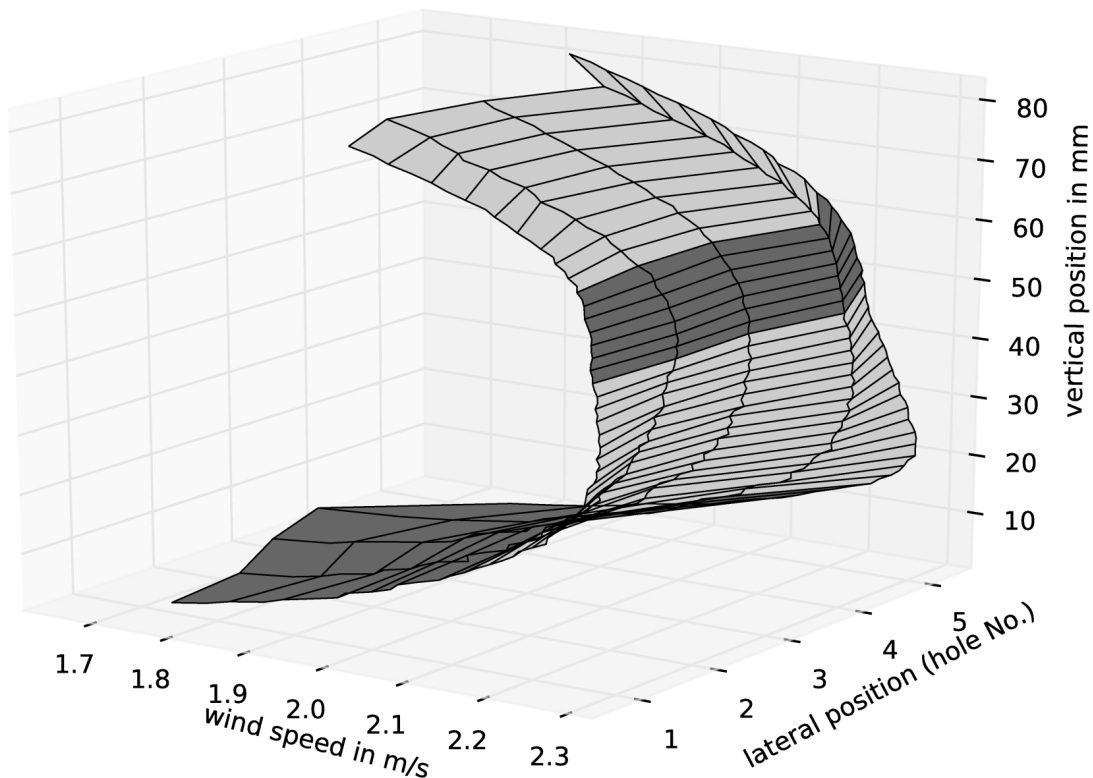


Figure A.10: 3-D plot of the wind profile at 13.7 Hz motor frequency.

For a comparison of theoretical models and experimental data of the gas transfer, knowledge about the friction velocity u_* and the surface roughness z_0 is crucial. While it is advised to determine these parameters during each gas transfer measurement they are presented here as a point of reference for the planning of future experiments. Figure A.11 shows the wind velocity profiles for several motor frequencies.

All profiles displayed the expected logarithmic shape. Near the cover plate at the top of the profile the velocity decreases. The Pitot-tube cannot measure the profile up to the ceiling of the channel which would be at 100 mm above the water surface. Due to the reduction of the wind speed near the ceiling a logarithmic fit was only used in a limited section of the profiles to determine the friction velocity u_* and the roughness z_0 . Figure A.12 shows one such profile and fit.

In a similar manner u_* was obtained for a range of motor frequencies. Figure A.13

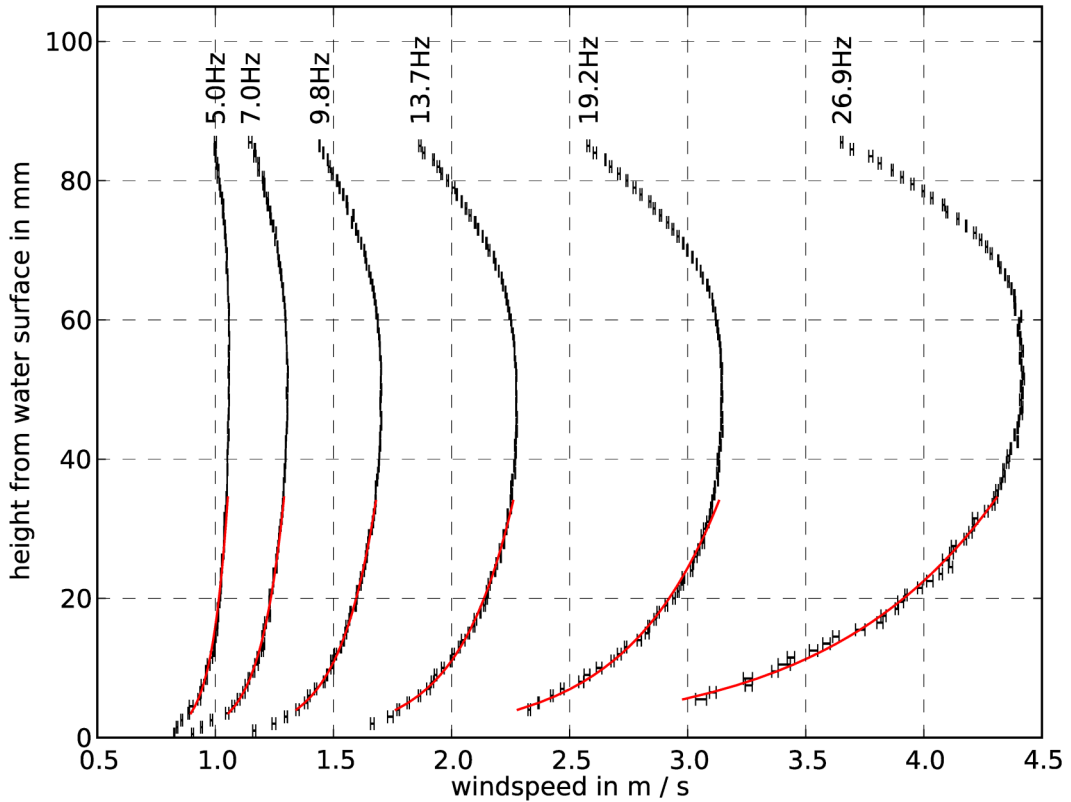


Figure A.11: Wind profiles at various motor frequencies (Pitot-tube in the middle of the tank)

illustrates the correlation.

Up to a motor frequency of 15 Hz the friction velocity u_* and motor frequency are linearly correlated. At higher motor frequencies and thus wind speeds the data scatters strongly and no obvious correlation was found.

The second fit parameter is the roughness z_0 . Its correlation to the motor frequency is pictured in figure A.14. The surface tends to be very smooth up to a motor frequency of 15 Hz, which is the same frequency where the above mentioned correlation of u_* and the motor frequency broke down. At higher frequencies, where wave generation commences, z_0 shows a cubic relation to the motor frequency.

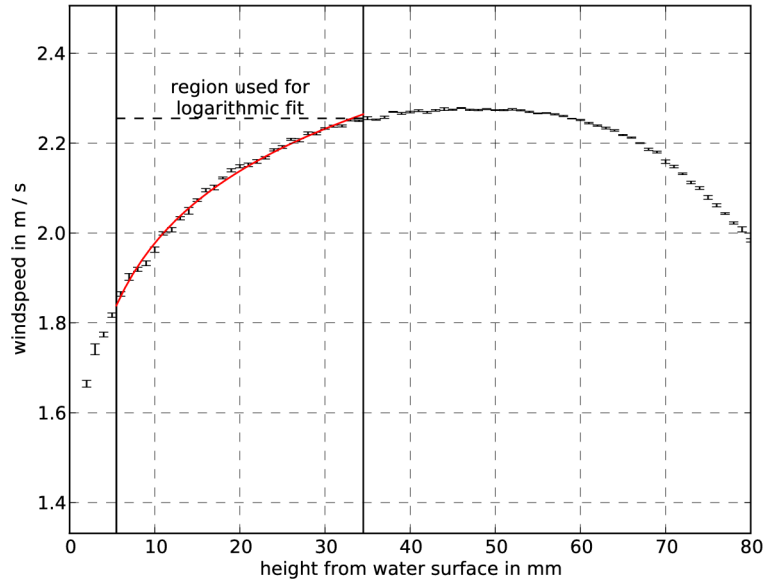


Figure A.12: Velocity profile at a motor frequency of 13.7 Hz

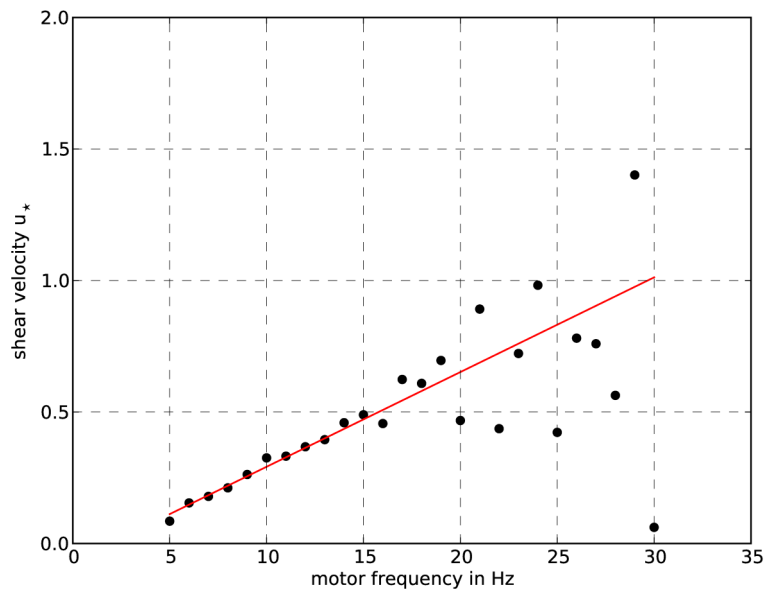


Figure A.13: Friction velocity u_* as a function of the motor frequency

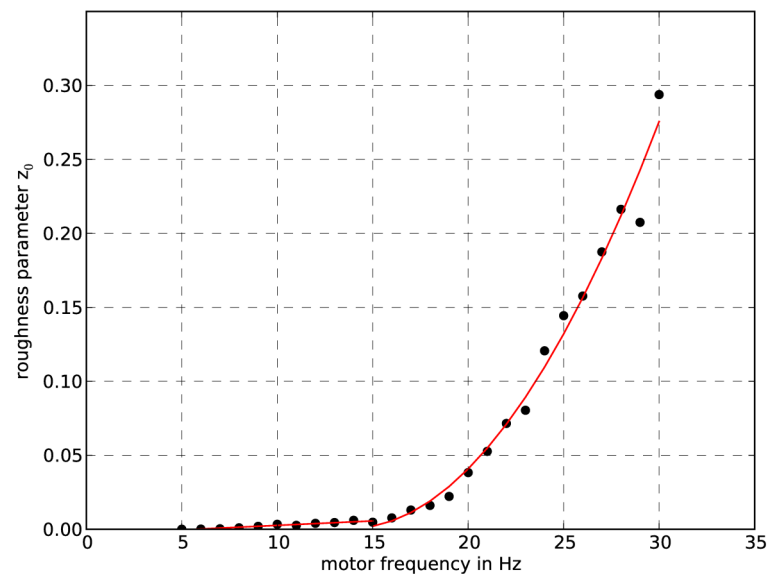


Figure A.14: Roughness z_0 plotted against the motor frequency

A.4 Leakage Rate

The leakage rate is an important characteristic for every wind-wave tank that is used for transfer experiments. In the case of invasion and evasion experiments it has to be taken into consideration when observing measured air-bulk concentration data because the leakage changes the concentration.

If the experiments require a different gaseous environment than air, for example a pure nitrogen environment to reduce quenching effects, the leakage rate has to be compensated for as laboratory air flows back into the wind-wave tank. The leakage rate is also an important factor when considering the health risks of an experiment when using dangerous substances.

The rate given below can be used as a reference after extensive alterations of the wind-wave tank have been conducted to check if the system has been reassembled correctly.

A.4.1 Experimental Method

The leakage rate was determined by giving a small amount of methane (CH_4) into the tank and measuring its reduction. The measurement was performed using an IR-spectrometer¹ that is employed for measurements at the Aeolotron wind-wave facility. Two measurements were conducted: One with attached exhaust air and one without.

Calculation To compute the leakage rate a simple box model was used. An amount of methane c_{CH_4} is introduced into the tank. Its reduction \dot{c}_{CH_4} is proportional to the leakage rate k_L , as there are no other ways for the substance to disappear than by leakage into the surrounding laboratory. The differential equation that results from this model reads:

$$\dot{c}_{\text{CH}_4} = -k_L c_{\text{CH}_4} \quad (\text{A.4})$$

This equation can easily be integrated:

$$c_{\text{CH}_4}(t) = A + c_{\text{CH}_4} e^{-k t} \quad (\text{A.5})$$

By fitting this equation to the data, the leakage rate is determined.

¹Advance Optima URAS 14 by Hartmann & Braun

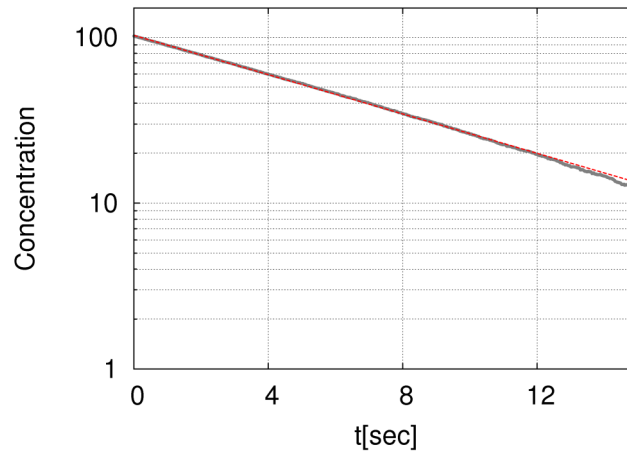


Figure A.15: Logarithmic plot of the CH₄ concentration with exhaust air.

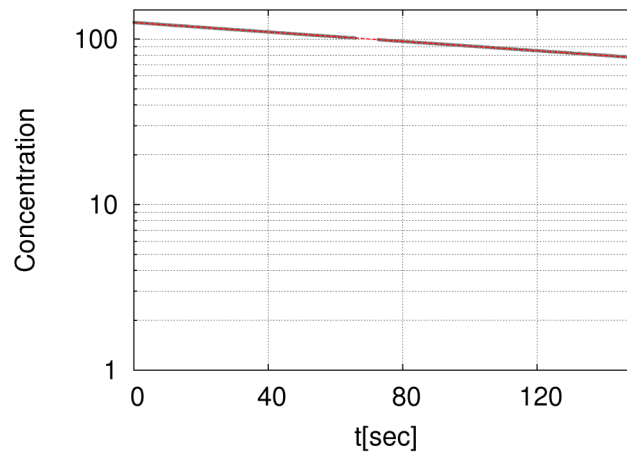


Figure A.16: Logarithmic plot of the CH₄ concentration without exhaust air.

A.4.2 Results

Fitting equation (A.5) to the acquired data (see figure A.15 and A.16) lead to a leakage rate of 34 l/min with attached exhaust air. When the exhaust air is detached from the wind-wave tank, the resulting leakage rate is 0.8 l/min.

B Datasheets

B.1 UV Broadband Anti-Reflective Coating ARB 2 UV

The fused silica lenses used for most setups within this work had a broadband anti-reflective coating provided by Linos/Qioptiq to reduce losses due to reflection. The effectiveness of this coating as provided by Linos/Qioptiq is shown in figure B.1. It has a guaranteed residual reflectance of less than 5% on fused silica for wavelengths between 250nm and 400nm.

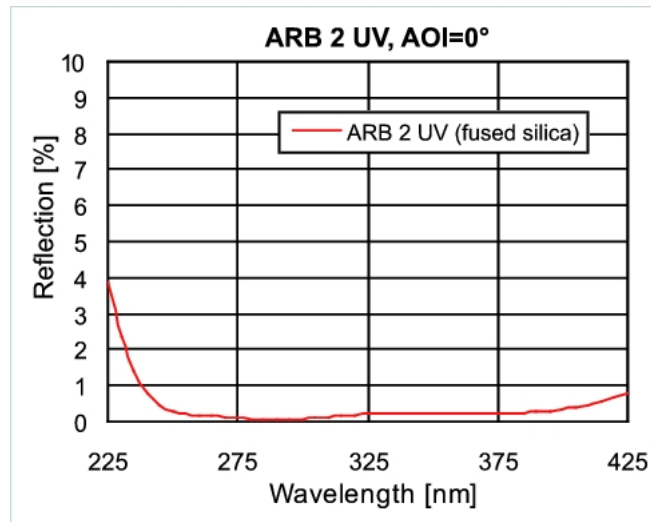


Figure B.1: Effectiveness of the ARB2 coating. (Source: Linos/Qioptiq)

B.2 Sensicam EM UV Calibration Data

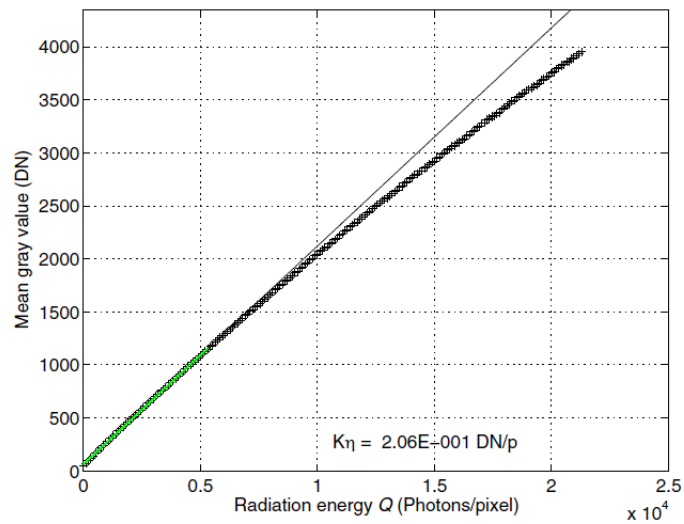


Figure B.2: Sensitivity of the Sensicam UV at gain 5. (Source: AEON Verlag)

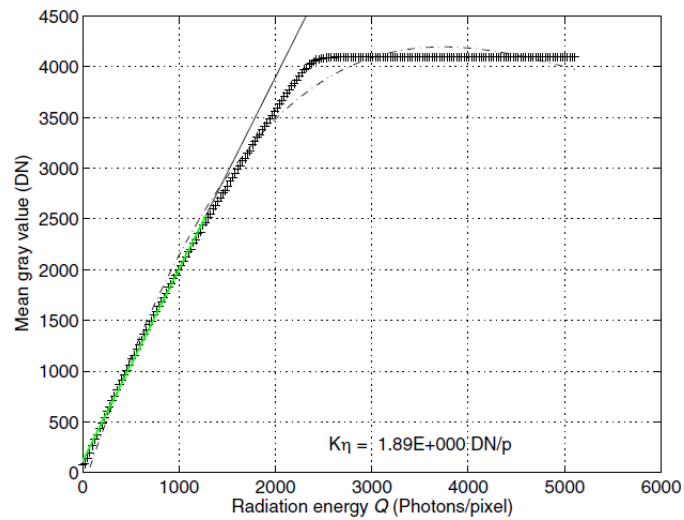


Figure B.3: Sensitivity of the Sensicam UV at gain 50. (Source: AEON Verlag)

B.3 Absorption and Fluorescence Spectra

B.3.1 Acetone

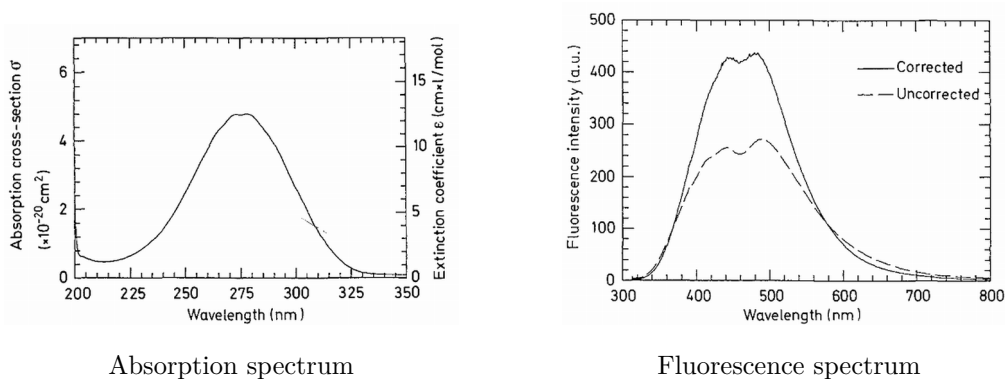


Figure B.4: Gas phase absorption and fluorescence spectra of acetone.
Source: Lozano et al. [44]

B.3.2 Ethanal

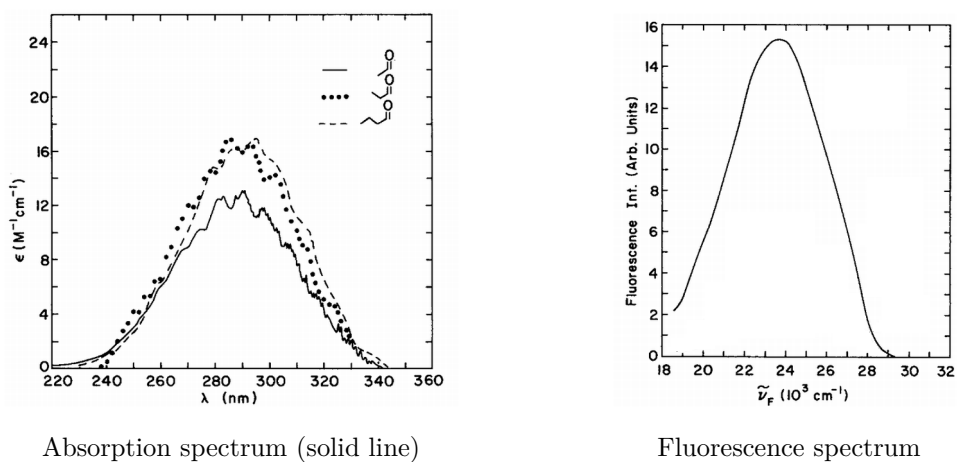


Figure B.5: Gas phase absorption and fluorescence spectra of ethanal.
Source: Hansen and Lee [25]

B.3.3 Diacetyl

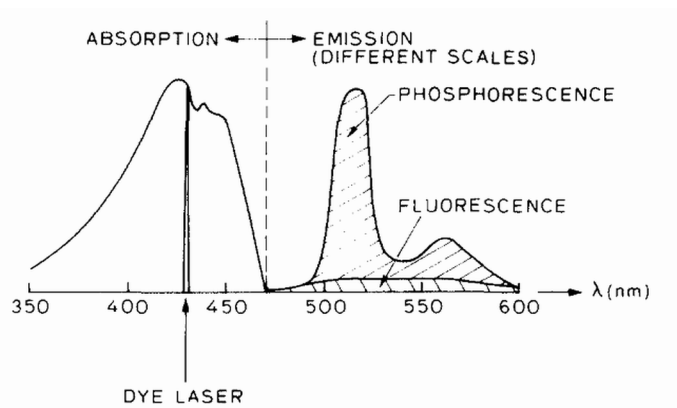


Figure B.6: Gas phase absorption and fluorescence spectra of diacetyl.
Source: Hiller et al. [31]

C Bibliography

- [1] M. Ageno, M. Chiozzotto, and R. Querzoli. Scintillations in liquids and solutions. *Phys. Rev.*, 79(4):720, Aug 1950.
- [2] R. S. Alexandra Pincock, James Pincock. Substituent effects on the rate constants for the photo-claisen rearrangement of allyl aryl ethers. *J. Am. Chem. Soc.*, 124 (33):9768–9778, 2002.
- [3] D. Ambrose, C. H. S. Sprake, and R. Townsend. Thermodynamic properties of organic oxygen compounds xxxiii. the vapour pressure of acetone. *The Journal of Chemical Thermodynamics*, 6(7):693 – 700, 1974. ISSN 0021-9614.
- [4] D. Ambrose, J. H. Ellender, C. H. S. Sprake, and R. Townsend. Thermodynamic properties of organic oxygen compounds xliii. vapour pressures of some ethers. *The Journal of Chemical Thermodynamics*, 8(2):165 – 178, 1976. ISSN 0021-9614.
- [5] A. Arnold, H. Becker, R. Suintz, P. Monkhouse, J. Wolfrum, R. Maly, and W. Pfister. Flame front imaging in an internal-combustion engine simulator by laser-induced fluorescence of acetaldehyde. *Opt. Lett.*, 15(15):831–833, Aug 1990.
- [6] H. J. Benkelberg, S. Hamm, and P. Warneck. Henry’s law coefficients for aqueous solutions of acetone, acetaldehyde and acetonitrile, and equilibrium constants for the addition compounds of acetone and acetaldehyde with bisulfite. *Journal of Atmospheric Chemistry*, 20:17–34, 1995. ISSN 0167-7764.
- [7] I. B. Berlman. *Handbook of fluorescence spectra of aromatic molecules*. Academic Press, 1971.
- [8] E. Breuer, G.M.; Lee. Fluorescence and phosphorescence of hexafluoroacetone vapor. *J. Phys. Chem.*, 68:2982 – 2985, 1964.
- [9] S. Bull. Isothermic equilibrium of liquid-steam in system water-acetoaldehyde. *Khim. Prom. (Moscow)*, 7:507–509, 1963. Data available via NIST.
- [10] M. Coantic. A model of gas transfer across air–water interfaces with capillary waves. *Journal of Geophysical Research*, 91:3925–3943, 1986.
- [11] L. S. Coyne. An evaluation of a new film for air sampling bags used in industrial hygiene and ambient air sampling. SKC Inc.
- [12] J. P. Crimaldi. Planar laser induced fluorescence in aqueous flows. *Exp. Fluids*, pages 44:851–863, 2008.
- [13] F. Damon, G.H.; Daniels. The photolysis of gaseous acetone and the influence of water. *J. Am. Chem. Soc.*, 55:2363 – 2375, 1933.

- [14] E. L. Deacon. Gas transfer to and across an air-water interface. *Tellus*, 29:363–374, 1977.
- [15] F. Dearden. Light absorption studies part xvi. the ultraviolet absorption spectra of phenols. *Can. J. Chem.*, 37, 1959.
- [16] K. Degreif. *Untersuchungen zum Gasaustausch - Entwicklung und Applikation eines zeitlich aufgelösten Massenbilanzverfahrens*. Dissertation, Institut für Umweltphysik, Fakultät für Physik und Astronomie, Univ. Heidelberg, 2006.
- [17] M. A. Donelan, W. M. Drennan, E. S. Saltzman, and R. Wanninkhof, editors. *Gas Transfer at Water Surfaces*, 2002. American Geophysical Union.
- [18] I. Düwel, W. Koban, F. Zimmermann, T. Dreier, and C. Schulz. Spectroscopic characterization of the fluorobenzene/dema tracer system for laser-induced exciplex fluorescence for the quantitative study of evaporating fuel sprays. *Applied Physics B: Lasers and Optics*, 97:909–918, 2009. ISSN 0946-2171.
- [19] M. Erz. *Charakterisierung von Laufzeitkamarasystemen für Lumineszenzlebensdauermessungen*. Dissertation, IWR, Fakultät für Physik und Astronomie, Univ. Heidelberg, 2011.
- [20] A. Falkenroth. *Visualisation of Oxygen Concentration Profiles in the Aqueous Boundary Layer*. Dissertation, Fakultät für Chemie und Geowissenschaften, Univ. Heidelberg, 2007.
- [21] A. Falkenroth, A. Herzog, and B. Jähne. Visualization of air-water gas exchange using novel fluorescent dyes. In *12th Intern. Symp. on Flow Visualization, Göttingen, 10–14. September 2006*, 2006.
- [22] F. Friedl. Dissertation, IWR, Fakultät für Physik und Astronomie, Univ. Heidelberg, 2012.
- [23] J. Gliß. *Entwicklung und Implementierung eines Cavity-Enhanced-Spektrometers am Wind-Wellen-Kanal*. Bachelor’s thesis, Institut für Umweltphysik, Fakultät für Physik und Astronomie, Univ. Heidelberg, 2010.
- [24] G. M. Hale and M. R. Query. Optical constants of water in the 200 nm to 200 μm wavelength region. *Appl. Opt.*, 12:555–563, 1973.
- [25] D. A. Hansen and E. K. C. Lee. Radiative and nonradiative transitions in the first excited singlet state of simple linear aldehydes. *The Journal of Chemical Physics*, 63(8):3272–3277, 1975.
- [26] R. K. Hanson, J. M. Seitzman, and P. H. Paul. Planar laser-fluorescence imaging of combustion gases. *Applied Physics B: Lasers and Optics*, 50:441–454, 1990. ISSN 0946-2171.
- [27] C. Hassa, P. H. Paul, and R. K. Hanson. Laser-induced fluorescence modulation techniques for velocity measurements in gas flows. *Experiments in Fluids*, 5:240–246, 1987.
- [28] A. Herzog. *Imaging of Water-sided Gas-Concentration Fields at a Wind-Driven, Wavy Air-Water Interface*. Dissertation, Institut für Umweltphysik, Fakultät für Physik und Astronomie, Univ. Heidelberg, 2010.
- [29] A. G. Herzog, F. Friedl, and B. Jähne. Spatio-temporal fluctuations of water-sided gas concentration fields under wind-induced turbulence. In *6th Int. Symp. Gas Transfer at Water Surfaces, Kyoto, May 17–21, 2010*, 2010.

-
- [30] B. Hiller and R. K. Hanson. Properties of the iodine molecule relevant to laser-induced fluorescence experiments in gas flows. *Experiments in Fluids*, 10:1–11, 1990.
- [31] B. Hiller, R. A. Booman, C. Hassa, and R. K. Hanson. Velocity visualization in gas flows using laser-induced phosphorescence of biacetyl. *Review of Scientific Instruments*, 55(12):1964–1967, 1984.
- [32] E. Hoffmann. Vapor pressure data of simple organic substances: their availability and reliability. *Journal of Chemical Information and Computer Sciences*, 24(1):3–6, 1984.
- [33] C. A. Hughey, R. P. Rodgers, and A. G. Marshall. Resolution of 11000 compositionally distinct components in a single electrospray ionization fourier transform ion cyclotron resonance mass spectrum of crude oil. *Analytical Chemistry*, 74(16):4145–4149, 2002.
- [34] A. W. Jackson and A. J. Yarwood. Fluorescence and phosphorescence of 2,3-pentanedione. *Canadian Journal of Chemistry*, 50:Pages 1325–1330, 1972.
- [35] B. Jähne. Dry deposition of gases over water surfaces (gas exchange). In D. Flothmann, editor, *Exchange of Air Pollutants at the Air-Earth Interface (Dry Deposition)*. Battelle Institute, Frankfurt, 1982.
- [36] B. Jähne. *Digital Image Processing*. Springer, Berlin, 6th edition, 2005.
- [37] B. Jähne. Air-sea gas exchange. In J. H. Steele, K. K. Turekian, and S. A. Thorpe, editors, *Encyclopedia Ocean Sciences*, pages 3434–3444. Elsevier, 2009.
- [38] L. Jian-Bang, P. Qi, L. Chang-Sheng, and S. Jie-Rong. Principles of flow field diagnostics by laser induced biacetyl phosphorescence. *Experiments in Fluids*, 6:505–513, 1988.
- [39] J. L. Kinsey. Laser-induced fluorescence. *Annual Review of Physical Chemistry*, 28(1):349–372, 1977.
- [40] C. Kräuter, K. E. Richter, B. Jähne, E. Mesarchaki, and J. Williams. Austausch flüchtiger Stoffe an der Wasser-Luft-Grenzschicht bei kombinierter luft/wasserseitiger Kontrolle. In *Verhandlungen der Deutschen Physikalischen Gesellschaft, Spring Conference, Dresden, 13.-18.03.2011*, 2011.
- [41] J. R. Lakowicz. *Principles of Fluorescence Spectroscopy*. Springer, 3. edition, 2006.
- [42] D. A. Lerner, P. M. Horowitz, and E. M. Evieth. Comparative photophysics of indolizine and related heterocyclics. *J. Phys. Chem.*, 81(1):12–17, 1977.
- [43] P. Linstrom and W. Mallard. *NIST Chemistry WebBook, NIST Standard Reference Database Number 69*. National Institute of Standards and Technology, 2011.
- [44] A. Lozano, B. Yip, and R. K. Hanson. Acetone: a tracer for concentration measurements in gaseous flows by planar laser-induced fluorescence. *Experiments in Fluids*, 13:369–376, 1992.
- [45] D. Mackay and W. Y. Shiu. A critical review of Henry’s law constants for chemicals of environmental interest. *Journal of Physical and Chemical Reference Data*, 10:1175–1199, 1981.
- [46] T. Münsterer and B. Jähne. LIF measurements of concentration profiles in the aqueous mass boundary layer. *Exp Fluids*, 25:190–196, 1998.

- [47] W. C. Neely and T. D. Hall. Vapor pressure of biacetyl. *Journal of Chemical & Engineering Data*, 17(3):294–295, 1972.
- [48] New York Times. Gulf spill is the largest of its kind, scientists say, 2010. August 2, www.nytimes.com.
- [49] S. M. Nikiforov, S. S. Alimpiev, M. W. George, B. G. Sartakov, and Y. O. Simanovsky. Anomalous reflection of water surface during laser ablation. *Optics Communications*, 182: 17–24, Aug. 2000.
- [50] J. Nikuradse. Strömungsgesetze in rauhen Röhren. *V.D.I.Forschungsheft*, 361:1, 1933.
- [51] NPIC. DDT technical fact sheet, 1999.
- [52] Occupational Safety and Health Administration. Chemical sampling information 2,3-pentanedione.
- [53] A. G. Osborn and D. W. Scott. Vapor pressures of 17 miscellaneous organic compounds. *The Journal of Chemical Thermodynamics*, 12(5):429 – 438, 1980. ISSN 0021-9614.
- [54] W. Pinney. The relation between the bactericidal activities and certain physico-chemical properties of some fluorophenols. *J Pharm Pharmacol.*, Jul;21(7):415–22, 1969.
- [55] H. Reichardt. Vollständige Darstellung der turbulenten Geschwindigkeitsverteilung in glatten Leitungen. *Zeitschrift für angewandte Mathematik und Mechanik*, 31:208–219, 1951.
- [56] G. T. Reynolds, F. B. Harrison, and G. Salvini. Liquid scintillation counters. *Phys. Rev.*, 78(4):488, May 1950.
- [57] R. Rocholz. *Spatiotemporal Measurement of Short Wind-Driven Water Waves*. Dissertation, Institut für Umweltp Physik, Fakultät für Physik und Astronomie, Univ. Heidelberg, 2008.
- [58] W. Roedel. *Physik unserer Umwelt: die Atmosphäre*. Springer-Verlag, 3 edition, 2000.
- [59] U. Schimpf, C. Garbe, and B. Jähne. Investigation of transport processes across the sea surface microlayer by infrared imagery. *Journal of Geophysical Research-Oceans*, 109(C8): C08S13, 2004. ISSN 0148-0227.
- [60] R. P. Schwarzenbach, P. M. Gschwend, and I. D.M. *Environmental Organic Chemistry*. Wiley-Interscience, 2 edition, 2003.
- [61] D. W. Scott, J. P. McCullough, W. D. Good, J. F. Messerly, R. E. Pennington, T. C. Kincheloe, I. A. Hossenlopp, D. R. Douslin, and G. Waddington. Fluorobenzene: Thermodynamic properties in the solid, liquid and vapor states; a revised vibrational assignment. *Journal of the American Chemical Society*, 78(21):5457–5463, 1956.
- [62] V. Sick. Exhaust-gas imaging via planar laser-induced fluorescence of sulfur dioxide. *Applied Physics B: Lasers and Optics*, 74:461–463, 2002. ISSN 0946-2171.
- [63] J. Staudinger and P. V. Roberts. A critical compilation of Henry’s law constant temperature dependence relations for organic compounds in dilute aqueous solutions. *Chemosphere*, 44 (4):561 – 576, 2001. ISSN 0045-6535.

-
- [64] T. I. Storer. DDT and wildlife. *The Journal of Wildlife Management*, Vol. 10:pp. 181–183, 1946.
- [65] T. Takahashi, S. C. Sutherland, C. Sweeny, A. Poisson, N. Metzl, B. Tilbrook, N. Bates, R. Wanninkhof, R. A. Feely, C. Sabine, J. Olafsson, and Y. Nojiri. Global sea-air CO₂ flux based on climatological surface ocean pCO₂ and seasonal biological and temperature effects. *Deep-Sea Research II*, 49:1601–1622, 2002.
- [66] I. van Cruyningen, A. Lozano, and R. K. Hanson. Quantitative imaging of concentration by planar laser-induced fluorescence. *Experiments in Fluids*, 10:41–49, 1990.
- [67] A. Vogel and V. Venugopalan. Mechanisms of pulsed laser ablation of biological tissues. *Chemical Reviews*, 103(2):577–644, 2003.
- [68] F. Vogel. Spectroscopic techniques for gas-exchange measurements. Diplomarbeit, Institut für Umweltphysik, Fakultät für Physik und Astronomie, Univ. Heidelberg, 2006.
- [69] L. J. Volk and E. K. C. Lee. Reinvestigation of vibronic level dependence of fluorescence quantum yields and radiative and nonradiative lifetimes of p-difluorobenzene in its first excited singlet state. *The Journal of Chemical Physics*, 67(1):236–241, 1977.
- [70] K. H. W. Gottwald. *UV/VIS-Spektroskopie für Anwender*. Wiley-VCH, 1998.
- [71] D. A. Walker. A fluorescence technique for measurement of concentration in mixing liquids. *Journal of Physics E: Scientific Instruments*, 20(2):217, 1987.
- [72] R. Wanninkhof. Relationship between wind speed and gas exchange over the ocean. *J. Geophys. Res.*, 97:7373–7382, 1992.
- [73] R. Wanninkhof and W. R. McGillis. A cubic relationship between gas transfer and wind speed. *Geophys. Res. Lett.*, 26:1889–1892, 1999.
- [74] P. Warken. Hochauflösende LIF-Methode zur Messung von Sauerstoffkonzentrationsprofilen in der wasserseitigen Grenzschicht. Diplomarbeit, Institut für Umweltphysik, Fakultät für Physik und Astronomie, Univ. Heidelberg, 2010.
- [75] L. M. Wolff and T. J. Hanratty. Instantaneous concentration profiles of oxygen accompanying absorption in a stratified flow. *Experiments in Fluids*, 16(6):385–392, 1994.
- [76] World Health Organisation. WHO gives indoor use of DDT a clean bill of health for controlling malaria, 2006.
- [77] S. H. Yalkowsky, R. J. Orr, and S. C. Valvani. Solubility and partitioning. 3. the solubility of halobenzenes in water. *Industrial and Engineering Chemistry Fundamentals*, 18(4): 351–353, 1979.
- [78] C. L. Yaws. *Handbook of Transport Property Data*. Gulf Publishing Company, 1995.